

N° ...

UNIVERSITÉ DES SCIENCES ET TECHNOLOGIES DE LILLE 1

Ecole Doctorale

Science Pour l'Ingénieur Université Lille Nord-de-France

THÈSE

Présentée et soutenue en vue de l'obtention du grade de

Docteur

**Spécialité Génie Civil en Hydrodynamique et Mécanique des Fluides
Numérique**

Par Dwinanti Rika MARTHANTY

**Développement de la méthode SPH (smoothed particle
hydrodynamics) pour simuler les caractéristiques de base de la
dynamique des méandres**

Soutenue le 26 avril 2016 devant la Commission d'Examen composée de :

Pr. Isam SHAHROUR	Laboratoire Génie Civil et géo- Environnement, Université Lille 1, France	Directeur de laboratoire
Prof. Dedi Priadi	Faculty of Engineering, Universitas Indonesia, Indonesia	Dean
Pr. Erick CARLIER	École Polytech Lille, Université Lille 1, France	Directeur de thèse
Dr-Ing. Dwita Sutjiningsih	Departemen Teknik Sipil, Universitas Indonesia, Indonesia	Promotor
Herr Soeryantono, PhD	Departemen Teknik Sipil, Universitas Indonesia, Indonesia	Co-promotor
Pr. Hassan SMAOUI	Laboratoire Roberval, Université Technologie de Compiègne, France	Rapporteur
Prof. Iwan Kridasantausa Hadihardaja	Departemen Teknik Sipil, Institut Teknologi Bandung, Indonesia	Reader



**UNIVERSITAS
INDONESIA**



**DEVELOPING SMOOTHED PARTICLE HYDRODYNAMICS
METHOD TO MODEL BASIC CHARACTERISTICS OF
MEANDERING DYNAMICS**

DISSERTATION

a dissertation submitted to the Doctoral Program in Civil Engineering in
conformity with the requirements for the Degree of Doctor
in the fields of Hydrodynamics and Computational Fluid Dynamics

Dwinanti Rika Marthanty

NPM.1006751640

INE.0CPZRL05TL5

Double Degree Program Indonesia - France

Departemen Teknik Sipil, Universitas Indonesia, Indonesia

Laboratoire Génie Civil et géo-Environnement, Université Lille 1, France

June 2016

STATEMENT OF ORIGINALITY AND AUTHENTICITY

I hereby declare that this dissertation is my own work,
and for all references cited, I have stated all correctly.

Name: Dwinanti Rika Marthanty

NPM: 1006751640



Signature:

Date: 15 JUNI 2016

DISSERTATION ACCEPTANCE

This is to certify that the dissertation prepared

By: Dwinanti Rika Marthanty

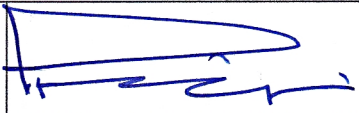

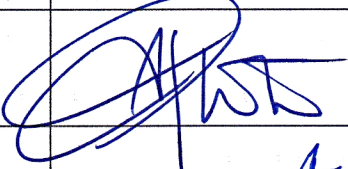

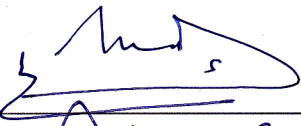
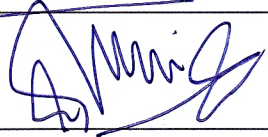
NPM: 1006751640

Study Program: Civil Engineering, Faculty of Engineering, Universitas Indonesia

entitled: DEVELOPING SMOOTHED PARTICLE HYDRODYNAMICS METHOD TO MODEL BASIC CHARACTERISTICS OF MEANDERING DYNAMICS

For the degree of: Doctor

Is approved by the final examining committee:

Dean	: Prof. Dedi Priadi	
Promotor	: Dr-Ing. Dwita Sutjiningsih	
Co-promotor	: Herr Soeryantono, PhD	
Reader	: Prof. Iwan K. Hadihardaja	
Jury	: Dr. Ahmad Indra Siswantara	
Jury	: Alhadi Bustamam, PhD	

Certified at: Depok, Jawa Barat, Indonesia

Date: 15 JUNI 2016

**HALAMAN PERNYATAAN PERSETUJUAN PUBLIKASI
TUGAS AKHIR UNTUK KEPENTINGAN AKADEMIS**

Sebagai sivitas akademik Universitas Indonesia, saya yang bertanda tangan di bawah ini:

Nama : Dwinanti Rika Marthanty
NPM : 1006751640
Program Studi : Teknik Sipil
Departemen : Teknik Sipil
Fakultas : Teknik
Jenis karya : Disertasi

demi pengembangan ilmu pengetahuan, menyetujui untuk memberikan kepada Universitas Indonesia Hak Bebas Royalti Noneksklusif (Non-exclusive Royalty Free Right) atas karya ilmiah saya yang berjudul :

DEVELOPING SMOOTHED PARTICLE HYDRODYNAMICS METHOD TO
MODEL BASIC CHARACTERISTICS OF MEANDERING DYNAMICS

beserta perangkat yang ada (jika diperlukan). Dengan Hak Bebas Royalti Noneksklusif ini Universitas Indonesia berhak menyimpan, mengalihmedia/formatkan, mengelola dalam bentuk pangkalan data (database), merawat, dan memublikasikan tugas akhir saya selama tetap mencantumkan nama saya sebagai penulis/pencipta dan sebagai pemilik Hak Cipta.

Demikian pernyataan ini saya buat dengan sebenarnya.

Dibuat di : Depok, Jawa Barat, Indonesia

Pada tanggal : 15 JUNI 2016

Yang menyatakan



(Dwinanti Rika Marthanty)

ABSTRACT

Name: Dwinanti Rika Marthanty

Study Program: Civil Engineering

Title: Developing Smoothed Particle Hydrodynamics Method to Model Basic Characteristics of Meandering Dynamics

Meanders occur even without sediment transport, it is caused by a large-scale turbulence (da Silva, 2006). Meandering channels research in general is separated, but still correlated, into two approaches: geomorphologic and fluid dynamics, where 3D flow modeling receives more attention for its ability to simulate helicoidal motion even though it is high in computational efforts and limited to simple geometry (Camporeal, et al., 2007). One developed model with a finite element method for three-dimensional flow is called Resource Modelling Associates (RMA), to model; density stratified flow (RMA-10), and water quality in estuaries and streams (RMA-11) (King, 2013). Smoothed particle hydrodynamics (SPH) is one most noticeable meshfree method and now become very popular, particularly for free surface flows, it is a robust and powerful method for describing deforming media (Gomez-Gesteira, et al., 2010). SPH is a very promising method to answer 3D flow modeling in meander dynamics. Objective of this research that helical flow patterns from flow simulation with 3D nearly incompressible flow SPH method is comparable to flow simulation with 3D stratified flow finite element method. Approaches in this research is divided into two big parts; (1) modeling meander dynamics with RMA to determine its basic characteristics, and (2) development smoothed particle hydrodynamics (SPH) method to simulate helical flow in a curved channel. The finite element model using in this study, RMA has shown its capability to simulate the meander key characteristics and are agreed with experiments of Hasegawa (1983), and Xu and Bai (2013). These results are used as a reference in developing a method to model meander dynamics. SPH procedures are developed from 3D fluid flow model, collision handling between water particles, and curved channel boundary conditions. The very basic characteristic in meander dynamics is helical flow. With SPH simulation, helical flow is initiated by adding up viscous flow and vorticity at initial conditions. Formation of helical flow is generated at downstream hemispheres part of the curved channel. Helical flow pattern from SPH model can be compared with helical flow patterns from RMA model. The helical flow pattern is consistent with the patterns from very recently experiment investigation by Wang and Liu (2015), and theoretical sketch of secondary flows in a curved channel by Wu (2008). Thus, SPH method is able to develop helical flow as a result of curvature, agreed with Camporeal et al. (2007), and even without sediment transport, agreed with da Silva (2006) and Yalin (1993). Our contribution with this research is developing SPH method for modeling helical flow in a curved channel with the aim of simulating meandering dynamics. This is all along with advancement of SPH in Hydraulics where four grand challenges in SPH applications, according to SPHERIC community (Violeau & Rogers, 2015), are convergence, numerical stability, boundary conditions, and adaptivity. This research participates to the two of SPH challenges; boundary conditions and adaptivity. We used simple geometries based on Snell's law to represent basic particle responses to channel walls. We adapted SPH for nearly incompressible flow as a basic hydraulics phenomenon in a curved channel that is note bene an incompressible flow.

Keywords: smoothed particle hydrodynamics, RMA, helical flow, 3D fluid flow simulation, curved channel, meandering

RÉSUMÉ DE THÈSE

Méandres se produire même sans le transport des sédiments, elle est causée par une turbulence à grande échelle (da Silva, 2006). La recherche de méandre des chaînes en général est séparé, mais toujours corrélée, en deux approches : la dynamique géomorphologiques et fluide, où la modélisation des flux 3D reçoivent plus d'attention pour sa capacité à simuler le mouvement hélicoïdal, même si elle est élevée dans les efforts de calcul et limitée à une géométrie simple (Camporeal, et al, 2007). Un modèle développé avec un finis méthodes d'éléments pour l'écoulement en trois dimensions est appelé Resource Modelling Associates (RMA), pour modéliser ; flux de densité stratifié (RMA-10), et la qualité de l'eau dans les estuaires et les ruisseaux (RMA-11) (King, 2013). Smoothed particle hydrodynamics (SPH) est une méthode libre de maille la plus perceptible et devenu très populaire, en particulier pour les flux de surface libre, il est une méthode robuste et puissant pour décrire les médias déformation (Gomez-Gesteira, et al, 2010). SPH est une méthode très prometteuse pour répondre à la modélisation des flux 3D dans le dynamique méandre. Objectif de cette recherche est modèles d'écoulement hélicoïdaux de simulation d'écoulement avec 3D méthode SPH d'écoulement presque incompressible est comparable à écouler simulation avec écoulement stratifié 3D méthode des éléments finis. Approches dans cette recherche est divisé en deux grandes parties ; (1) modélisation du dynamique méandre avec RMA afin de déterminer ses caractéristiques de base, et (2) développement de la méthode de SPH pour simuler l'écoulement hélicoïdal dans un canal. Modèle éléments finis utilisé dans cette étude, RMA a montré sa capacité à simuler les caractéristiques clés de méandres et sont convenus avec les expériences de Hasegawa (1983), et Xu et Bai (2013). Ces résultats sont utilisés comme référence pour développer le modèle du dynamique méandre. Procédures de SPH sont élaborées à partir du modèle d'écoulement du fluide 3D, gestion des collisions entre les particules de l'eau, et des conditions aux limites de canal courbes. La caractéristique fondamentale dans le dynamique méandre est écoulement hélicoïdal. Avec simulation de SPH, écoulement hélicoïdal est initiée par l'addition des flux de tourbillon et visqueux aux conditions initiales. Formation d'écoulement hélicoïdal est généré en hémisphères partie aval du canal courbé. Motif d'écoulement hélicoïdal à partir du modèle SPH peut être comparé avec des modèles de flux hélicoïdaux de modèle RMA. Le modèle d'écoulement hélicoïdal est compatible avec les modèles de l'investigation très récente de l'expérience par Wang et Liu (2015), et l'esquisse théorique de flux secondaires dans un canal courbe par Wu (2008). Ainsi, SPH est capable pour développer écoulement hélicoïdal du fait de la courbure, d'accord avec Camporeal et al. (2007), et même sans le transport des sédiments, convenu avec da Silva (2006) et Yalin (1993). Notre contribution en présente recherche est le développement de la méthode SPH pour la modélisation de l'écoulement hélicoïdal dans un canal courbé dans le but de simuler le dynamique méandre. Ceci est tout le long avec l'avancement de SPH en hydraulique où quatre grands défis dans les applications de SPH, selon la communauté SPHERIC (Violeau et Rogers, 2015), sont la convergence, la stabilité numérique, la condition limite, et l'adaptabilité. Cette recherche participe aux deux défis de SPH ; la condition limite et l'adaptabilité. Nous avons utilisé des géométries simples basées sur la loi de Snell pour représenter la réponse basique des particules du mur de canal courbé, et adapté SPH pour flux presque incompressible comme un phénomène basique de l'hydraulique dans un canal courbé qui est note bene un flux incompressible.

Mots-clés: smoothed particle hydrodynamics, RMA, écoulement hélicoïdal, simulation d'écoulement du fluide 3D, canal courbé, les méandres

ACKNOWLEDGEMENT

Alhamdulillah

I am deeply grateful to my supervisors, Herr Soeryantono, PhD, Prof. Erick Carlier, and Dr-Ing. Dwita Sutjiningsih, for all their understanding, encouragement and guidance.

I wish to express my sincere thanks to Prof. Iwan Kridasantausa Hadihardaja and Prof. Hassan Smaoui for having accepted to be external examiners of my dissertation, Prof. Isam Shahrour for accepting me in LGCgE, also to Prof. Dedi Priadi for chairing the jury, and of course Dr. Ahmad Indra Siswantara and Alhadi Bustaman, PhD for your time to be the jury in my doctoral defense.

My thanks especially to my mother Ir. Tintin Komariah, and my youngest brother, Bayu Aji Nanto, who have always been available and ready to lend me a helping hand, and in memory of my father Ir. Wignyo Husodo (alm).

TABLE OF CONTENTS

DEVELOPING SMOOTHED PARTICLE HYDRODYNAMICS METHOD TO MODEL BASIC CHARACTERISTICS OF MEANDERING DYNAMICS	i
ABSTRACT	v
RÉSUMÉ DE THÈSE	vi
ACKNOWLEDGEMENT	vii
TABLE OF CONTENTS	ix
TABLE OF FIGURES	xi
LIST OF TABLE	xiii
1 INTRODUCTION	1
1.1 RATIONAL	1
1.2 RESEARCH OBJECTIVES	2
1.3 RESEARCH APPROACHES	2
1.4 RESEARCH LIMITATION	5
1.5 WRITING LAYOUT	5
2 BASIC CHARACTERISTICS OF MEANDERING DYNAMICS	7
2.1 MEANDERING PHYSICAL PROCESSES	7
2.2 MEANDERING BENDS	8
2.2.1 FLOW STRUCTURES	8
2.2.2 EROSION, DEPOSITION AND BEND MIGRATION	12
2.3 MEANDERING FLOW BASIC CHARACTERISTICS	13
3 FLOW SIMULATIONS WITH RMA	15
3.1 NUMERICAL EXPERIMENT WITH RMA (RESOURCES MODELING ASSOCIATIONS)	15
3.1.1 RMA-10 DESCRIPTION MODEL	15
3.1.2 EQUATIONS OF STATE	20
3.1.3 RMA-11 DESCRIPTION MODEL	20
3.2 MODEL SET UP	27
3.2.1 MEANDER GEOMETRY	29
3.2.2 MESH GENERATING AND BED DEFORMATION	30
3.2.3 SIMULATION THREE-DIMENSIONAL FLOW	31
3.2.4 SIMULATION THREE-DIMENSIONAL SEDIMENT TRANSPORT	35
3.3 RESULTS AND DISCUSSION	38
3.4 RESULTS COMPARISONS FOR MODEL VERIFICATION	47
4 SPH METHOD	53

4.1	BASIC FORMULATION	53
4.1.1	INTEGRAL REPRESENTATION AND SMOOTHING FUNCTION.	54
4.1.2	PARTICLE APPROXIMATION.....	55
4.2	SPH PROCEDURE FORMULATIONS	56
4.2.1	FLOW EQUATIONS.....	56
4.2.2	PARTICLE APPROXIMATION FOR MEANDERING FLOW EQUATIONS.....	57
4.2.3	SMOOTHING FUNCTION (KERNEL).....	58
4.2.4	BOUNDARY CONDITIONS AND INITIAL CONDITIONS.....	60
5	FLOW SIMULATIONS WITH SPH	63
5.1	3D FLUID FLOW MODEL	63
5.2	NUMERICAL SIMULATION	66
5.2.1	PARAMETERS AND PROPERTIES.....	66
5.2.2	BOUNDARY CONDITIONS.....	69
5.2.3	INITIAL CONDITIONS.....	77
5.2.4	FLOW SIMULATIONS IN CURVED CHANNEL.....	78
5.3	RESULTS DISCUSSION	87
5.3.1	RESULTS COMPARISON.....	99
6	CONCLUSIONS AND CONTRIBUTIONS	105
6.1	CONCLUSIONS	105
6.2	RESEARCH CONTRIBUTIONS	106
6.3	SUGGESTIONS FOR FUTURE RESEARCH	107
	REFERENCES	109

TABLE OF FIGURES

Figure 1-1. Research approaches.....	3
Figure 1-2. Logical frame work.....	4
Figure 2-1. Scheme of the main processes involved in the meandering dynamics and their interactions (Camporeal, et al., 2007)	7
Figure 2-2. Schematic representation and location of convergence-divergence flow and bed erosion-deposition zones (da Silva, 2006).....	9
Figure 2-3. Sketch of flow mechanisms within flooded meandering channels (a) strong floodplain flow (Ervine, et al., 1993), and (b) weak floodplain flow (Wormleaton & Ewunetu, 2006).	11
Figure 2-4. Flow in river bends (Julien, 2002).	12
Figure 2-5. (a) Coordinate systems and (b) secondary flows in a curved channel (Wu, 2008).....	13
Figure 2-6. Basic characteristics meandering process.....	13
Figure 3-1. Definition sketch of a meander geometry and bed depth contour. Unit in x and y directions are in meters.....	29
Figure 3-2. Meshing elements, bed depth contours and continuity lines for deviation angles: (a) 30°, (b) 70°, and (c) 110°	30
Figure 3-3. RMA-10 input setting for meander with deviation angle 30°, and hydrograph inflow	34
Figure 3-4. RMA-11 input setting for meander with deviation angle 30°	36
Figure 3-5. Cohesive sediment parameters in R4Q file.....	37
Figure 3-6. Non-cohesive sediment parameters in R4Q file	38
Figure 3-7. Flow structures	40
Figure 3-8. Bed depths	44
Figure 3-9. Non-cohesive (Sand) sediment concentrations.....	45
Figure 3-10. Flow convergence-divergence zones schematic representation (a and b), and measured bed topography illustration by (c) Makaveyev (1975) and (d) Jackson (1975) (da Silva, 2006).....	47
Figure 3-11. Flow structures in small deflection angle channel (a) computed by RMA, (b) run ME-2 measured by Hasegawa (1983), and (c) run RUN30-1 measured by Xu and Bai (2013).....	48
Figure 3-12. Flow structures in large deflection angle channel (a) computed by RMA, and (b) run RUN110-2 measured by Xu and Bai (2013)	49
Figure 3-13. Flow structures in small deflection angle channel (a) computed by RMA, and (b) test case ME-2 Hasegawa (1983) by Dai (2008)	50
Figure 3-14. Flow structures in medium deflection angle channel (a) computed by RMA, and (b) test case #3 Binns (2006) by Dai (2008).....	51
Figure 3-15. Flow structures in large deflection angle channel (a) computed by RMA, and (b) test case Termini (1996) by Dai (2008)	52
Figure 4-1. Smoothing kernel functions: poly6 (w8(r)), spiky (w9(r)), viscosity (w10(r))	58
Figure 5-1. Process description for (a) the general algorithm, and (b) collision handling algorithm	63
Figure 5-2. Fluid flow program flow chart.....	65
Figure 5-3. Runtime versus particle number	67

Figure 5-4. At $t = 100 dt$, (a) Density Response (left to right) Due to the Difference of Rest Density 100 kg/m^3 , 1000 kg/m^3 , 10000 kg/m^3 ; (b) Pressure Response (left to right) Due to the Difference of Rest Density 100 kg/m^3 , 1000 kg/m^3 , 10000 kg/m^3	67
Figure 5-5. At $t = 100 dt$, (a) Density Response (left to right) Due to the Difference of Initial Velocity ($v_x = 10 \text{ m/s}$, $v_y = 10 \text{ m/s}$, $v_z = 10 \text{ m/s}$; (b) Pressure Response (left to right) Due to the Difference of Rest Initial Velocity ($v_x = 10 \text{ m/s}$, $v_y = 10 \text{ m/s}$, $v_z = 10 \text{ m/s}$	68
Figure 5-6. Particle interactions with plane area	69
Figure 5-7. Particle interactions with cylindrical wall	70
Figure 5-8. Boundary conditions for a curved channel	71
Figure 5-9. Particle interactions with curved channel flow chart (part 1 of 4).....	74
Figure 5-10. Initial condition for particle interactions with curved channel plan and 3D view	77
Figure 5-11. Checking angle refraction for a particle interaction in a curved channel plan view with gravity presence (upper row), and gravity absence (lower row)	78
Figure 5-12. Angle refraction for a particle interaction in a curved channel 3D view with gravity presence (left), and gravity absence (right).....	79
Figure 5-13. Transient inviscid flow simulation at $t = 15 \text{ s}$ in a curved channel plan view with gravity presence (left), and gravity absence (right)	80
Figure 5-14. Transient inviscid flow simulation at $t = 15 \text{ s}$ in a curved channel 3D view with gravity presence (upper), and gravity absence (lower)	80
Figure 5-15. Viscous velocity profile (left) at $z = 0.667 \text{ meter}$, (right) at $x = 0.50 \text{ meter}$	81
Figure 5-16. Transient viscous flow simulation at $t = 15 \text{ s}$ in a curved channel plan view with gravity (left) presence, and (right) absence	82
Figure 5-17. Transient viscous flow simulation at $t = 15 \text{ s}$ in a curved channel 3D view with gravity (upper) presence, and (lower) absence.....	82
Figure 5-18. Viscous velocity profile in [m/s] (left) at $z = 0.667 \text{ meter}$, (middle) $y = 0.5 \text{ meter}$, and (right) at $x = 0.50 \text{ meter}$	83
Figure 5-19. Transient viscous vorticity flow simulation at $t = 15 \text{ s}$ in a curved channel plan view with gravity (left) presence, and (right) absence	83
Figure 5-20. Transient viscous vorticity flow simulation at $t = 15 \text{ s}$ in a curved channel 3D view with gravity (upper) presence, and (lower) absence	84
Figure 5-21. Flow simulation with 1% of gravity magnitude in plan view (left) with vorticity, and (right) without vorticity.....	85
Figure 5-22. Flow simulation with 1% of gravity magnitude in 3D view (upper) with vorticity, and (lower) without vorticity	85
Figure 5-23. Flow simulation with 100 times of viscosity, mass, and surface tension magnitude in plan view (left) with vorticity, and (right) without vorticity	86
Figure 5-24. Flow simulation with 100 times of viscosity, mass, and surface tension magnitude in 3D view (left) with vorticity, and (right) without vorticity	86
Figure 5-25. Particle flows with water properties from $t = 0, 3, 6, 9, 12$, and 15 second (from upper left in clockwise direction); colors represent velocity [m/s]	87
Figure 5-26. Particles collision handling (upper left) with gravity, (upper right) with 1% * gravity, (lower left) without gravity, and (lower right) with 10% mass; colors represent velocity [m/s].....	88
Figure 5-27. Particles collision handling in curved channel with 1% gravity, initial inviscid flow, time 14 seconds in 3D view, time step 1 s, each color represents velocity [m/s]	91

Figure 5-28. Particles collision handling in curved channel with 1% gravity, initial inviscid flow, time 14 seconds for cross sections at the hemispheres	92
Figure 5-29. Particles collision handling in curved channel with 1% gravity, initial vorticity flow, time 6.5 seconds in 3D view, time step 0.5 s, each color represents velocity [m/s].....	93
Figure 5-30. Particles collision handling in curved channel with 1% gravity, initial vorticity flow, time 6.6 seconds for cross sections at the hemispheres	94
Figure 5-31. Particles collision handling with curved channel with 1% gravity, initial viscous flow, time 15 seconds in 3D view, time step 1 s, color represents velocity [m/s]	95
Figure 5-32. Particles collision handling with curved channel with 1% gravity, initial viscous flow, time 15 seconds for cross sections at the hemispheres.....	96
Figure 5-33. Particles collision handling with curved channel with 1% gravity, initial viscous vorticity flow, time 8 seconds in 3D view, time step 0.5 s, color represents velocity [m/s].....	97
Figure 5-34. Particles collision handling with curved channel with 1% gravity, initial viscous vorticity flow, time 8 seconds for cross sections at the hemispheres	98
Figure 5-35. Helical formation with initial vorticity viscous flow simulation at $t = 6.5$ seconds; colors represent velocity [m/s].....	99
Figure 5-36. Helical formation with SPH simulation, initial vorticity viscous flow, and results at $t = 2.35$ seconds; colors represent velocity [m/s].....	100
Figure 5-37. Checking angle refraction for a particle interaction; colors represent velocity [m/s].....	101
Figure 5-38. Particles value of: (a) velocity [m/s], (b) pressure [Pa], and (c) density [kg/m ³].....	101
Figure 5-39. Helical formation with RMA simulation at $t = 1.5$ seconds; colors represent velocity [m/s]	102
Figure 5-40. Helical formation from experiment investigation of flow structures (Wang & Liu, 2015).....	102
Figure 5-41. Theoretical sketch of helical flows in a curved channel, modified from “flow structure past flood channel facility meanders” (Wormleaton & Ewunetu, 2006)	103

LIST OF TABLE

Table 3-1. Construction of input files (modified from King 1993).....	28
Table 3-2. Variables of meander geometry.	30
Table 3-3. Continuity lines coordinates at meander center lines.....	31
Table 3-4. Cross sections from upstream (1) to downstream (9).	41
Table 3-5. Bed Shear Stress	43
Table 5-1. Parameter properties	66
Table 5.2. Simulation Cases	89

1 INTRODUCTION

1.1 RATIONAL

M. S. Yalin defines meandering as “*self-induced* plan deformation of a stream that is (ideally) periodic and anti-symmetrical with respect to an axis, x say, which may or may not be exactly straight” (Yalin, 1992). Meanders occur even without sediment transport, it is caused by a large-scale turbulence (da Silva, 2006), turbidity current as in submarine meanders (Darby & Peakall, 2012), and trailing vortices as in low-frequency meander in wind tunnels (Beresh, et al., 2010). Characteristics of flow in meanders are three-dimensional (3D), turbulent, and the presents of helical flow (Wu, 2008).

Meandering channels research in general separated, but still correlated, into two approaches: geomorphologic and fluid dynamics, where 3D flow modeling receive more attention for its ability to simulate helicoidal motion even though it is high in computational efforts and limited to simple geometry (Camporeal, et al., 2007). However computer’s capability is growing hence meandering channel can be simulated with a powerful computational fluid dynamics (CFD) tools such as direct numeric simulation (DNS), large eddy simulation (LES), or $\kappa - \epsilon$ models (Wormleaton & Ewunetu, 2006).

CFD is traditionally using grid-based numerical methods, such as finite element methods (FEM) and finite volume methods (FVM), which have gained high acceptance ((Bates, et al., 2005), and (Wendt, 2009)). One developed model with a finite element methods for three-dimensional flow is called Resource Modelling Associates (RMA), to model; density stratified flow (RMA-10), and water quality in estuaries and streams (RMA-11) ((King, 2013), (King, 2012), and (King, 1993)). It is suited for computing the hydrodynamics of shallow water flow and limited to uniform sediment (Papanicolaou, et al., 2008).

In spite of its success, grid-based method has limitations whenever dealing with free surface, deformable boundary, moving interface, and extremely large deformation and crack propagation because of the use of mesh. Complex geometry problems make generating mesh is hard, expensive, and laborious (Liu

& Liu, 2010). Meshfree methods has been emerged as an alternative grid based methods to deliver better accuracy and stability numerical solutions for PDEs with all possible boundary conditions using particles (Liu & Liu, 2003).

Smoothed particle hydrodynamics (SPH) is one most noticeable meshfree method and now become very popular, particularly for free surface flows, it is a robust and powerful method for describing deforming media (Gomez-Gesteira, et al., 2010). SPH main appeals are its ability to predict highly strained motions based on a set of particles, and its consistency with Lagrangian and Hamiltonian mechanics in terms of conservativity (Violeau, 2012). SPH applications for incompressible or nearly incompressible flow in the last two decades is diverse involving dam breaks and plunging waves, gravity currents and multifluid phenomenon, bodies moving in fluids, non-Newtonian fluids, surface tension, and diffusion and precipitation (Monaghan, 2012). Advanced hydraulics with SPH so far has been covered wave action upon waterworks, fish pass, floating oil spill containment boom, and dam spillway (Violeau, 2012). SPH is also a hot topic in Computer Graphics (Kelager, 2006) including realistically animated fluids (Müller, et al., 2003), fluid-fluid interaction (Müller, et al., 2005), hydraulics erosion (Kristof, et al., 2009), and 2D shallow water simulation (Solenthaler, et al., 2011).

SPH researches in CFD, hydraulics, and computer graphics mostly do not focus on flow structures except in turbulence. Thus, SPH is a very promising method to answer 3D flow modeling in meander dynamics.

1.2 RESEARCH OBJECTIVES

Helical flow patterns from flow simulation with 3D nearly incompressible flow SPH method is comparable to flow simulation with 3D stratified flow finite element method.

1.3 RESEARCH APPROACHES

This research comprises two big parts; (1) modeling meander dynamics with RMA (Resources Model Association), a 3D stratified flow finite element model, to determine its basic characteristics, and (2) development smoothed particle

hydrodynamics (SPH) method for 3D nearly incompressible flow to simulate helical flow in a curved channel.

Approaches used in part (1) are:

- 1) modeling sediment transport due to helical flow in meandering river,
- 2) investigating channel geometries and its relation to the development of helical flows,
- 3) predicting location of convergence-divergence flow zones and erosion and deposition zones,
- 4) simulating sediment transport process due to coherent structures and burst in meandering river, and
- 5) modeling eroding process as mechanical interaction fluid-soil at river bank.

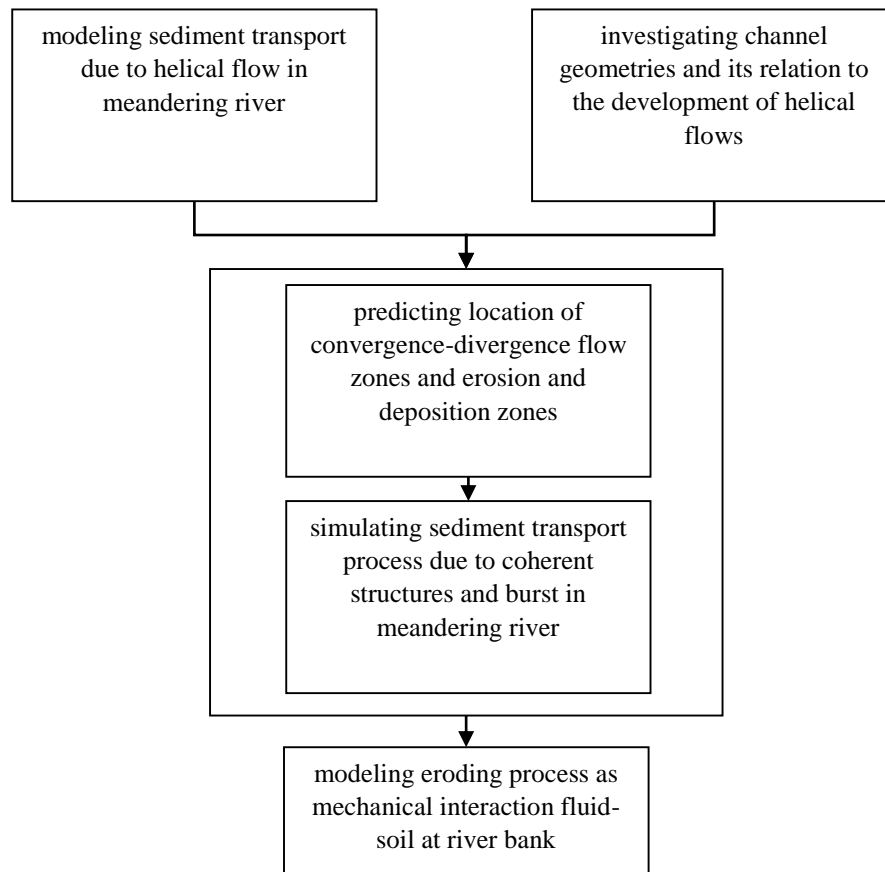


Figure 1-1. Research approaches

In part (2), development a FORTRAN code of SPH procedure to simulate helical flow in curved channel follows a logical frame work as in Figure 1-2.

Physical phenomenon is interpreted in mathematical formulation and represented as governing equations. Numerical method is chosen to find the equations solutions. Algorithm is developed to express the work flow and written in program code. The program run through evaluation until produce results as we expect. If the solutions do not satisfy the objective of the program development, then we have to adjust the parameter. If the solutions do satisfy, then we interpret the results. From result interpretation we can verify and/or validation. According to ISO 9001:2000 section 7.3, designs need to be verified and validated. Verification is defined as the conformation that a product meets identified specifications, and validation is the conformation that a product appropriately meets its design function or the intended use.

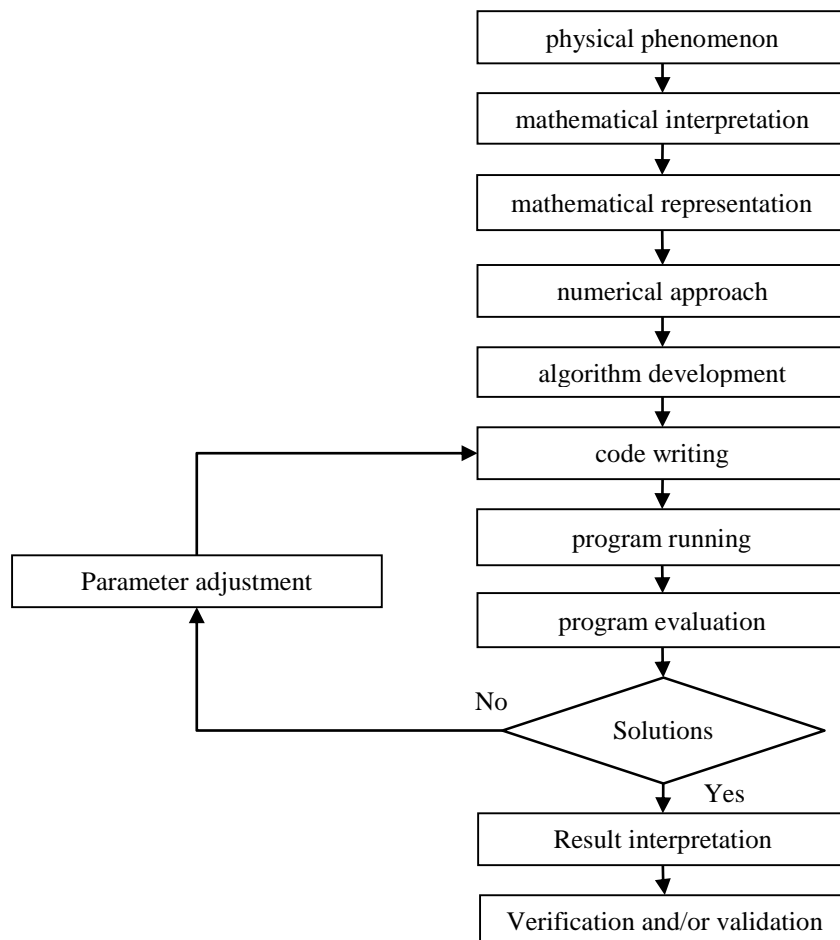


Figure 1-2. Logical frame work

1.4 RESEARCH LIMITATION

This research is limited to:

- 1) 3D stratified flow finite element method with RMA based on shallow water approach
- 2) turbulence closure with Smagorinsky closure in RMA-10 model
- 3) non-cohesive sediment transport in RMA-11 model
- 4) sine-generated curves for meander geometry representative with RMA model
- 5) 3D nearly compressible flow for SPH model development
- 6) turbulence and sediment transport that are not considered yet
- 7) a curved channel as meander geometry representation with SPH model
- 8) verification by comparing the results to experimental researches of Hasegawa (1983), Xu & Bai (2013), and Wang & Liu (2015).

1.5 WRITING LAYOUT

This dissertation writing is divided into two parts in general. The first one is to model meander dynamics with RMA-10 AND RMA-11 to determine its basic characteristics, and written in chapter 2 and 3. This part is prepared in Laboratoire de Génie Civil et géo-Environnement, Ecole Polytechnique de Lille, Université de Lille 1, France. The last one is to develop smoothed particle hydrodynamics (SPH) method to simulate helical flow in a curved channel, and presented in chapter 4 and 5. This part is done in Laboratory of Hydraulics, Hydrology and River, Civil Engineering Department, Universitas Indonesia, Indonesia.

Chapter 2 writes about fundamental theory of meandering physical processes, and flow structure, erosion-deposition and bend migration in meandering bends. In the end, this chapter wrap up meandering flow basic characteristics.

Chapter 3 presents flow simulations with RMA from description model, model set-up, results and discussion, and lastly results confirmation with other experimental studies in meandering channel.

From chapter 2 and chapter 3, we have published (1) a paper in International Conference Sediment Transport Modeling in Hydrological Watersheds and Rivers, Istanbul, Turkey, 2012, titled 'Developing model to predict curve

dynamics in river meandering process'; and (2) a paper in Journal of Urban and Environmental Engineering (JUEE) Vol 8, No 2, 2014, titled 'Assessment of the capability of 3D stratified flow finite element model in characterizing meander dynamics', DOI: 10.4090/juee.2014.v8n2.155166.

Chapter 4 describes SPH method, opening with basic formulation, and closing in procedure formulation.

Chapter 5 composes flow simulations with SPH from 3D fluid flow model, numerical simulation, and finally results discussion.

Chapter 6 completes this writing by reviewing conclusions, research contributions, and suggestions for future research.

Based on chapter 4 and chapter 5, we have published (1) a paper in International Conference on Ecohydrology, Yogyakarta, Indonesia, 2014, titled 'Reviewing the use of smoothed particle hydrodynamics as a tool in modeling river meandering', ISBN: 978-979-8163-22-7, and (2) we plan afterwards to publish a paper in an international journal with tentatively title 'Development of smoothed particle hydrodynamics (SPH) method to simulate helical flow in a curved channel'.

2 BASIC CHARACTERISTICS OF MEANDERING DYNAMICS

Einstein firstly explained the cause of the formation of meanders in 1926 where streams tend to flow in winding and turning course instead of following the downward slope as a result from Coriolis-force (Einstein, 1926). Even without bends, the circular movement still exists at cross-sections of its course. Meandering is not only happened on alluvial streams but also on melting water channels on ice (Langbein & Leopold, 1966), wind tunnels (Beresh, et al., 2010), and submarine channels (Darby & Peakall, 2012).

2.1 MEANDERING PHYSICAL PROCESSES

River is meandering when there is an active process of erosion at the outer bank and deposition on the inner bank (Raudkivi, 1998). Camporeal et al. (2007) in Figure 2-1 present the main elements of meandering dynamics are curvature and erodible boundary. Each of main elements can drive secondary currents then leads to transversal flow field.

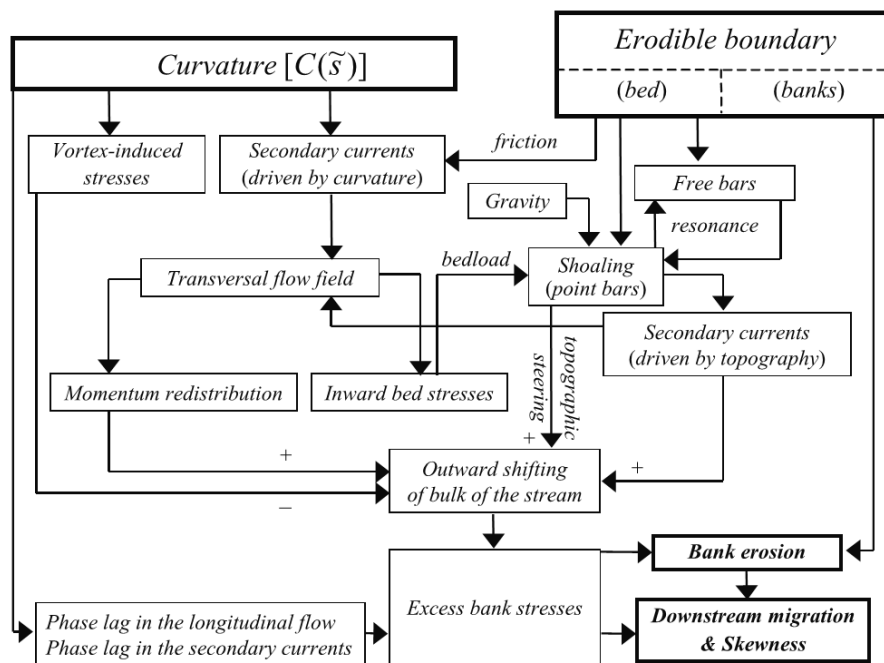


Figure 2-1. Scheme of the main processes involved in the meandering dynamics and their interactions (CAMPORREAL, ET AL., 2007)

2.2 MEANDERING BENDS

In river modeling is often used one-dimensional model due to efficiency and applied in the study of long-term sedimentation problems in rivers. But flows in curved channels give evidence of complex three-dimensional features that have big influences on sediment transport process. Thus these phenomena must rely on three-dimensional model for all practical purposes. To simulate correctly channel meandering process, at least a model must be capable of; (1) taking into account the helical flow effect, (2) dealing with bank erosion, and (3) coping with the moving boundary problems. Erosion mechanisms vary with bank material. The bank material fails in blocks for a cohesive bank, and it fails in particles for a non-cohesive one (Wu, 2008).

Here, the river scale is defined as reach scale where the domain is longer than the channel by a factor of at least 5 and up to 50 or more. Considering that reach scale is a common scale in management activities such as scour around bridge piers, in-channel sedimentation process, bank erosion and channel migration, thus it relates the flow and sediment transport around structures, and linkages strongly to morpho-dynamic and habitat process likewise the flow field itself (Bates, et al., 2005).

2.2.1 FLOW STRUCTURES

In curved channel, the dispersion transport plays great role due to helical flow. The existence of helical flow is caused by the difference between the centrifugal forces in the upper and lower layers (Wu, 2008). More fundamental explanation is the physical reasoning of meandering phenomenon. Recent research explained that meandering is caused by the large-scale turbulence where is designated to bursting processes (da Silva, 2006).

da Silva and Ahmari (2009) found that the formation of large-scale river forms is directly related to the large-scale turbulence, particularly the formation of alternate bars and meanders through the actions of horizontal coherent structures on the mean flow and the mobile bed and banks (da Silva & Ahmari, 2009). This is agreed with Mao (2003) experiments that at high roughness Reynolds number the bursts and sweeps phenomena can send sediment particles into suspension where bed forms and bed roughness interact with the coherent

turbulent structures and resulted in flow and sand movement in alluvial rivers (Mao, 2003). The most recent result comes from (Esfahani & Keshavarzi, 2012), they detected the importance of sweeps and bursts on sediment deposition, and stated the occurrence of fluctuating velocities in three-dimensions inside meanders is responsible for sediment transport.

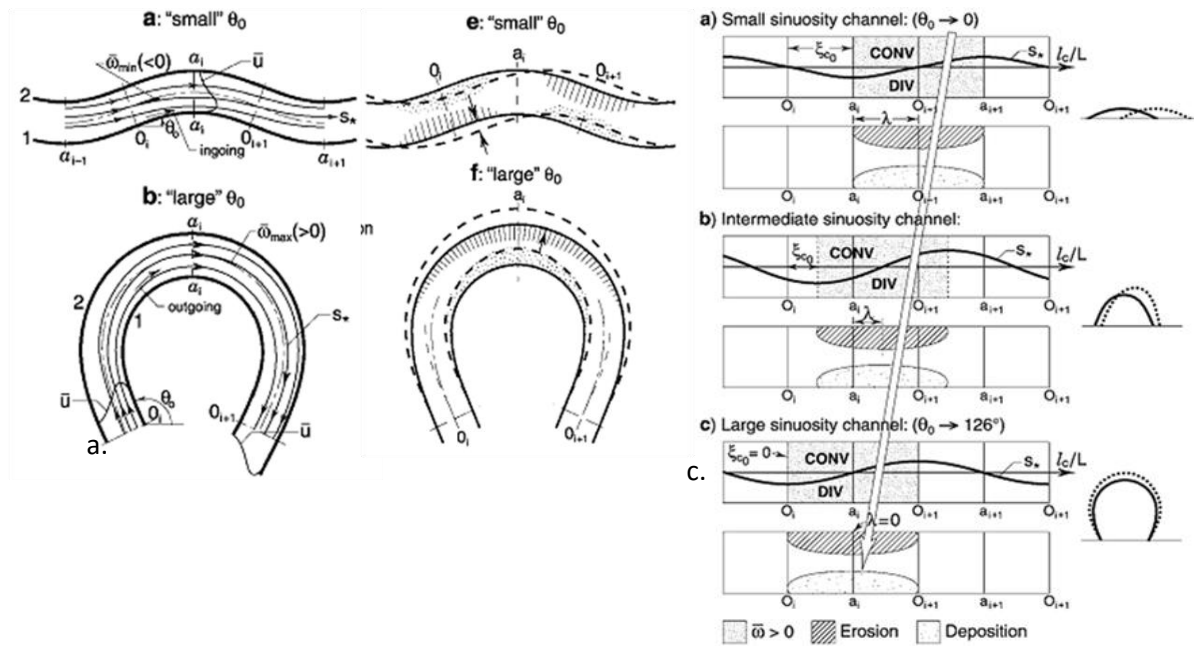


Figure 2-2. Schematic representation and location of convergence-divergence flow and bed erosion-deposition zones (DA SILVA, 2006)

If we assume the ratio of channel width to its depth is large, then we can consider the flow in meandering river is vertically averaged and convective as shown by in Figure 2-2 (da Silva, et al., 2006). In the sine-generated channels, da Silva et al. stated that the flow is accelerating where the vertically averaged streamlines are converging to each other, and decelerating where the vertically averaged streamlines are diverging from each other. From their experiments, for small deflection angles (30°) location of maximum erosion-deposition zones near the crossover of the sinuosity, for intermediate deflection angles (70°) location of maximum erosion-deposition zones between the crossover and apex of the sinuosity, and for large deflection angles (110°) location of maximum erosion-

deposition zones near the apex of the sinuosity. Esfahani & Keshavarzi (2012) investigated different deflection angles affected on fluctuation velocities that is responsible for direction of sediment deviation and then migration pattern. They have the same opinion that convergence-divergence regions coincide with erosion-deposition regions (Esfahani & Keshavarzi, 2012).

As erosion-deposition zones coincide with the convergence-divergence flow zones in meandering river, we can predict the zones of convective acceleration and deceleration of flow, and the zones of upward and downward bed displacements by examining velocity, depth distributions, meander wavelength, and plan shape of meandering river ((Odgaard, 1989) and (da Silva, 2006)).

Turbulence consists of coherent (phase-correlated) and phase-random (i.e., incoherent) motions. A coherent structure is a connected, large-scale turbulent fluid mass with a phase-correlated vorticity over its spatial event (Hussain, 1983). Coherent structure is used to point out the largest cluster of turbulent eddies which has the most common sense of rotation. The term burst is to appoint the evolution of coherent structures during its life span (da Silva, 2006). As mentioned by (Sanjou & Nezu, 2009), velocity inflection-point instability, i.e. shear instability, occurs at the meandering entrance, suggesting the generation of a horizontal vortex. Whether such a vortex is surely generated and how it is convected in the meandering channel is not yet clear. The combination between horizontal vortex and secondary currents may promote significant mass and momentum exchanges at the interchanging boundaries near main channel bed and near free surface.

Coherent turbulence structures in meanders, bursts and sweeps, are responsible for transferring fluid momentum across local velocity gradients (da Silva & Ahmari, 2009). Bursts are oriented towards inner-bank and sweeps are oriented towards outer-bank of the channel bend (Güneralp, et al., 2012). According to Güneralp et al. (2012), coherent turbulent structures may be regarded as temporal imbalances in the cross-section force equilibrium combined with turbulent structures movement, and changes in the mean cross-section velocity through the water column joined with secondary currents.

Ervine et al. (1993) shows in Figure 2-2 the importance of flow mechanisms in meandering over-bank flow based on their measurements. From floodplain or outer-bank, flow moves toward main channel as a large secondary flow which is vigorously expulsion of inner-bank. Then secondary flow decays right after bend apex. Afterwards, primary flow proceeds to the next bend, and converges with strong vortex from floodplain.

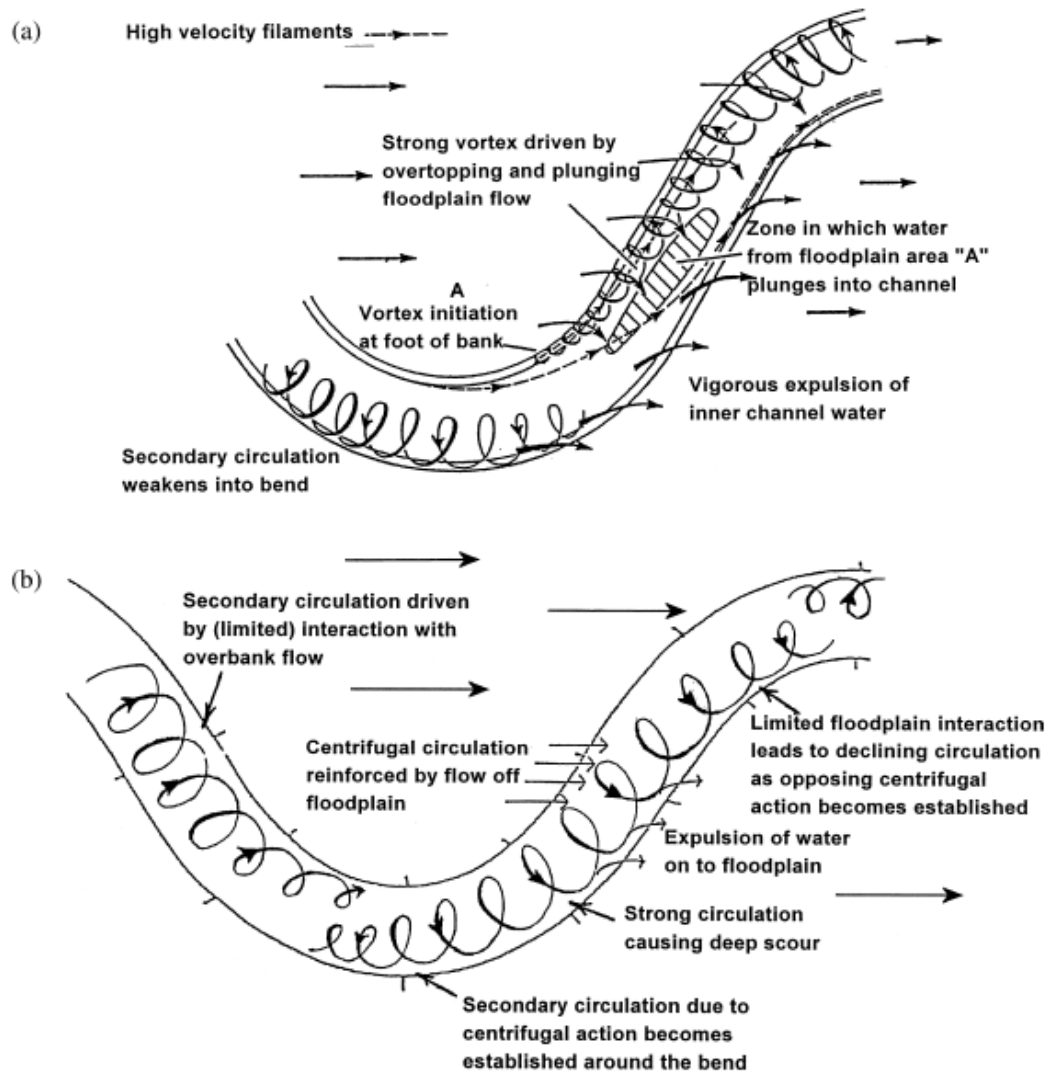


Figure 2-3. Sketch of flow mechanisms within flooded meandering channels (a) strong floodplain flow (ERVINE, ET AL., 1993), and (b) weak floodplain flow (WORMLEATON & EWUNETU, 2006).

2.2.2 EROSION, DEPOSITION AND BEND MIGRATION

In theory of river basins, river process can be divided into three main zones; (1) erosion at the upper zone, (2) transportation at the mid zone, and (3) deposition at the lower zone. As a fluvial system, those zones are characterized by sediment process, bed elevation, channel pattern, slope, and bed material. At the upper zone, it is typically erosion process, degradation bed, confluence channel, steep slope, and bed material of cobble – gravel. At the mid zone, it is commonly transportation process, equilibrium bed, single channel, mild slope, and bed material of gravel – sand. The last part, it is expected sedimentation process, aggradation bed, branching channel, flat slope, and bed material of sand – silt. Alluvial rivers flow with their own deposits. Its equilibrium channel leads to a balance between incoming and outgoing water discharge and sediment load. The cross-sectional geometry may change at local on condition that the deposition volume within a river reach is equal to the erosion volume. Consequently at river bends, its cross-sectional geometry is in equilibrium. Nevertheless, lateral migration of the bend indicates instability of the stream planform geometry (Julien, 2002).

Deviation angle λ depends primarily on the ratio of flow depth to radius of curvature thus sharp bends will exhibit stronger secondary flows (Julien, 2002). It is expressed in:

$$\tan \lambda = \frac{\tau_r R}{\tau_\theta} = \left[\frac{a^2}{\Omega_R} \left(\frac{h}{d_s} \right)^{2m} \right] \frac{h}{R} \quad (2-1)$$

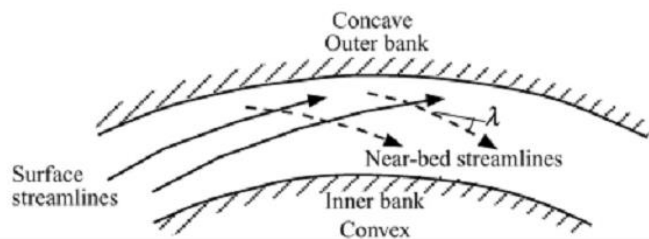


FIGURE 2-4. FLOW IN RIVER BENDS (JULIEN, 2002).

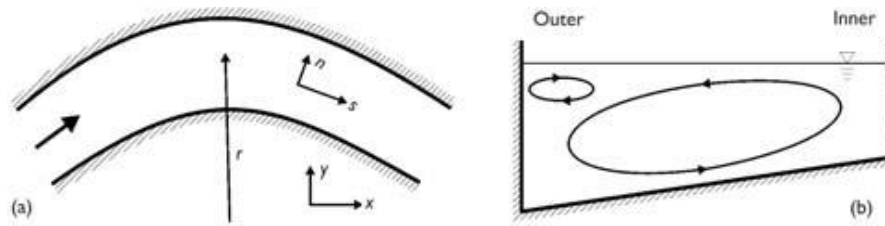


Figure 2-5. (a) Coordinate systems and (b) secondary flows in a curved channel (WU, 2008).

2.3 MEANDERING FLOW BASIC CHARACTERISTICS

Development of meander dynamics model has to have a capability to simulate meander flow characteristic and sediment transport distribution pattern, or at least having the same capability as the finite element method (Wu, 2008). Here, the meander flow is characterized by having helical flow and coherent structures (bursts and sweeps), higher flow velocity at the outer banks and lower in the inner banks, sediment erosion at the outer banks and deposition in the inner banks, higher sediment concentration at the outer banks and lower in the inner banks (da Silva, 2006).

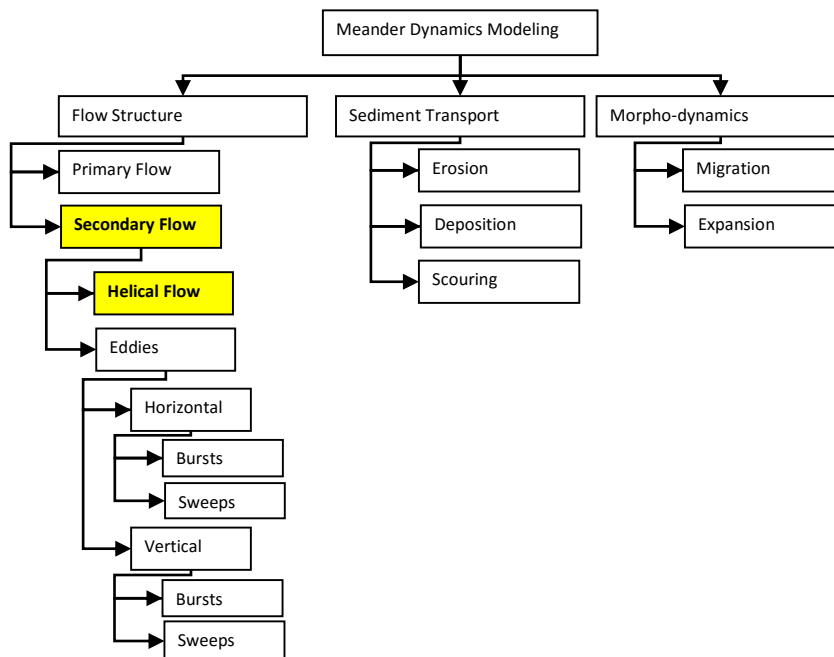


Figure 2-6. Basic characteristics meandering process

3 FLOW SIMULATIONS WITH RMA

3.1 NUMERICAL EXPERIMENT WITH RMA (RESOURCES MODELING ASSOCIATIONS)

The governing equations of RMA-10 is based on the combination of the Reynolds form of the Navier-Stokes equations, the volume continuity equation, the advection diffusion equation, and an equation of state relating water density to salinity or temperature. For fully three-dimensional model, the required boundary conditions that must be defined here are water surface elevation, sediment concentration, sediment flux, and specified velocity at land and water boundaries. Practically it can be divided into three categories which are the free surface, the bed, and the side boundaries.

The finite element approach in RMA-10 is using iso-parametric approximations to define elements, Galerkin Method of Weighted Residuals for the finite element derivation, Newton-Rhapson method to structure and iterate for the nonlinearity, modified Crank-Nicolson time stepping scheme for unsteady flow, and Gaussian quadrature to integrate the finite element integrals. Hydrostatic pressure assumption is considered since vertical momentum effects may be neglected and the vertical velocities are sufficiently small ((King, 1993) and (King, 2012)). Here, we used RMA-10 version 87e in 20 November 2012.

RMA-11 is a finite element water quality model to simulate three-dimensional estuaries, bays, lakes and rivers as separate system or combined form. It employs the input of velocities and depths from RMA-10 for the computation of advection diffusion constituent transport equations with additional terms for each source/sink and growth/decay.

3.1.1 RMA-10 DESCRIPTION MODEL

3.1.1.1 Governing Equations for Three-Dimensional Stratified Flow

RMA-10 uses three-dimensional stratified flow equations describing velocity in all three Cartesian directions, water pressure and the distribution of constituent concentration of sediment throughout the system. The sediment is treated as the dependent variable.

Hydrodynamics approximation, or often called shallow water approximation, is widely used in surface water systems. Shallow water (or long wave) approximation assumes that ratio between horizontal (L) to vertical (L) scales is very large, or $\frac{H}{L} \ll 1$ (Ji, 2008).

$$\text{Volume Continuity: } \frac{\partial u_j}{\partial x_j} = 0 \quad (3-1)$$

$$\text{Momentum equation:} \quad (3-2)$$

$$\rho \left(\frac{\partial u_i}{\partial t} + u_j \frac{\partial u_i}{\partial x_j} \right) - \frac{\partial}{\partial x_j} \left(\varepsilon_{x_i x_j} \frac{\partial u_i}{\partial x_j} \right) + \frac{\partial p}{\partial x_i} - \Gamma_{x_i} = 0$$

$$\text{Advection Diffusion: } \frac{\partial c}{\partial t} + u_j \frac{\partial c}{\partial x_j} - \frac{\partial}{\partial x_j} \left(D_{x_j} \frac{\partial c}{\partial x_j} \right) - \theta_s = 0 \quad (3-3)$$

$$\text{Hydrostatic Approximation: } \frac{\partial p}{\partial z} + \rho g = 0 \quad (3-4)$$

where i, j are general coordinate directions as subscripts, u_j is the component vector velocity in j -direction, x_j is coordinate system in j -directions, ρ is density, $\varepsilon_{x_i x_j}$ is the turbulent eddy coefficients, u_i is the vector velocity in i -direction, t is for time, p is for pressure, Γ_x is external forces, c is constituent concentration, D_x is the eddy diffusion coefficients, and θ_s is the source/sink for the constituent. In the RMA-10 formulation of the vertical velocity w is used only in the two momentum equations and the advection diffusion equation. For the simulation model, the main dependent variables are thus the horizontal velocity components u and v , the water depth h and the constituent concentration c .

For equations (1) through (4), the geometric system varies with time where the water depth h varies during the simulation. In modifying the geometry the transformation is defined by a as the elevation of the bottom relative to the same vertical datum and b as the fixed vertical location to which the water surface will be transformed. To add in the impact of the transformation, the horizontal eddy coefficients have been modified but neglected the influence of slightly non horizontal diffusion induced by the transformation.

The final form for three-dimensional stratified flow that is used in RMA-10 are momentum equations (5) and (6), volume continuity equation (7), advection diffusion equation (8), and equation of state (9):

$$\rho \left\{ h \frac{\partial u}{\partial t} + hu \frac{\partial u}{\partial x} + hv \frac{\partial u}{\partial y} + \frac{\partial u}{\partial z} \left[(b-a)(w - uT_x - vT_y) - \right. \right. \quad (3-5)$$

$$\left. (z-a) \frac{\partial h}{\partial t} \right\} - (b-a) \frac{\partial}{\partial x} \left[\epsilon_{xx} \frac{h}{(b-a)} \frac{\partial u}{\partial x} \right] - (b-a) \frac{\partial}{\partial y} \left[\epsilon_{xy} \frac{h}{(b-a)} \frac{\partial u}{\partial y} \right] -$$

$$(b-a) \frac{\partial}{\partial z} \left[\epsilon_{xz} \frac{\partial u}{\partial z} \right] + \rho_s gh \frac{\partial a}{\partial x} + \rho_s gh \frac{\partial h}{\partial x} + g_x h - h\Gamma_x = 0$$

$$\rho \left\{ h \frac{\partial v}{\partial t} + hu \frac{\partial v}{\partial x} + hv \frac{\partial v}{\partial y} + \frac{\partial v}{\partial z} \left[(b-a)(w - uT_x - vT_y) - \right. \right. \quad (3-6)$$

$$\left. (z-a) \frac{\partial h}{\partial t} \right\} - (b-a) \frac{\partial}{\partial x} \left[\epsilon_{yx} \frac{h}{(b-a)} \frac{\partial v}{\partial x} \right] - (b-a) \frac{\partial}{\partial y} \left[\epsilon_{yy} \frac{h}{(b-a)} \frac{\partial v}{\partial y} \right] -$$

$$(b-a) \frac{\partial}{\partial z} \left[\epsilon_{yz} \frac{\partial v}{\partial z} \right] + \rho_s gh \frac{\partial a}{\partial y} + \rho_s gh \frac{\partial h}{\partial y} + g_y h - h\Gamma_y = 0$$

$$\int_a^b \left[\frac{\partial u}{\partial x} - \frac{(b-a)}{h} \frac{\partial u}{\partial z} T_x + \frac{\partial v}{\partial y} - \frac{(b-a)}{h} \frac{\partial v}{\partial z} T_y \right] dz + u_s \frac{\partial(a+h)}{\partial x} - u_b \frac{\partial(a)}{\partial x} + \quad (3-7)$$

$$v_s \frac{\partial(a+h)}{\partial y} - v_b \frac{\partial(a)}{\partial y} + \frac{\partial h}{\partial t} = 0$$

$$h \frac{\partial c}{\partial t} + hu \frac{\partial c}{\partial x} + hv \frac{\partial c}{\partial y} + \frac{\partial c}{\partial z} \left[(b-a)(w - uT_x - vT_y) - (z-a) \frac{\partial h}{\partial t} \right] - \quad (3-8)$$

$$(b-a) \frac{\partial}{\partial x} \left(D_x \frac{h}{(b-a)} \frac{\partial c}{\partial x} \right) - (b-a) \frac{\partial}{\partial y} \left(D_y \frac{h}{(b-a)} \frac{\partial c}{\partial y} \right) - (b-$$

$$a) \frac{\partial}{\partial z} \left(D_z \frac{\partial c}{\partial z} \right) - h\theta_s = 0$$

$$\rho - F(c) = 0 \quad (3-9)$$

where ρ_s is the density at the surface; ρ_z is the density at the elevation z ; u_s and v_s are horizontal Cartesian velocity components at the water surface; and u_b and v_b are horizontal Cartesian velocity components at the bed.

It is noted that the momentum and advection diffusion equations have been multiplied by h . D_x , D_y , and D_z represent similar approximations for the diffusion coefficients to those were made for the eddy coefficients. T_x , T_y , g_x , and g_y are defined by:

$$T_x = \frac{\partial a}{\partial x} + \frac{(z-a)}{(b-a)} \frac{\partial h}{\partial x} - \frac{h}{(b-a)} \frac{\partial a}{\partial x} + \frac{(z-a)}{(b-a)^2} h \frac{\partial a}{\partial x} \quad (3-10)$$

$$T_y = \frac{\partial a}{\partial y} + \frac{(z-a)}{(b-a)} \frac{\partial h}{\partial y} - \frac{h}{(b-a)} \frac{\partial a}{\partial y} + \frac{(z-a)}{(b-a)^2} h \frac{\partial a}{\partial y} \quad (3-11)$$

$$g_x = \int_z^{a+h} \frac{\partial}{\partial x} (\rho g) dz \quad (3-12)$$

$$g_y = \int_z^{a+h} \frac{\partial}{\partial y} (\rho g) dz \quad (3-13)$$

3.1.1.2 Boundary Conditions and Surface Traction

The free water surface is no leakage boundary conditions across the surface and zero pressure where the water depth is h .

$$w_s = \frac{dh}{dt} \quad (3-14)$$

The bottom is no leakage condition with drag from the bed for velocities:

$$u_b \frac{\partial a}{\partial x} + v_b \frac{\partial a}{\partial y} - w_b = 0 \quad (3-15)$$

where u_b , v_b and w_b are represent Cartesian velocity components at the bottom, and a is the elevation of the bottom relative to the same vertical datum. The side boundaries occur at system cuts where the boundary conditions specify water surface elevations for each (x, y) location, velocities at the (x, y, z) location, or flows at the cuts (uh and or vh).

The boundary is considered as being at a fixed location, thus it will require special numerical and analytical techniques for moving boundary systems. Hence, in the future paper we will propose the additional technique to simulate curve dynamic evolvement due to erosion and disposition process. Surface tractions for bed friction are using Chezy friction equation:

$$\Gamma_x = -\frac{\rho g u_b V}{C^2}, \quad \Gamma_y = -\frac{\rho g v_b V}{C^2} \quad (3-16)$$

where ρ is density, g is gravity acceleration, u_b and v_b are represent Cartesian velocity components at the bottom, $V = (u_b^2 + v_b^2)^{0.5}$ is magnitude of water velocity at the bed, and C is Chezy friction coefficient. Likewise, the wall friction is computed analogues to bed friction and directed in against the flow.

3.1.1.3 Eddy Viscosity and Diffusivity in The Vertical Direction

Vertical eddy viscosity and diffusivity may vary significantly over the depth in both homogeneous and stratified flow. RMA-10 has been developed to permit various forms of the dependence of these parameters. Parametric description for horizontal eddy viscosity and diffusivity ϵ_{xz} , ϵ_{yz} , and D_z are defined as quadratically varying over the depth.

$$\epsilon_{xz} = \epsilon_{xz'} \left[EDD1 + \frac{(z-a)}{(b-a)} \left(EDD2 + \frac{(z-a)}{(b-a)} EDD3 \right) \right] \quad (3-17)$$

where $\epsilon_{xz'}$, $EDD1$, $EDD2$, and $EDD3$ are fixed parameters defined in the model input. Similar way of scaling factors are used for ϵ_{yz} and D_z .

RMA-10 formulation for vertical eddy viscosity and diffusivity is based on diffusivity distributions developed for stratified reservoirs application. The ϵ_{xz} , ϵ_{yz} , and D_z are scaled from the homogeneous values developed using 2.63. D_f is the defined factor and applied to all three coefficients, and in English unit where $D_f = 1.0$;

$$\epsilon_{xz}'' = D_f \epsilon_{xz} \quad (3-18)$$

$$\text{when } \frac{1}{\rho} \frac{\partial \rho}{\partial z} < D_{cr} \text{ then } D_f = 0.6888 * 10^{-4} * \left(-\frac{1}{\rho} \frac{\partial \rho}{\partial z} \right)^{0.7} \quad (3-19)$$

$$\text{when } \frac{1}{\rho} \frac{\partial \rho}{\partial z} > D_{cr} \text{ then } D_{cr} = 1.1335 * 10^{-6} \text{ ft}^{-1} \quad (3-20)$$

$$\text{if } D_f < 0.01 \text{ then } D_f = 0.01 \quad (3-21)$$

$$\text{if } \frac{\partial \rho}{\partial z} > 0 \text{ then } D_f = 50.0 \quad (3-22)$$

The value from this method must be in the input data for homogeneous flow. Metric units can be used with the appropriate scaling.

Horizontal and vertical eddy diffusivity coefficients are used as turbulence mixing parameters in in hydrodynamics model (Ji, 2008). The horizontal eddy viscosity is related to turbulence in flow and affects velocity distribution. Smagorinsky formula can used to calculate horizontal eddy viscosity. In the model, RMA-10 uses Smagorinsky closure to control turbulence.

3.1.1.4 Solution of The Continuity Equation for Vertical Velocities

Volume continuity equation (1) is converted into a boundary value problem and differentiated with respect to z . It is subjected to boundary conditions for the water surface and the bed.

$$\frac{\partial^2 w}{\partial z^2} = -\frac{\partial}{\partial z} \left(\frac{\partial u}{\partial x} + \frac{\partial v}{\partial y} \right) \quad (3-23)$$

$$w = u^* \frac{d(h+a)}{dx} + v^* \frac{d(h+a)}{dy} + \frac{dh}{dt} \quad \text{at the water surface} \quad (3-24)$$

$$w = u^* \frac{da}{dx} + v^* \frac{da}{dy} \quad \text{at the bed} \quad (3-25)$$

In these equations the values of u and v will be known at all locations from the previous part of the solution step. Then values obtained for w in this solution are used in the next iteration for u, v, h and s .

3.1.2 EQUATIONS OF STATE

Equations of state are required to describe the relationships of the constituent concentration such as suspended sediment, temperature, and salinity to density in the RMA-10 equations. These equations are empirical.

$$\text{Suspended sediment: } \rho = 1.940 * (1.0 + 2.4 * 10^{-6} \text{ss}) \text{ where ss in } \text{mg/l} \quad (3-26)$$

$$\text{Temperature: } \rho = 1.93993 + T * (5.88599 * 10^{-5} - 1.108539 * 10^{-5} * T) \text{ where } T \text{ in degrees C} \quad (3-27)$$

$$\text{Salinity: } \rho = 1.940 * \left\{ 1.0 + \frac{(4.906*s-11.7)}{(6511.7-1.906*s)} \right\} \text{ where } s \text{ in parts per thousands} \quad (3-28)$$

It is noted that suspended sediment is treated as a conservative constituent. Settling, bed erosion, and deposition are not incorporated into RMA-10 module computation. In one simulation when multiple constituents are used, then density is defined as 1.940 added to the discrepancy from 1.940 for each constituent.

3.1.3 RMA-11 DESCRIPTION MODEL

3.1.3.1 Governing Equations for Three-Dimensional Transport

The RMA-11 governing equations are continuity equation (3-29) and advection diffusion equation (3-30). The advection diffusion equations in both conservative and non-conservative forms are presented in generalized form where source/sink and reactions variables are represented by generic terms. The same manner with RMA-10 governing equations that they are transformed to a constant water surface elevation b , and in the case where the principal diffusion direction is at angle to the x axis.

$$h \left(\frac{\partial u}{\partial x} + \frac{\partial v}{\partial y} \right) + (b - a) \frac{\partial w}{\partial z} - (b - a) \left(T_x \frac{\partial u}{\partial z} + T_y \frac{\partial v}{\partial z} \right) - h q_0 = 0 \quad (3-29)$$

$$h \frac{\partial c}{\partial t} + h \frac{\partial(uc)}{\partial x} + h \frac{\partial(vc)}{\partial y} + (b - a) \frac{\partial(wc)}{\partial z} - (b - a) T_x \frac{\partial(uc)}{\partial z} - \quad (3-30)$$

$$(b - a) T_y \frac{\partial(vc)}{\partial z} - (z - a) \frac{\partial h}{\partial t} \frac{\partial c}{\partial z} - h \frac{\partial}{\partial x} \left(D_x \frac{\partial c}{\partial x} + D_{xy} \frac{\partial c}{\partial y} \right) +$$

$$h \frac{\partial}{\partial x} \left(\frac{(b-a)}{h} \{ D_x T_x + D_{xy} T_y \} \frac{\partial c}{\partial z} \right) + (b - a) T_x \frac{\partial}{\partial z} \left(D_x \frac{\partial c}{\partial x} + D_{xy} \frac{\partial c}{\partial y} \right) -$$

$$(b - a) T_x \frac{\partial}{\partial z} \left(\frac{(b-a)}{h} \{ D_x T_x + D_{xy} T_y \} \frac{\partial c}{\partial z} \right) - h \frac{\partial}{\partial y} \left(D_{xy} \frac{\partial c}{\partial x} + D_y \frac{\partial c}{\partial y} \right) +$$

$$\begin{aligned}
& h \frac{\partial}{\partial y} \left(\frac{(b-a)}{h} \{D_{xy}T_x + D_yT_y\} \frac{\partial c}{\partial z} \right) + (b-a)T_y \frac{\partial}{\partial z} \left(D_{xy} \frac{\partial c}{\partial x} + D_y \frac{\partial c}{\partial y} \right) - \\
& (b-a)T_y \frac{\partial}{\partial z} \left(\frac{(b-a)}{h} \{D_{xy}T_x + D_yT_y\} \frac{\partial c}{\partial z} \right) - (b-a) \frac{\partial}{\partial z} \left(D_y \frac{(b-a)}{h} \frac{\partial c}{\partial z} \right) - \\
& Khc - h\theta_s - (b-a) \frac{\partial(V_S c)}{\partial z} = 0
\end{aligned}$$

If the continuity equation is substituted into advection diffusion equation then it becomes constituent transport equation:

$$\begin{aligned}
& h \frac{\partial c}{\partial t} + hu \frac{\partial c}{\partial x} + hv \frac{\partial c}{\partial y} + \left[(b-a)(w - uT_x - vT_y) - (z-a) \frac{\partial h}{\partial t} \right] \frac{\partial c}{\partial z} - \quad (3-31) \\
& h \frac{\partial}{\partial x} \left(D_x \frac{\partial c}{\partial x} + D_{xy} \frac{\partial c}{\partial y} \right) + h \frac{\partial}{\partial x} \left(\frac{(b-a)}{h} \{D_xT_x + D_{xy}T_y\} \frac{\partial c}{\partial z} \right) + \\
& (b-a)T_x \frac{\partial}{\partial z} \left(D_x \frac{\partial c}{\partial x} + D_{xy} \frac{\partial c}{\partial y} \right) - (b-a)T_x \frac{\partial}{\partial z} \left(\frac{(b-a)}{h} \{D_xT_x + \right. \\
& \left. D_{xy}T_y\} \frac{\partial c}{\partial z} \right) - h \frac{\partial}{\partial y} \left(D_{xy} \frac{\partial c}{\partial x} + D_y \frac{\partial c}{\partial y} \right) + h \frac{\partial}{\partial y} \left(\frac{(b-a)}{h} \{D_{xy}T_x + \right. \\
& \left. D_yT_y\} \frac{\partial c}{\partial z} \right) + (b-a)T_y \frac{\partial}{\partial z} \left(D_{xy} \frac{\partial c}{\partial x} + D_y \frac{\partial c}{\partial y} \right) - (b-a) \\
& T_y \frac{\partial}{\partial z} \left(\frac{(b-a)}{h} \{D_{xy}T_x + D_yT_y\} \frac{\partial c}{\partial z} \right) - (b-a) \frac{\partial}{\partial z} \left(D_y \frac{(b-a)}{h} \frac{\partial c}{\partial z} \right) - \\
& (q_0 - K)hc - h\theta_s - (b-a) \frac{\partial(V_S c)}{\partial z} = 0
\end{aligned}$$

where \mathbf{q}_0 is inflow per unit volume, V_S is the settling rate, and K is the first order rate coefficient.

3.1.3.2 Suspended Sediment (Cohesive)

Based on Ariathurai and Krone (1976) methodology in RMA-11 (King, 2013) is constructed to model transport of fine sediment or mud with several processes which are deposition through settling, erosion either as surface process or mass process, and development history of bed layer. Erosion and/or deposition are dependent on the bed shear stress developed by flowing water and the shear strength of surface layer on the bed. Strength of lower layer of the bed is increased through consolidation. This method is using variables of bed shear stress, settling rate, bed settling, and sediment erosion.

Bed Shear Stress τ_b

There are two options to compute bed shear stress based on law of the roughness wall with smooth bed assumption or rough one.

$$\tau_b = \rho_w u_*^2 \quad (3-32)$$

$$\text{for smooth bed: } u_m = u_* \log_e \left(\frac{3.32 u_* d}{v} \right) \quad (3-33)$$

$$\text{for rough bed: } u_* = \frac{V_K u_m}{\log_e \left(12.27 \frac{d}{r} \right)} \quad (3-34)$$

where ρ_w is water density (kg/m³), u_* is shear velocity (m/s), u_m is mean flow velocity (m/s), d is water depth (m), v is kinematic viscosity of water (m²/s), V_K is Von Karman's constant, and r is roughness height in meters.

Settling Rate V_S

Settling velocity is applied to model effective flocculation and its influence on particle settling rates and optionally defined as a function of the suspended sediment concentration.

$$V_S = V_1 \text{ for concentration } S < S_1 \quad (3-35)$$

$$V_S = V_{sk} S^{p_c} \text{ for concentration } S_1 < S < S_2 \quad (3-36)$$

$$V_S = V_{sk} S_2^{p_c} \text{ for concentration } S_2 < S \quad (3-37)$$

where V_1 , S_1 , S_2 , and p_c are all input parameters, and V_{sk} is derived as matching condition.

Bed Settling V_B

Deposition occurs when the shear stress on the bed is sufficient to re-suspend particles that contact and bond with the bed. The probability of settling occurrence increases as the shear stress decreases relative to the critical shear stress.

$$V_B = V_S \frac{(\tau_d - \tau_b)}{\tau_d} \text{ when } \tau_b < \tau_d \quad (3-38)$$

where V_B is effective bed settling velocity (m/s), V_S is particle settling velocity (m/s), τ_b is bed shear stress for settling (N/m²), and τ_d is critical shear stress for settling (N/m²).

Erosion Rate

Bed erosion will occur when it is above a critical level of shear stress. By Flowing water, resistance of a cohesive bed to erosion by flowing water relies on

certain factors; (1) clay minerals type that constitute the bed, (2) bed structure, which in turn depends on the environment in which the aggregates that formed the bed were deposited, the elapsed time, the temperature and the rate of gel formation, (3) pore chemical composition and eroding fluids, (4) stress history such as the maximum overburden pressure that the bed has experienced and the elapsed time at various stress levels, and (5) organic matter presence and its oxidation state.

It is called surface erosion when erosion occurs particle by particle at bed shear stresses just above the critical value. The bulk shear stress of the bed may be exceeded at higher levels of stress. A portion of the bed may be liable to exhibit mass erosion when the shear stress exceeded the critical shear stress. It is completely decline and instantly suspended. Therefore, the critical shear strength of bed stratum and erosion rate for surface erosion need to be defined. The erosion rate for surface erosion E_S may be written as:

$$E_S = M \frac{(\tau_b - \tau_{ce})}{\tau_{ce}} \text{ when } \tau_b > \tau_{ce} \quad (3-39)$$

where M is erodibility constant, and τ_{ce} is critical shear stress for erosion (N/m^2).

The erosion rate for mass erosion can be defined assuming that all mass is eroded over a time step, and may be written as:

$$E_M = \frac{\Delta m}{\Delta t} \text{ when } \tau_b > \tau_{cl} \quad (3-40)$$

where Δm is mass eroded per unit bed area (gm/m^2), Δt is time step (s), and τ_{cl} is critical shear stress for layer mass erosion (N/m^2).

3.1.3.3 Sand/Silt (Non-Cohesive Sediment)

It is noted that RMA-11 referred components of sediment mixture of both sand and silt as sand only. RMA-11 can model sand transport in up to 5 separate sizes. There are two methods used (1) sand potential or (2) erosion-deposition for each constituent. We can select either approach for an individual constituent so that a simulation can consist of some sizes that use the sand potential method and some that use the erosion-deposition method by switching the input of a non-zero critical shear stress for deposition on SAND4 data lines. If it is not defined then the sand potential method is used for all sand classes.

3.1.3.3.1 Sand Potential Method

Concept of sand transport potential can be thought of as the concentration at which the sand is at equilibrium in the suspension. This method uses erosion and deposition with intention to move towards this equilibrium, and is assumed to depend on the sand and flow parameters. It is designated for sand constituents with a diameter greater than 0.100 mm. The bed source/sink term is defined in general by:

$$S = \frac{c_{eq} - c}{t_c} \quad (3-41)$$

where S is the source/sink term (gm/s/m²/meter of depth), c_{eq} is equilibrium concentration (transport potential in mg/l), c is sand concentration in the water (mg/l), and t_c is characteristic time for effecting the transition, this is depends on whether deposition or erosion is occurring (s).

This model is based on STUDH method by Corps of Engineers 1985 (King, 2013). Five options as cited from (King, 2013) are allowed for computation of the transport potential: (1) Ackers-White equations (1973), (2) Van Rijn method (1984), (3) Brownlie method (1981), (4) Van Rijn method (1989) that allows for wave transport effects, and (5) method that expands the method *sed* for wave transport effects (van Rijn, 1993). Here, we used Ackers-White equations in English units:

$$D_{gr} = D_{50} g^{1/3} (S_{gs} - 1.0)^{1/3} v^{*-2/3} \quad (3-42)$$

where D_{gr} is grain number, D_{50} is 50th percentile grain diameter (mm), g is acceleration due to gravity in English units for Ackers-White formulation, (ft/s²), S_{gs} is specific gravity of sand, and v^* is kinematic viscosity of water in English units for Ackers-White formulation (ft/s²).

For $D_{gr} > 60$ then four coefficients are defined as $n = 0$, $A = 0.17$, $m = 1.5$, and $c = 0.025$. For $60 > D_{gr} > 1$ then four coefficients are defined as followed:

$$n = 1.0 - 0.56 \log D_{gr} \quad (3-43)$$

$$A = \frac{0.23}{D_{gr}^{1/2}} + 0.14 \quad (3-44)$$

$$m = \frac{9.66}{D_{gr}} + 1.34 \quad (3-45)$$

$$\log c = 2.86 \log D_{gr} - (\log D_{gr})^2 - 3.53 \quad (3-46)$$

$$u^{*'} = \frac{v^*}{32^{1/2} \log \frac{10d^*}{D_{50}}} \quad (3-47)$$

where v^* is water velocity in English units for Ackers-White formulation (ft/s), and d^* is depth in English units for Ackers-White formulation (ft).

The mobility number F_{gr} is defined by:

$$F_{gr} = \frac{u^{*n} u^{*(1-n)}}{(gD_{50}(S_{gs}-1.0))^{0.5}} \quad (3-48)$$

where u^* is bed shear velocity in English units for Ackers-White formulation (ft/s). Then the equilibrium concentration (transport potential) c_{eq} is given by:

$$c_{eq} = cS_{gs} \left(\frac{v}{u^*} \right)^n \left(\frac{F_{gr}}{A} 1.0 \right)^m \quad (3-49)$$

In the current version of the model the bed shear velocity u^* is computed using a Manning shear stress equation. Thus u^* in metric units is given by:

$$u^* = \frac{M_n g^{0.5} v}{d^{1/6}} \quad (3-50)$$

where M_n is Manning coefficient, and v is water velocity near bed (m/s).

Sand Deposition Method

Deposition occurs when the equilibrium sand concentration is less than the sand concentration in the water. Characteristic time t_c is a function of fall velocity, and there are two options here to compute it. Option 0 is based on STUDH, it treats the time step as a limiting value.

$$t_c = \text{larger of } C_d \frac{d}{V_s} \text{ or } \Delta t \quad (3-51)$$

where C_d is coefficient for deposition with typical value 1.0, V_s is fall or settling velocity (m/s), and Δt is computation time step (s).

The other, option 1 is an alternate formulation where it uses an input characteristic time as a limiting value. Therefore it is independent of Δt .

$$t_c = \text{larger of } \frac{d}{V_s} \text{ or } 3600 * C_{td} \quad (3-52)$$

where C_{td} is an input characteristic time for deposition with typical value 0.05.

Sand Erosion Method

Erosion occurs when the equilibrium sand concentration is less than the sand concentration in the water. Characteristic time is a more complex function and employing empirical form, and also there are two options using. Option 0 is based on STUDH, it treats the time step as a limiting value.

$$t_c = \text{larger of } C_e \frac{d}{V} \text{ or } \Delta t \quad (3-53)$$

where C_e is coefficient for erosion with typical value 10.0, V is water velocity near bed (m/s), and Δt is computation time step (s).

The other, option 1 is an alternate formulation where it uses an input characteristic time as a limiting value. Therefore it is independent of Δt .

$$t_c = \text{larger of } \frac{d}{V} \text{ or } 3600 * C_{te} \quad (3-54)$$

where C_{te} is an input characteristic time for erosion with typical value 0.05.

3.1.3.3.2 *Erosion-Deposition (Non-Cohesive Sediment)*

Similar to those used for cohesive sediment, source/sink terms are computed from calculated erosion-deposition rates.

Deposition

The method assumes that deposition of the bed occurs when the shear stress on the bed is not sufficient to re-suspend particles. The probability of settling occurrence increases as the shear stress decreases relative to the critical shear stress.

$$V_B = V_S \frac{(\tau_d - \tau_b)}{\tau_d} \text{ when } \tau_b < \tau_d \quad (3-55)$$

where V_B is effective bed settling velocity (m/s), V_S is particle settling velocity (m/s), τ_b is bed shear stress for settling (N/m^2), and τ_d is critical shear stress for settling (N/m^2).

Erosion

The method assumes that erosion of the bed occurs above a critical level of shear stress erosion. For each given sand size classes the erosion rates is expressed as:

$$E_s = M e^{\alpha[\tau_b - \tau_{ce}]} \text{ when } \tau_b > \tau_{ce} \quad (3-56)$$

where E_s is erosion rate (kg/m²/s), τ_{ce} is critical shear stress for erosion, (N/m²), M is erodibility constant and equal to erosion rate at point of initial erosion (kg/m²/s), and α is a power factor.

3.1.3.3.3 Bed Structure

The bed is assumed to be given an initial thickness, and that deposition builds a bed with a porosity of 0.4. Thus for each sand size, the increase of thickness from deposition ($\delta + 've$) or loss through erosion ($\delta - 've$) is applied by:

$$\Delta b = \frac{\delta \Delta t}{0.4 \rho_s} \quad (3-57)$$

where Δb is additional thickness of sand (m), δ is source rate of sand of this size (kg/s/m²), and ρ_s is effective density of sand (kg/m³).

3.1.3.3.4 Armoring

For multiple sand sizes, armoring can be modeled by defining a parameter that provides for limiting erosion of any individual sand size. The bed is in undergoing erosion and limited so that the mass of the remaining fractions after the projected erosion cannot be less than a factor multiplied by the total mass in the bed for all sand sizes of greater diameter. Consequently, the factor equals to 0.0 means erosion will unconstrained by armoring. Furthermore, if the bed is reduced to less than zero using the computed erosion rates then the total bed thickness serves to reduce the source rate. This limit applies when the armoring factor is 0.0.

3.2 MODEL SET UP

The value of parameter in model set up can be selected from a feasible range, evaluated in the model, adjusted to the model results based on literature review and/or pervious modeling studies and experimental data (Ji, 2008).

RMA model consists of simulation sequence and graphic modules. The pre-processor is RMAGEN which is a graphic module to generate mesh of finite element networks. The processor for three-dimensional finite element model for stratified hydrodynamic simulation is RMA-10, and for three-dimensional water quality model including sediment transport is RMA-11. The post-processor is RMAPLT for displaying results as current vectors, contour plots, time histories or section plots.

The processor modules of RMA-10 and RMA-11 are based on the finite element method and geometrically designed to execute input setting from two-dimensional horizontal network and data describing the number of elements vertically from all corner nodes.

The processor file structures can be seen as series of blocks as seen in the figure 5. The input files of RMA-10 and RMA-11 are similar. There is only one addition R4Q file need to describe the water quality parameters containing their relationships and kinetics.

Table 3-1. Construction of input files (modified from King 1993)

BLOCK DATA	R10 FILE	R11 FILE	R4Q FILE
1	FILE DATA Information on files that will be required for input or output.	FILE DATA Information on files that will be required for input or output.	SYSTEM CONTROL DATA Information on constituents that are to be used overall prototype location.
2	LIMIT DATA Information that overrides defined limits for model use	CONTROL DATA Control data defining this run	GLOBAL WATER QUALITY DATA Water quality parameters that are common to the whole system
3	CONTROL DATA Control data defining this run	SYSTEM PROPERTY DATA Water, bed and system properties	ELEMENT TYPE DEPENDENT WATER QUALITY DATA Water quality parameters that vary by element type number
4	SYSTEM PROPERTY DATA Water, bed and system properties	INITIAL CONDITION DATA Initial condition and rate terms for all nodes	METEOROLOGIC DATA Weather data
5	STEADY STATE STEP DATA Time step and boundary condition data	TRANSIENT STEP DATA Time step and boundary condition data	

3.2.1 MEANDER GEOMETRY

For plan shape of a meandering river, we used sine-generated curve (Leopold and Langbein 1966) as depicted by the following equation where l_c is longitudinal coordinate along the meandering flow centerline L :

$$\theta = \theta_0 \cos\left(2\pi \frac{l_c}{L}\right) \quad (3-58)$$

The best given proportionality of meander wavelength Λ_M and channel width B is around 6. The plan shapes of sine-generated curve are differed by values of the deflection angle θ_0 . The deepest erosions and highest depositions must be expected to occur around the crossovers O_i if θ_0 is “small”, and around the apex-sections a_i if θ_0 is “large”. Small angle is 30° , large angle is 110° , and medium angle is 70° (da Silva 2006). Factors that affect the development of helical flow in this model are geometry characteristics and turbulence flow properties. The idea is to make the flow high turbulent in order to evoke helical flow. Therefore we set up high value of Smagorinsky closure for the flow and high Chezy friction number for the bed and wall.

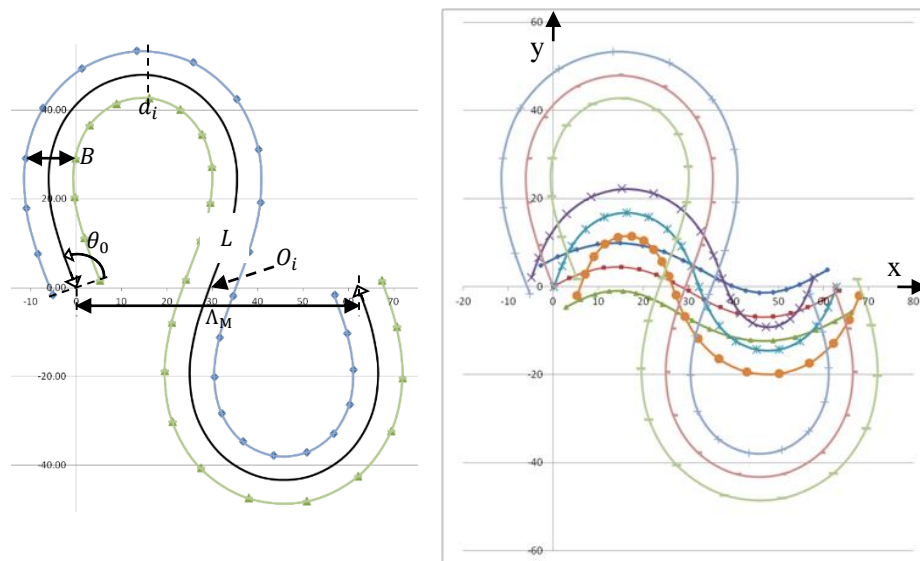


Figure 3-1. Definition sketch of a meander geometry and bed depth contour.
Unit in x and y directions are in meters

3.2.2 MESH GENERATING AND BED DEFORMATION

Mesh is generated by a pre-processor module RMAGEN. Basically each element is a quadrilateral element with 8 nodes which are consisted of 4 corner nodes at the vertices of the element and 4 mid-side nodes in the middle of the element. Each cross-section channel is divided into 8 elements by width. For flat bed, it used bed depth 5.5 m or bed at elevation -5.5 m.

Table 3-2. Variables of meander geometry.

Deflection angle of a meandering flow	θ_0	L [m]	Λ_M [m]	B [m]	Node Numbers	Element Numbers	Layer Numbers
Small	30°	68	66	11	6185	2208	4
Medium	70°	95	66	11	6905	2464	4
Large	110°	232	66	11	8345	2976	4

In meandering river, the bed is deformed at the bend where the inner bend has a higher level than the outer. The bed deformation gives significant effect in the development of helical flow since it governs the interaction between the turbulent flow motion and the suspended sediment constituting the river bed (Struiksma, et al., 1985).

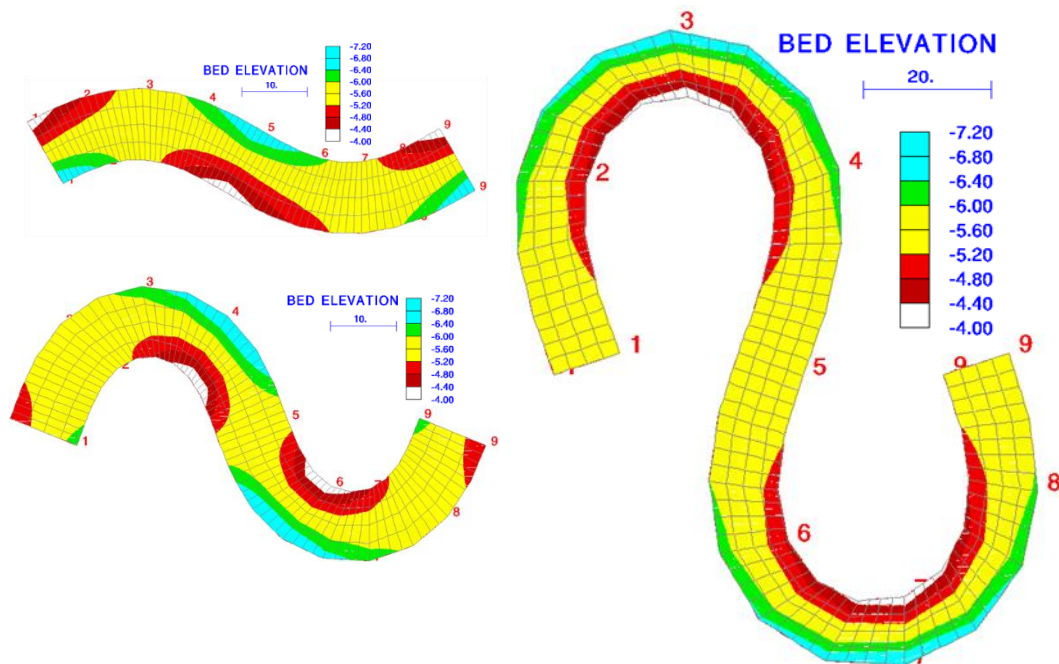


Figure 3-2. Meshing elements, bed depth contours and continuity lines for deviation angles: (a) 30°, (b) 70°, and (c) 110°

Cross-lines coordinates at the center line meander are shown in Table 3-3. It is noted that for the line 1, 19 is node number and (3;-5;-7) is Cartesian coordinates.

Table 3-3. Continuity lines coordinates at meander center lines

Line	Deflection Angles θ								
	30°			70°			110°		
1	19 (3;-5;-7)	37 (0;0;-5.5)	1 (-3;5;-4)	21 (5;-2;-6.2)	41 (3;16;-5.5)	1 (-5;2;-4.8)	25 (5;2;-5.5)	49 (-5;-2;-5.5)	1 (-5;-2;-5.5)
3	23 (15;-1;-5.5)	51 (15;4;-5.5)	5 (15;10;-5.5)	26 (17;11;-4.8)	59 (16;17;-5.5)	6 (15;22;-6.2)	31 (16;43;-4)	71 (15;48;-5.5)	7 (13;53;-7)
5	264 (28;-6;-4.1)	147 (31;-1;-5.5)	149 (34;3;-6.9)	31 (27;-2;-5.5)	79 (32;0;-5.5)	11 (38;2;-5.5)	37 (24;2;-5.5)	95 (29;0;-5.5)	13 (35;-2;-5.5)
7	305 (48;-12;-5.4)	304 (48;-7;-5.5)	307 (48;-1;-5.6)	36 (50;-20;-6.2)	99 (50;-14;-5.5)	16 (50;-9;-5.9;-4.8)	43 (51;-48;-7)	119 (51;-43;-5.5)	19 (51;-37;-4)
9	36 (66;-6;-7)	103 (64;-1;-5.5)	18 (61;4;-4)	40 (68;-2;-4.8)	115 (63;0;-5.5)	20 (58;2;-6.2)	48 (67;2;-5.5)	139 (62;0;-5.5)	24 (57;-2;-5.5)

Mesh independence test is procedure to make sure that the solution is independent of the mesh resolution. At initial, grid is drawn as in Figure 3-2 but the they get refined fourth times until the solutions are independent from the grid resolution.

Setting up meander geometry is complied with shallow water approximation in sub-sub-chapter 3.1.1, where all geometry simulations have ratio of; 0.081, 0.058, and 0.024. All the ratios are much less than 1 and within shallow water approximation.

3.2.3 SIMULATION THREE-DIMENSIONAL FLOW

For the truly three-dimensional computation, RMA-10 uses the solid elements for the volume integrals and the surface elements for the boundary

integrals. Types of surface elements used here are: (1) water surface elements for evaluation of surface velocity terms in the continuity equation; (2) bed elements for evaluation of bed friction and pressure terms in the momentum equations and bed velocity terms in the continuity equation; (3) side elements for external sides of system and applying pressure or water depth and or slip boundary conditions in the momentum equations.

The main inputs in RMA-10 are meander geometry, running control, system properties, initial condition, and transient step data. The meander geometries comprise flat and deformed beds for each deviation angle small, medium and large.

In control data block we set up turbulence closure method using original Smagorinsky to control horizontal eddy with alfa factor 0.5 and minimum kinematic eddy viscosity $1.0 \text{ m}^2/\text{s}$, using bottom friction Manning resistance to control bottom velocities, treating concentration variable as passive conservative constituent, local attitude average is 0.00 to set equator location, initial value for temperature is 20°C and for suspended sediment concentration is 10.0 mg/l , initial iteration value for u and v bed velocity is 0.1 m/s , initial water surface elevation is -2.0 m , and suspended sediment settling rate is 0.01 m/s .

During convergence test, the maximum allowable change in x -velocity and y -velocity is 0.02 m/s , in temperature is 0.010°c , and in sediment is 0.010 mg/l .

As for element properties data, turbulent exchange coefficients associated with x -direction shear of x -direction flow, with y -direction shear of x -direction flow, and with x -direction shear of y -direction flow is all 0.1 pascal-sec , whether with y -direction shear of y -direction flow is 1 pascal-sec . Manning coefficient for all element is 0.040 , and turbulent exchange coefficients associated with z -direction shear of x -direction flow and with z -direction shear of y -direction flow is all 0.1 pascal-sec . Turbulent diffusion coefficient associated with the x -direction is $0.05 \text{ m}^2/\text{s}$, and Turbulent diffusion coefficient associated with the y -direction and with the z -direction is all $0.1 \text{ m}^2/\text{s}$. Manning coefficient for shoreline is 0.020 , and for water surface is 0.015 .

Vertical distribution coefficient at externally specified flow boundaries is 0.4, and at interface between two- and three-dimensions is 0.4. Here, we used 4 layers data at elevation -2.5 m, -3.0 m, -3.5 m, and -5.0 m.

For time variable simulation, firstly we simulated for steady state where time step is 0. For transient state, time step is different for each geometry. The smaller the deviation angle is the smaller the time step. As for small deviation angle 30° is 0.001 s, for 70° is 0.01 s, and for 110° is 0.05 s.

In each geometry, it has 9 continuity lines where we set it up as boundary condition to determine the total flow and constituent inflow crossing the line. Otherwise, we used hydrograph inflow as dynamic simulation.

RMA-10 in fact can simulate a suspended sediment simulation along with the three-dimensional flow computation by using BQD option. However, after several running test, the results are not satisfied then we focus on RMA-11 simulation.


```

case13A.r10 - Notepad
File Edit Format View Help
output file name
OUTFIL case13A.out
input binary name
INBNGEO case13.geo
output file name for creation of saving results from this run
OUTBNRMAC case13A.rma
output 3-d geometry file name
OUTBN3GEO case13.3dg
INHYD CASE13.HYD
OUTBNRSTCASE13A.RST
ENDFIL

title data
water flow 3D
TI
C0 IOPTZD IDNOPT IYRR DAYOFY TET IEDSW TBFAC TBMIN IPROJ
0 0 2012 1 0.00 2 0.5 1.0 0
NDP IGRV IZB IPASS1 IPASS2 IPASS3 IZERS
C1 2 1 0 1 1 1 0
OMEGA ELEV XSCALE YSCALE ZSCALE
C2 0.00 -2. 1 1
CMIN CPR UNOM
C3 1.00 1.0 0.00
SALI TEMPI SEDI UINP VINP PRCNT
C4 0.0 20.0 10.0 0.1 0.1 0
NITI NITN TSTART NCYC IPRT NPRTI NPRTF IRSAV IDSWT
C5 10 10 0 120 1 0 8 1 0
IOUTFREQ IOUTRST IREWOUT IDLND ICPU IOOC IREWMES
C6 1 10 0 0 4 0 0
ELEV1
INIT
-2.
VSET VDECAV PRECIP
VSET
0.01
CONV(1) CONV(2) CONV(3) CONV(4) CONV(5) CONV(6) IDRPT
CV 0.020 0.020 0.010 0.010 0.010 0.010 0
JORT(J,1)ORT(J,2)ORT(J,3)ORT(J,4)ORT(J,5)ORT(J,6)ORT(J,7)
ED1 1 0.1 0.1 0.1 1 0.040 1.0 1.0
ORT(J,8)ORT(J,9)ORT(J,10)ORT(J,11)ORT(J,12)ORT(J,13)
ED2 0.05 0.1 0.1 0.020 0 0.015
VD VMIN POWER UMIN PWERIN
0.4 0.5 0.4 0.5
I NDEP(I)
LD3 0 4 -2.5 -3.0 -3.5 -5.0
ENDGEO

DELTA
DT 0.00
BQD
QC 9 0 1. 3.7 0.0 20.0 1.0 1
HC 1 0 0. 0.0 20.0 1.0 0
ENDSTEP

DELTA IYRE IDYE IHRE NPRTF
DT 0.001 2012 40 24.0
BQD
HC 1 0 0. 0.0 20.0 1.0 0
ENDSTEP
ENDDATA
Ln 21, Col 3

```

```

case13.HYD - Notepad
File Edit Format View Help
SKELETON HYDROGRAPH
TH 9 2012
CLQ
QD 1 0. 0 2. 00. 20. 1.
QD 1 .01 0 10. 00. 20. 1.
QD 1 .02 0 40. 00. 20. 1.
QD 1 .03 0 80. 00. 20. 1.
QD 1 .04 0 160. 00. 20. 1.
QD 1 .05 0 320. 00. 20. 1.
QD 1 .06 0 400. 00. 20. 1.
QD 1 .07 0 240. 00. 20. 1.
QD 1 .08 0 120. 00. 20. 1.
QD 1 .09 0 40. 00. 20. 1.
QD 1 .10 0 20. 00. 20. 1.
QD 1 .20 0 2. 00. 20. 1.
ENDDATA
Ln 18, Col 1

```

Figure 3-3. RMA-10 input setting for meander with deviation angle 30°, and hydrograph inflow

Typical input setting is as shown in Figure 1-1. During the dynamic simulation, we used hydrograph values for the inflow with HYD file which is activated by LABL option with 1. The crucial parameters that has to be carefully input are TBFAC or alfa factor applied in Smagorinsky closure, TBMIN or minimum kinematic eddy viscosity using the Smagorinsky closure in m²/s, INIT ELEV or initial water surface elevation, LD3 or layer data for specified elevations, and DT or time step control.

Smagorinsky model is chosen because it facilitates possible large-scale turbulence anisotropy (van Balen et. al 2010). Initial water surface elevation is

maintained to be valid for shallow water approximation when ratio of depth (h) to channel length (L) is less or equal to 0.05 (Ji 2008). Time step control is kept below the flood wave travel time in order to stabilize the numerical calculation (Bates et. al 2005, King 2012).

$$\text{Shallow water approximation: } \frac{h}{L} \leq 0.05 \quad (3-59)$$

$$\text{Wave travel time: } \frac{L}{\sqrt{g*h}} \quad (3-60)$$

As stated by Ji (2008), based on sensitivity tests with a six-layer model, three-layer model is actually adequate to represent the vertical structure of the object study of surface water in most of the time.

3.2.4 SIMULATION THREE-DIMENSIONAL SEDIMENT TRANSPORT

RMA-11 is using input of velocities and depths from RMA-10 output. RMA-11 used R4Q file to define input sediment parameters. The crucial parameters that has to be carefully input are defining diffusion DF in the properties block, setting up boundary conditions BC at the upstream, applying element loading DL whether at this time it is only for an element for three-dimensional simulation, setting conservative constituent to avoid bumpy results with ICNSV is 1, managing time step control DT lower than the wave travel to evade from low flow case, and specifying sediment parameters in R4Q file.

The diffusion coefficient (diffusivity) is often assumed to proportional to the eddy viscosity of turbulent flow. The parameters used in the model are horizontal and vertical eddy diffusivity coefficients. The horizontal eddy viscosity affects velocity distribution and can be calculated using the Smagorinsky scheme. The vertical eddy viscosity treats vertical mixing in the model and is represented in the closure model (Wu, 2008).

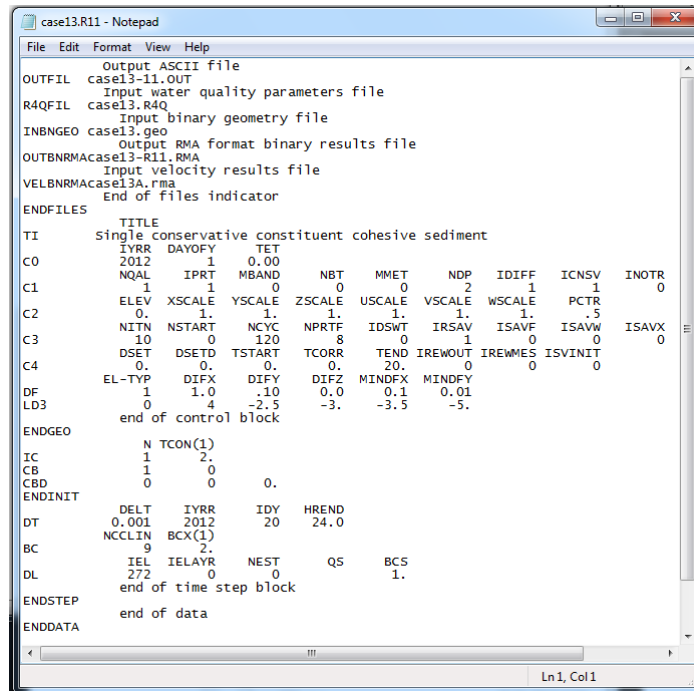


Figure 3-4. RMA-11 input setting for meander with deviation angle 30°

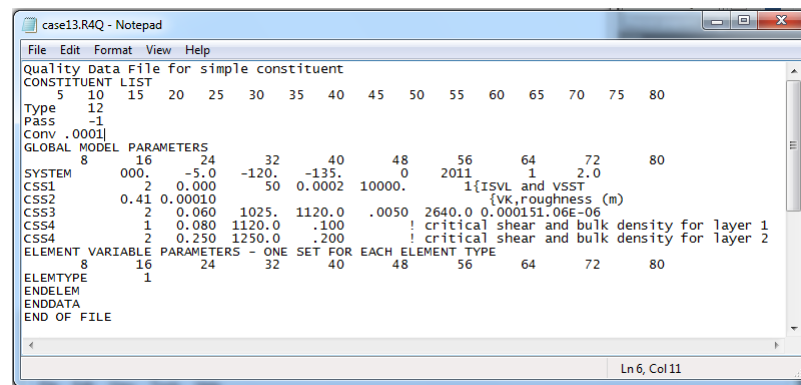
The zone of influence of boundary conditions propagates through the domain at each time step, and carries information from the upstream boundary condition. This is important in advection-dispersion problems where conservation of mass is considered certain (Julien, 2002). Sediment can be assumed as a conservative constituent that do not react under chemical and biological decay where the rate of reaction is very low. The vertical velocity for cohesive sediment can be related to sediment concentration other factor such as flow shear. The settling velocity for non-cohesive sediment is a function of the grain size, density, and shape, and is not customarily associated with sediment concentration (Ji, 2008).

Sediment is moved as suspended load and/or bed load. Cohesive sediments are only transported as suspended sediment whereas non-cohesive sediments can be both. Suspended load is transported in suspension in the water column including sediment resuspended from the bed and the wash load brought from upstream. Bed load is moved on or near the bed saltation, rolling, or sliding in the bed layer and occurs periodically in a thin layer of several grain diameters in thickness (Ji, 2008). It depends on their particles sizes to move in as suspended

load or bed load, but it is commonly assumed suspension as the main transport mode (Wu, 2008).

3.2.4.1 Cohesive Sediment

Regularly cohesive sediments are present in the form of mud in water-bodies, in most cases, mud include clay and non-clay minerals in the clay - and silt - size ranges, organic matter, and, sometimes, small quantities of fine sand. Practically the non-cohesive sediment movement can be estimated by knowing its physical properties such as the grain size and shape, specific gravities of the sediment and water, and the viscosity or temperature of the water (Ji, 2008).



```

case13.R4Q - Notepad
File Edit Format View Help
Quality Data File for simple constituent
CONSTITUENT LIST
5 10 15 20 25 30 35 40 45 50 55 60 65 70 75 80
Type 12
PASS -1
Conv .0001
GLOBAL MODEL PARAMETERS
8 16 24 32 40 48 56 64 72 80
SYSTEM 000. -5.0 -120. -135. 0 2011 1 2.0
CSS1 2 0.000 50 0.0002 10000. 1{ISVL and VSST
CSS2 0.41 0.00010 {vk,roughness (m)
CSS3 2 0.060 1025. 1120.0 .0050 2640.0 0.000151.06E-06
CSS4 1 0.080 1120.0 .100 ! critical shear and bulk density for layer 1
CSS4 2 0.250 1250.0 .200 ! critical shear and bulk density for layer 2
ELEMENT VARIABLE PARAMETERS - ONE SET FOR EACH ELEMENT TYPE
8 16 24 32 40 48 56 64 72 80
ELEMTYPE
ENDELEM
ENDDATA
END OF FILE
Ln 6, Col 11

```

Figure 3-5. Cohesive sediment parameters in R4Q file

Parameters of cohesive sediment used here are in line CSS1; settling velocity 0,0002 m/s, and settling velocity parameter 10000 gm/m³. In line CSS2 there are von Karman constant 0.41, and bed height roughness for Rouse distribution calculation 0.00010 m. In line CSS3 there are 2 number of layers of new deposits formed, critical shear stress for deposition of new layer 0.060 N/m², density of suspending water 1025.0 kg/m³, bulk density of top layer 1120.0 kg/m³, full thickness of top layer 0.0050 m, density of sediment material 2640.0 kg/m³, erosion rate constant for bottom layer 0.000151 kg/(m²s), and kinematic viscosity of suspending water 0.06e-6 m/s at 20°C.

In lines CSS4 there are set two layers, for each layer 1 and 2 consecutively the critical shear stress in N/m², bulk density in kg/m³ and layer thickness in m are: 0.080 and 0.250; 1120.0 and 1250.0; and 0.100 and 0.200.

3.2.4.2 Non Cohesive Sediment

Non-cohesive sediments on average include gravel, sand, and some silt. There are three important properties of non-cohesive sediments consist of (1) particle size, (2) shape, and (3) specific gravity (Ji, 2008).

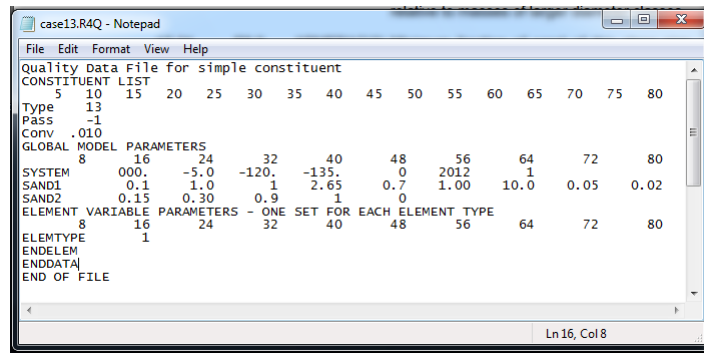


Figure 3-6. Non-cohesive sediment parameters in R4Q file

Parameters of non-cohesive sediment used here are in line SAND1 there are minimum grain size 0.1 mm, maximum grain size 1.0 mm, specific gravity of sediment 2.65, grain shape factor 0.7, characteristics length factor/time for deposition 1.00, characteristics length factor/time for deposition 10.0, fall velocity for sediment 0.05 m/s, and Manning coefficient used to calculated bed shear velocity for Ackers-White formulation 0.02.

In line SAND2 there are D35 grain size 0.15 mm, D50 grain size 0.30 mm, D90 grain size 0.90 mm, transport method option to use Ackers and White is 1, and treatment of characteristics length factor/time for erosion-deposition option to use standard STU DH method is 0.

3.3 RESULTS AND DISCUSSION

Results of RMA-10 and RMA-11 are presented in ASSCII output files, and read by post-processor of RMAGEN. The simulations run on flat and deformed bed, with high and low flow, and for non-cohesive (sand).

The discussion object is divided in to three parts; flow structures, bed depth profiles, and sediment distributions.

For the turbulence structures through planform geometry, the cross-circulation flow combined with longitudinal flow motion defines helical flow. The presence of helical flow as shown in Table 3-4 diverts the distribution of fluid velocity, and transfers the high momentum fluid from the inner-side to the outer-side of the river bend to shift the core of maximum velocity towards the outer-bank and the flow is accelerated. Towards the inner-bank, the flow is decelerated.

In Figure 3-7, from the velocity vector fields the velocity is decreasing at the bends and sidewalls. This is agreed with (da Silva, 2006), (Tilston, et al., 2009), (Termini & Piraino, 2011) that the cause of decreasing velocity is the occurrence of helical flows. We can see from Figure 3-7 that the flow velocity gained the highest value at the outer bend for each deflection angle. The fluid flows from left to right, from this perspective the outer-bank is at the upper side of the curved-channels.

The deflection angle of sine-generated curve where flow enters the bend alters the shifting of velocity zones. The bigger the deflection moves the location of maximum velocity more downward of stream flow, this can be seen in Figure 3-7. According to (Julien, 2002) where he mentioned that the strength of secondary circulation is affected by the flow deviation angle of the streamlines. The deflection angle defines the deviation angle, where at large deviation angles shift the maximum velocity zones and determine the direction of channel migration. This is also agreed with (Odgaard, 1989).

Through the water column, the high momentum fluid transfers from the upper-part of the flow towards the lower-part and it is called sweep. The opposite occurs along the tailing half of the rotation eddy, and it is known as burst. Sweep is oriented towards the outer-bank at acceleration zones, and burst is oriented towards the inner-bank at deceleration zones.

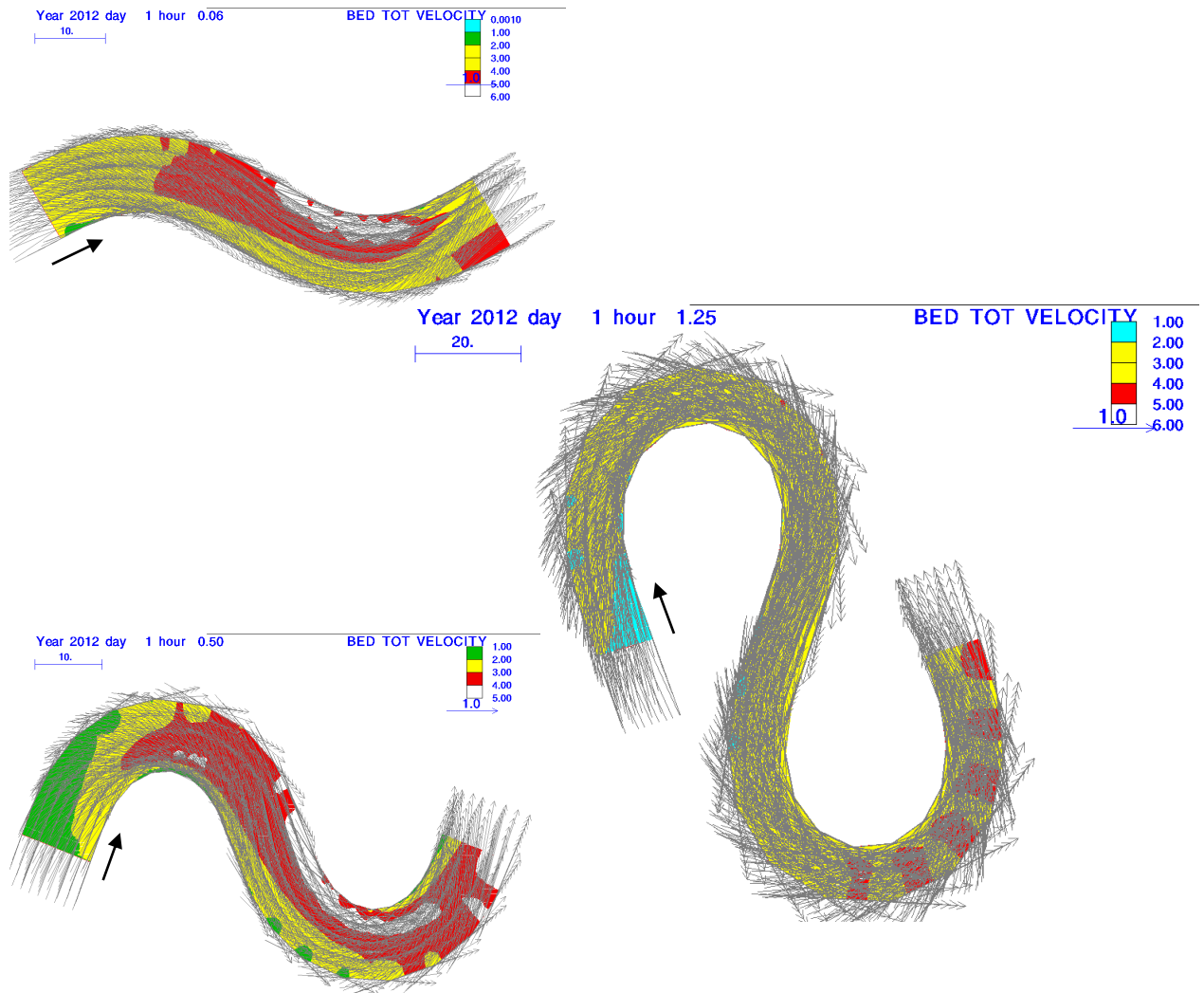
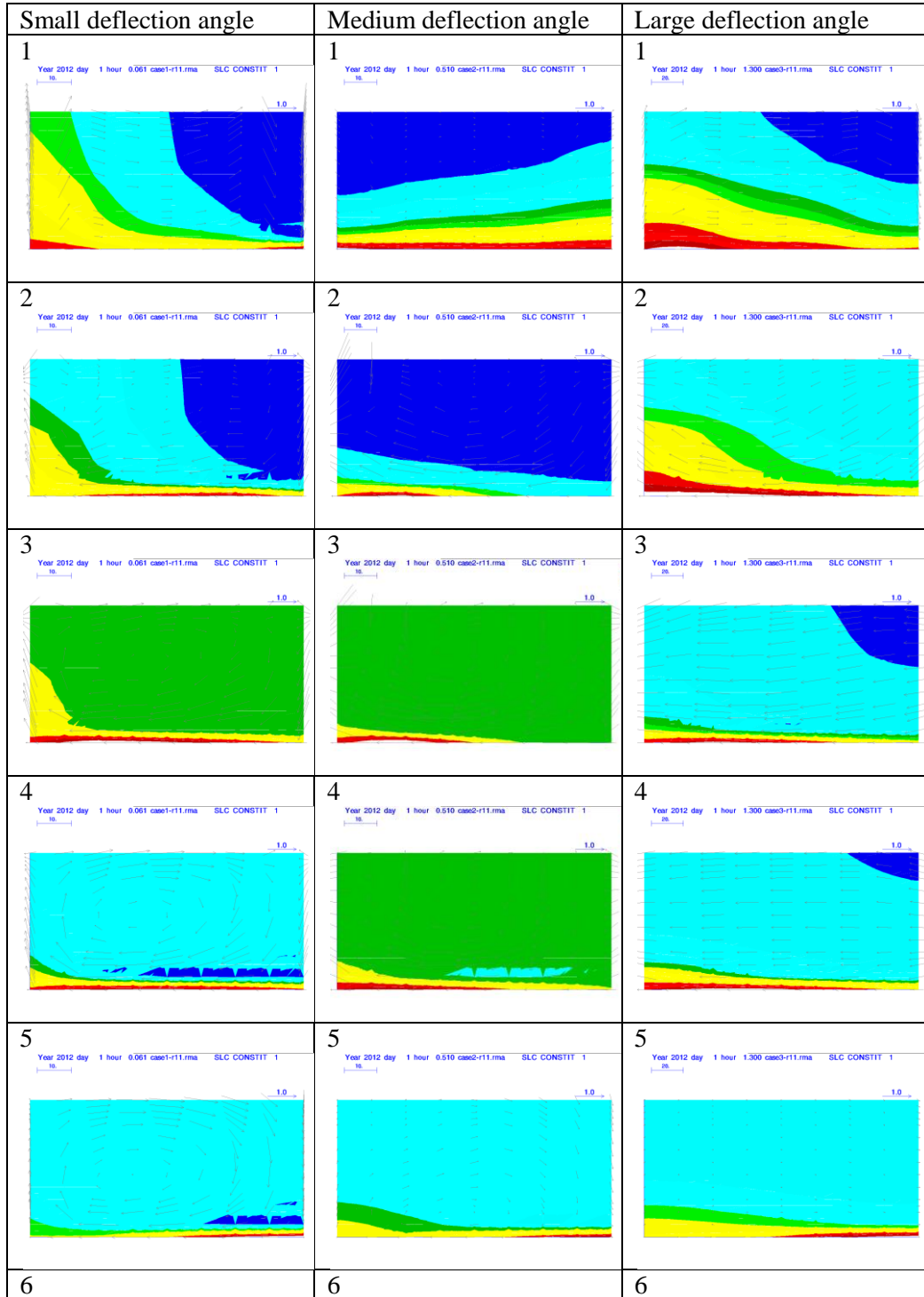


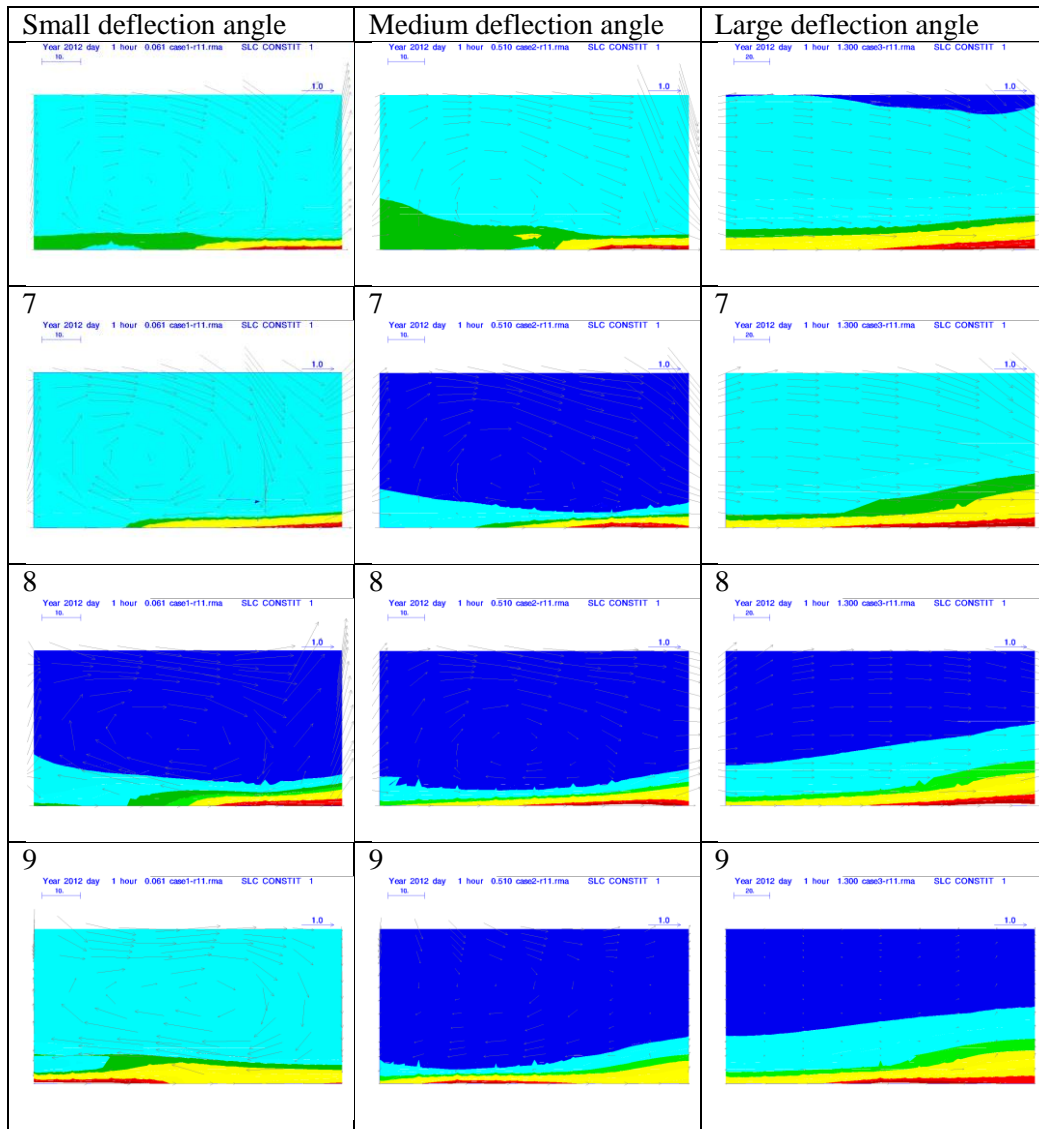
Figure 3-7. Flow structures

Shown in Table 3-4 this is agreed with (Wu, 2008) and (Termini & Piraino, 2011) where the major secondary current observed in the cross-section of a channel bend is the helical flow, and points to the outer bank in the upper layer and to the inner bank in the lower layer. For small deflection angle, the helical flow is developed clearly in cross-section 3 and consistent to spin clockwise direction up to cross-section 7. For medium deflection angle, the helical flow spun clockwise direction is also developed clearly in cross-section 3, but getting weaker in cross-section 5, and then developed stronger up to cross-section 8. For large deflection angle, the helical flow development is not as strong as for others, from cross-section 1 to 4, it spins clockwise direction but in cross-section 5 it is

disappeared and then developed in counter-clockwise direction from cross-section 6 to 9.

Table 3-4. Cross sections from upstream (1) to downstream (9).



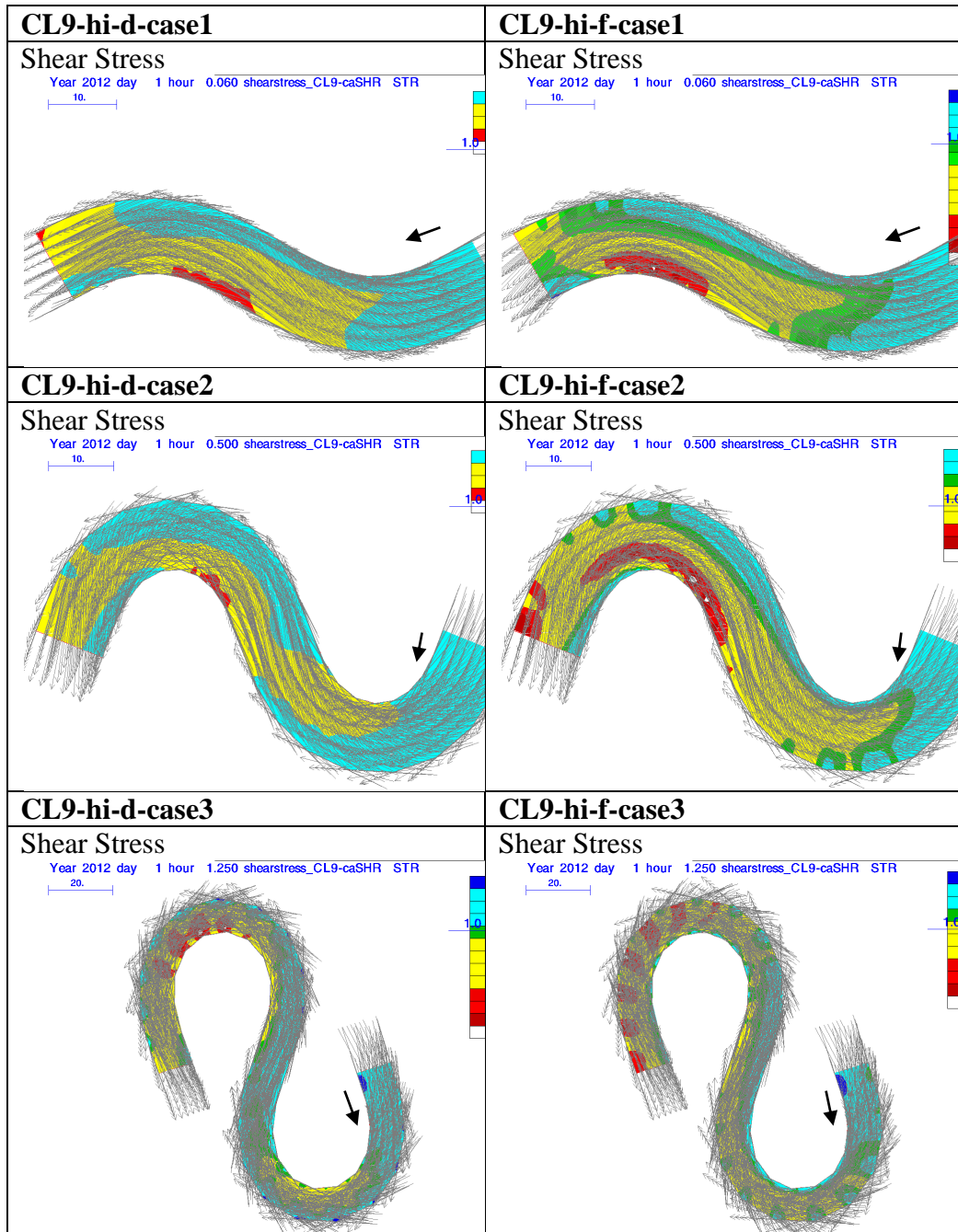


The bed deformation affects the intensity of helical flow where the more inclined bed makes the helical flow stronger as shown in Figure 3-8. According to (de Vriend, 1977), (Julien, 2002), and (da Silva & El-Tahawy, 2008), the intensity of the flow is influenced by bed shear stress. For each of deflection angle geometry, bed is inclined maximum at $\tan^{-1}\left(\frac{3}{11}\right) = 15.25^\circ$ where channel width is 11 m and bed height difference is 3 m.

In Table 3-5, bed shear stress for bed deformed channels are bigger than the flat ones. Agreed with (Struiksmas, et al., 1985), (Julien, 2002) and (Wu, 2008), that the bed deformation gives significant effect in the development of helical flow

since it governs the interaction between the turbulent flow motion and the suspended sediment constituting the river bed.

Table 3-5. Bed Shear Stress



For depth profiles at the outer bank, bed is deepened downward displacement where erosion zones coincide with acceleration zones. At the inner bank, bed is thickened upward displacement where deposition zone correspond to

deceleration zones. These are along with (da Silva, 2006) experiments, in Figure 3-8, the erosion is happened at the high accelerated zone where the bed is deepened, and the deposition is located at the low decelerated zone where the bed is thickened. Consequently, the erosion-deposition process govern the movement of meander either lateral expansion or downstream migration as referred to (da Silva, 2006) and (Garde, 2006). The process is also varied with deflection angles, as stated by (Esfahani & Keshavarzi, 2012) where migration is dominating for small deflection angle, and expansion is dominating for large deflection angle.

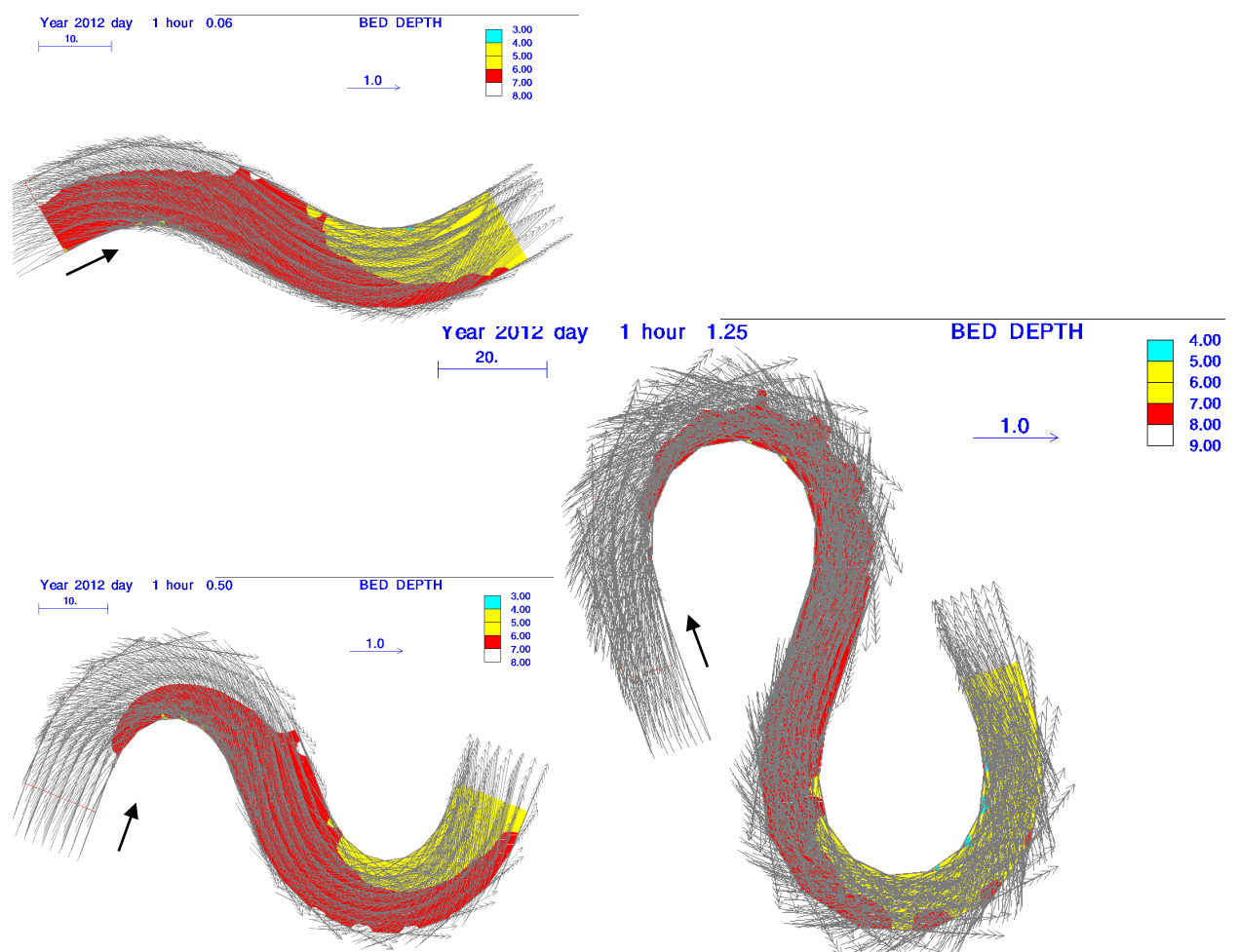


Figure 3-8. Bed depths

For sediment distribution, the highest concentration zone is located at the outer-bank where erosion occurs. The lowest concentration zone is place at the inner-bank where deposition happens, as in Figure 3-9. The flow is supercritical,

since at higher flow there are stronger secondary flows with maximum scour potential near the outer bank (Julien 2003), as seen in Figure 3-7, Figure 3-8, and Figure 3-9. About the bed erosion, it is related to the 4th and 5th point of approaches on the paper, which are: (4) simulating sediment transport process due to coherent structures and burst in meandering river, and (5) modeling eroding process as mechanical interaction fluid-soil at river bank. In the paper it is shown the distribution of sediment transport along the system for non-cohesive (sand/silt) sediment.

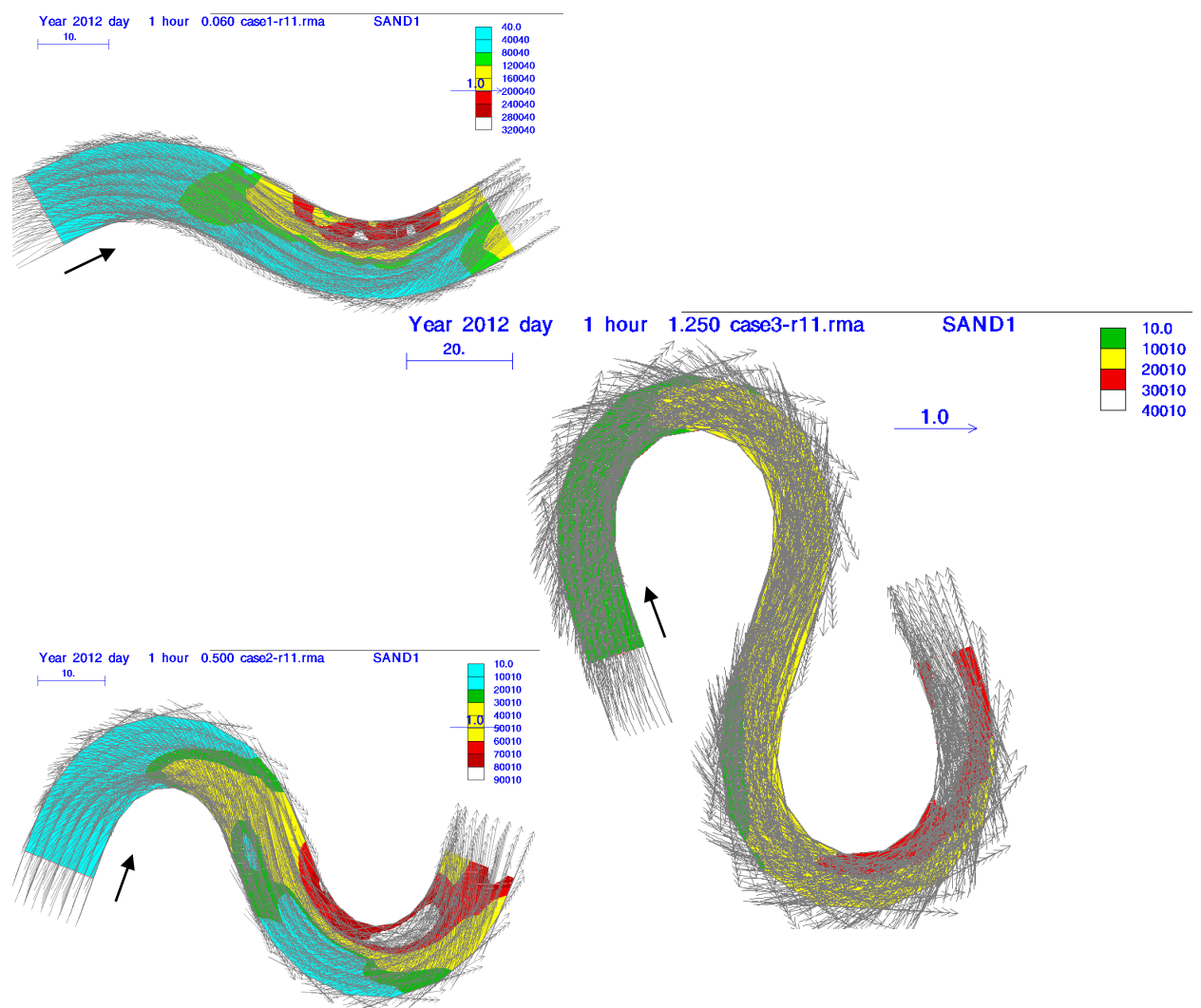


Figure 3-9. Non-cohesive (Sand) sediment concentrations

It took sometimes to get a better flow structures results with RMA-10. It is because a reasonable result of sediment transport depends on a reasonable result

of the flow structures in the system (Bates, et al., 2005). Meander occurs even when there is no sediment transport; meandering is caused by the large-scale turbulence (da Silva, 2006).

RMA-11 is using advection diffusion equation and erosion-deposition method for sand source/sink terms. Erosion and/or deposition are dependent on the bed shear stress developed by flowing water and the shear strength of the surface layer on the bed. Bed erosion will occur when it is above a critical level of a shear stress, and bed deposition will occur when the shear stress on the bed is not sufficient to re-suspend particles. Bed shear stress is a function of water density times to a square of shear velocity.

Julien (2002) stated when the strength of secondary circulation increases the equilibrium in river bends prevails between outer-bank erosion and inner-bank deposition. This strength has function of deviation angle of the streamlines near the bed which is a ratio of radial shear stress to the downstream bed shear stress (Julien, 2002).

The recent researches show that due to the gravitational force the flow in an open channel with a given slope would continuously accelerate, but a steady state is achieved due to friction at the bottom and the sidewalls. In other words, the equilibrium is due to a momentum transport from the flow to the walls. The momentum transport occurs in a turbulent flow, and has consequences for the transport of sediment. In a turbulent flow the exchange of momentum between different levels in the flow is mainly achieved by so-called flow structures, since the viscous contribution is rather small (Gyr, 2011). da Silva (2006) concluded that the zones of the downward and upward bed displacements (i.e. the erosion and deposition zones) must necessarily coincide with the zones of convective acceleration and deceleration of flow which can be explain by its flow structures (da Silva, 2006). These can be seen in Table 3-4, the circulation of velocity vectors at the center of the channel is different to at the inner and outer bank.

From here, we could predict the area where will occur the soil-water mechanical interaction at the erosion and deposition zones. The above simulations may have added significantly to our understanding of the controls upon secondary

circulation in the type of idealized channel geometries that have commonly been investigated in laboratory experiments.

Furthermore, we could connect this finding therefore we could quantify the erosion and deposition process by exploring RMA with finite element method (FEM). Otherwise, as we will discuss in Chapter 4, recent studies proposed a better result with meshless numerical method such smoothed particle hydrodynamics (SPH) where we could compare the results from RMA.

3.4 RESULTS COMPARISONS FOR MODEL VERIFICATION

Experimental study in meandering channel mostly focus on bed topography measurements such as by N. I. Makaveyev (1975) for small deflection angle and R. J. Jackson (1975) for large deflection angle (da Silva & El-Tahawy, 2008) as in Figure 3-10.

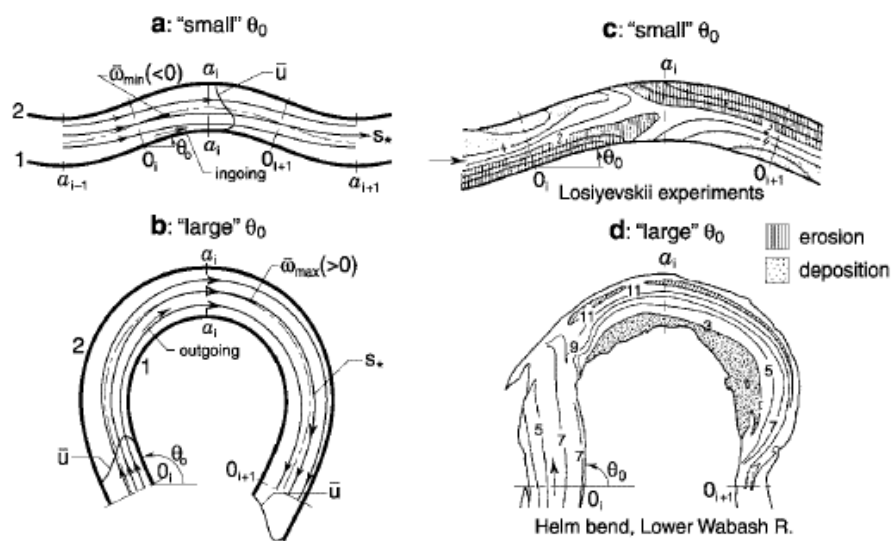


Figure 3-10. Flow convergence-divergence zones schematic representation (a and b), and measured bed topography illustration by (c) Makaveyev (1975) and (d) Jackson (1975) (DA SILVA, 2006)

da Silva (2006) affirmed the pattern of flow convergence-divergence zones in small and large deflection angle of sine-generated channel from series of laboratory measurements (Whiting and Dietrich, 1993; da Silva, 1995; Termini,

1996), and is confirmed by other experiment studies (Hasegawa, 1983; da Silva *et al.*, 2006; Termini, 2009; Binns, 2012; Xu and Bai, 2013).

Hasegawa conducted an experiment to measure flow field for sine-generated channel. One of the test cases is channel with deflection angle 30 degrees and called ME-2 case (Hasegawa, 1983). Xu and Bai run an experiment on bed topography evolution in sine-generated channels with flow field measurements for 30, 60 and 110 degree deflection angle channels (Xu & Bai, 2013). Binns (2012) run an experimental study for sine-generated channel with 70 degree deflection angle.

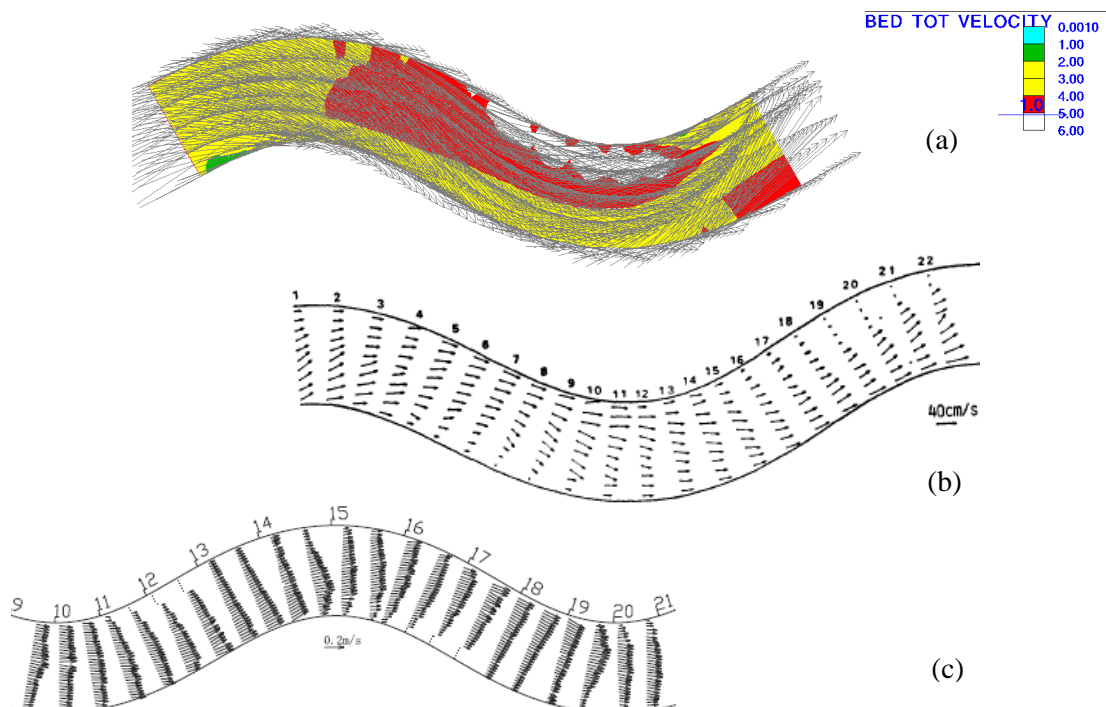


Figure 3-11. Flow structures in small deflection angle channel (a) computed by RMA, (b) run ME-2 measured by Hasegawa (1983), and (c) run RUN30-1 measured by Xu and Bai (2013)

As in Figure 3-10 (a) for small deflection angle, the patterns of flow structures computed by RMA can be compared with both measurement results in Figure 3-11 (b) by Hasegawa (1983) and in Figure 3-11 (c) by Xu and Bai (2013) where the maximum velocities zone takes place at the inner bank. This is agreed with da Silva (2006) that for small deflection angle the most intense convergence/divergence being is at the crossover-section of sine-generated

channel or at O_{i+1} in Figure 3-10 (a). The convergence/divergence flow exhibits deviation angle between the vertically-averaged streamlines and the longitudinal coordinate lines throughout its length and extends between the apex-section a_i and a_{i+1} in Figure 3-10 (a).

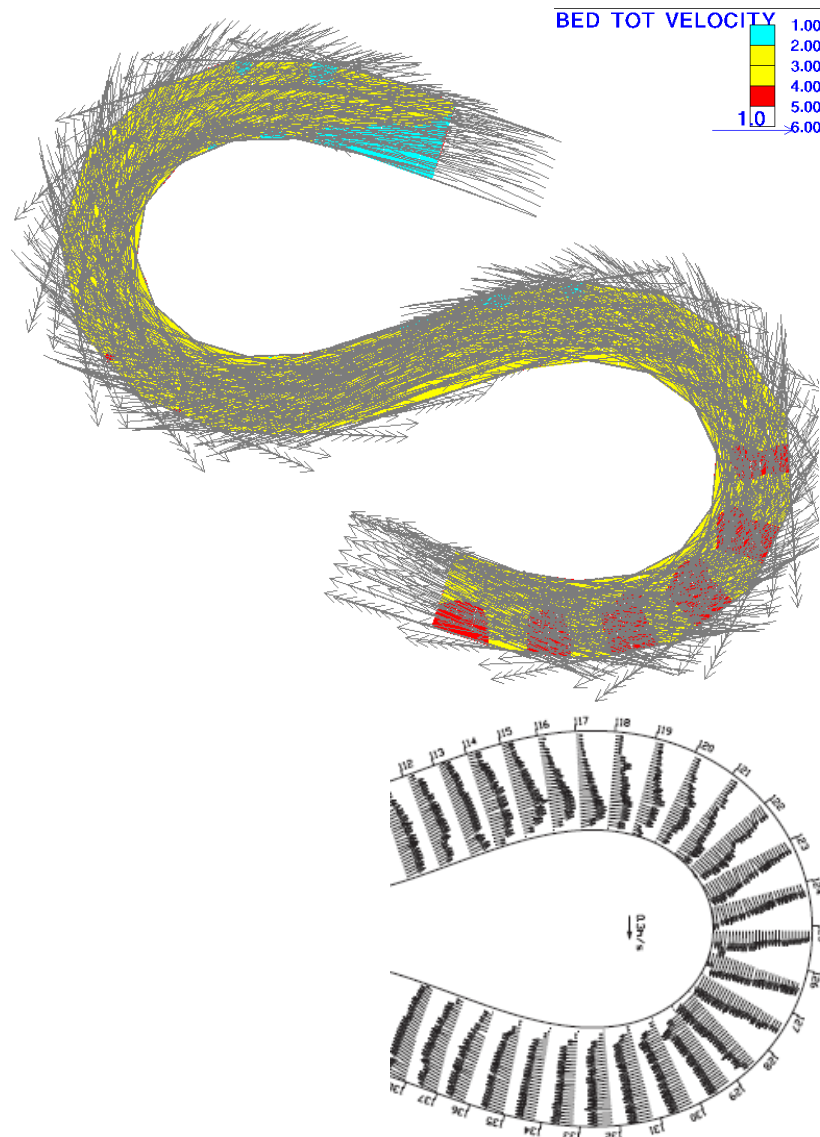


Figure 3-12. Flow structures in large deflection angle channel (a) computed by RMA, and (b) run RUN110-2 measured by Xu and Bai (2013)

As in Figure 3-10 (b) for large deflection angle, the patterns of flow structures computed by RMA can be compared with both measurement results in Figure 3-12 (b) by Xu and Bai (2013) where the maximum velocities zone takes

place at the outer bank downstream the apex-section a_i . This is agreed with da Silva (2006), for large deflection angle the most intense convergence/divergence being is at the apex-section of sine-generated channel or at a_i in Figure 3-10 (b). The convergence/divergence flow exhibits deviation angle between the vertically-averaged streamlines and the longitudinal coordinate lines approximately between the cross-section O_i and O_{i+1} in Figure 3-10 (b).

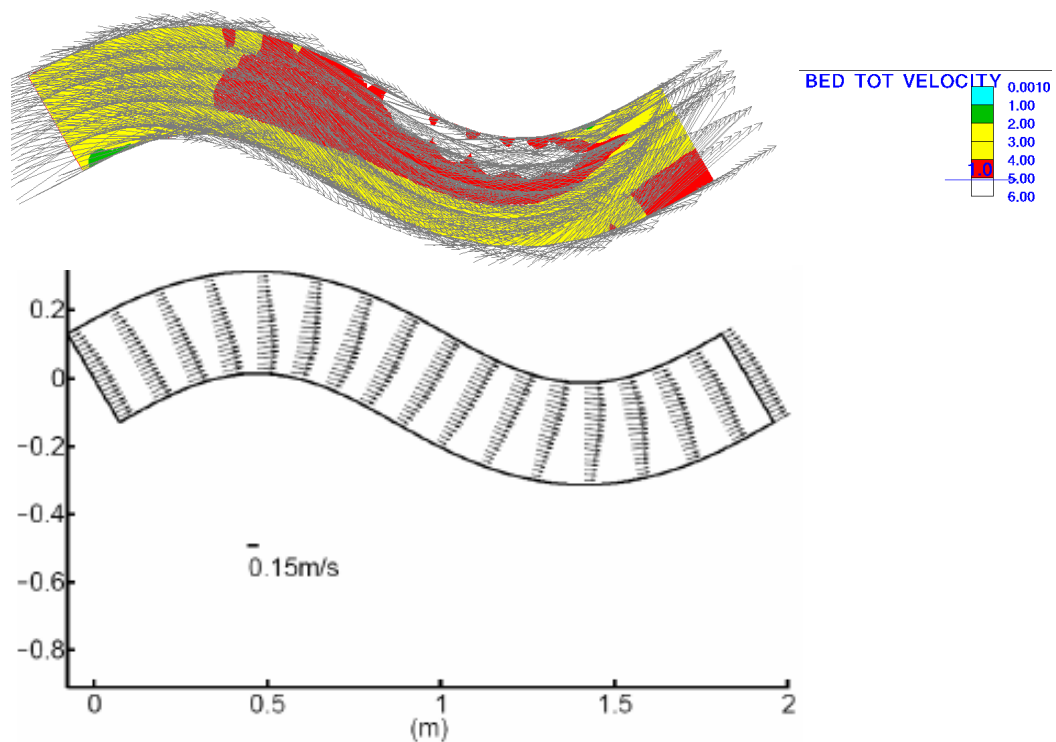


Figure 3-13. Flow structures in small deflection angle channel (a) computed by RMA, and (b) test case ME-2 Hasegawa (1983) by Dai (2008)

Wen Hong Dai (2008) tested the hydrodynamic model for vertically-average meandering flow developed by Yibing Zhang (2007); and chose the specific flow and bed conditions to match the experimental runs; (1) test case ME-2 by Hasegawa (1983) for 30° deflection angle channel, (2) test case #3 by Binns (2006) for 70° deflection angle channel, and (3) test case by Termini (1996) for 110° deflection angle channel (Dai, 2008). The test results produced flow fields in good agreement with measurements (Dai, 2008). We can compare the pattern of

flow structures computed by RMA with his test results, as depicted by Figure 3-13 for small, Figure 3-14 for medium, and Figure 3-15 for large deflection angle.

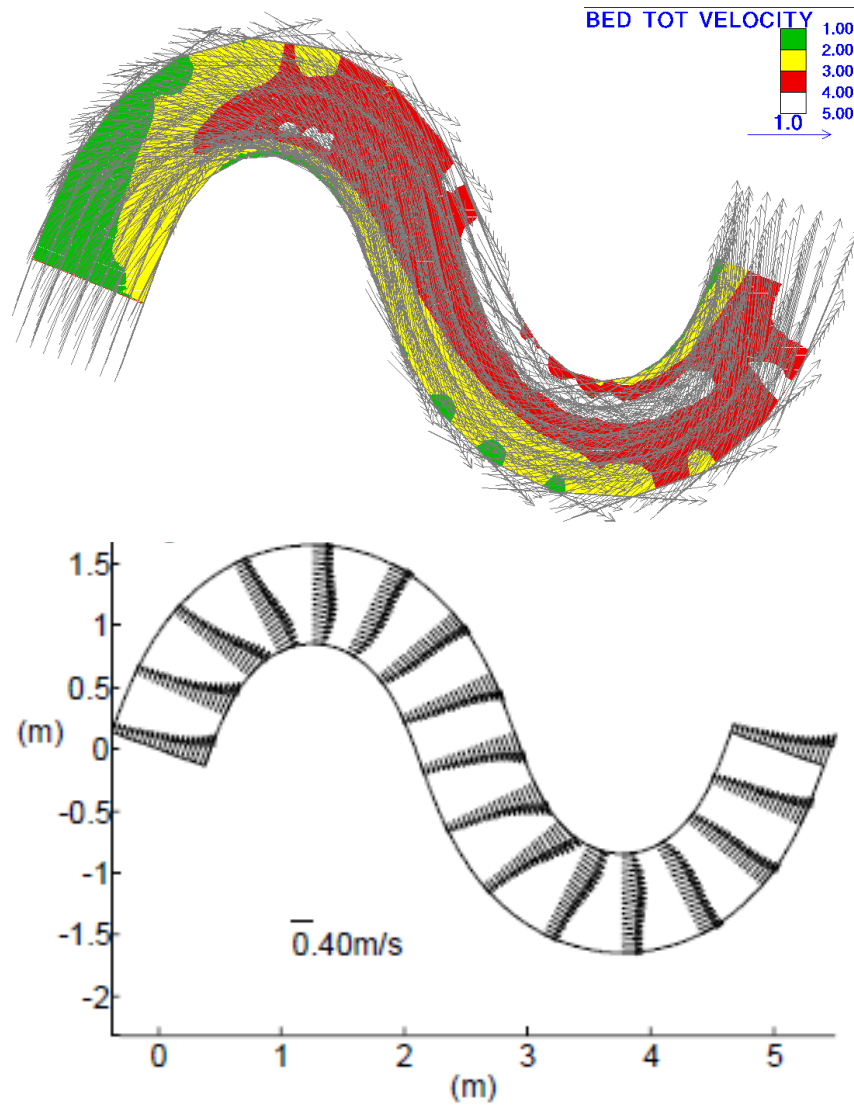


Figure 3-14. Flow structures in medium deflection angle channel (a) computed by RMA, and (b) test case #3 Binns (2006) by Dai (2008)

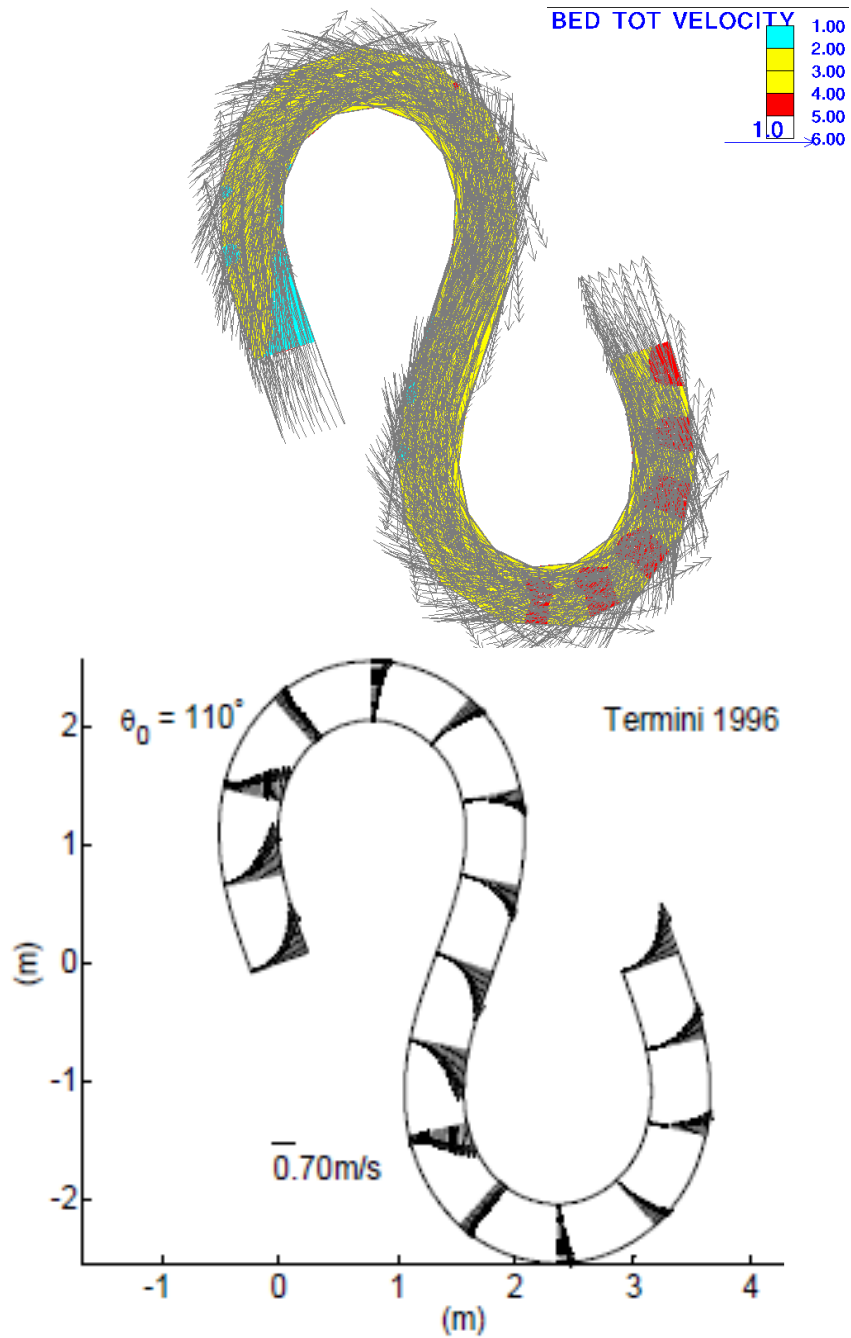


Figure 3-15. Flow structures in large deflection angle channel (a) computed by RMA, and (b) test case Termini (1996) by Dai (2008)

4 SPH METHOD

Since firstly introduced by (Gingold & Monaghan, 1977), and (Lucy, 1977), SPH gains popularity as a mesh-free method because it can overcome problems using fixed grid (Liu & Liu, 2003). The SPH method is modeled as an assembly of particles where the interaction zone is assumed to be around each of it. So, there is no need to describe all terms in governing equation on a fixed grid. The problem using grid arise from the numerical diffusion as a consequence of the advection terms in the equations. On the free surface, large deformation yields severe numerical diffusion (Shao & Gotoh, 2005).

Within several years, SPH established to reach a maturity that could perform better comparison to laboratory experiments of computational fluid dynamics. Different methods have been carried out to improve the original approach with the use of density filters and corrections of the kernel and its gradient. The methods base on derivations of the method of interpolants and the moving least-squares approaches. The classical SPH formulation for the Navier-Stokes equations is using compressible fluid assumption. Hence in simulating water, the artificial equation of state is used to define the relation between pressure and density (Gomez-Gesteira, et al., 2010).

4.1 BASIC FORMULATION

Basic formulation of SPH is consisted in two important steps; integral representation (or kernel approximation), and particle approximation according to (Liu & Liu, 2003) and (Monaghan, 2005). Integral representation of the function is the integration of an arbitrary function and a smoothing kernel function. Particle approximation of the function at a discrete point or a particle is approximation of the integral representation of the function by summing up the values of the nearest neighbor particles.

4.1.1 INTEGRAL REPRESENTATION AND SMOOTHING FUNCTION

Function f of the three-dimensional position vector r has integral representation

$$\langle f(r) \rangle = \int_{\Omega} f(r') W(r - r', h) dr' \quad (4-1)$$

where W is smoothing function (or kernel), h is smoothing length defining the influence area of the smoothing function, and Ω is the volume of the integral that contains r . The integral representation of equation (4-1) can only be an approximation as long as W is not the Dirac function. Integral representation of the derivative of a function for divergence ∇f and for laplacian $\nabla^2 f$ are

$$\langle \nabla f(r) \rangle = \int_{\Omega} [\nabla f(r')] W(r - r', h) dr' \quad (4-2)$$

$$\langle \nabla^2 f(r) \rangle = \int_{\Omega} [\nabla^2 f(r')] W(r - r', h) dr' \quad (4-3)$$

The conditions for W that must be satisfied are (1) normalization (or unity) condition where

$$\int_{\Omega} W(r - r', h) dr' = 1 \quad (4-4)$$

and (2) Delta function property where

$$\lim_{h \rightarrow 0} W(r - r', h) = \delta(r - r', h) \text{ and } \delta(r - r', h) = \begin{cases} 1 & x = x' \\ 0 & x \neq x' \end{cases} \quad (4-5)$$

and, (3) compact condition where

$$W(r - r', h) = 0 \text{ when } |r - r'| > \kappa h \quad (4-6)$$

with κ is a constant concerning smoothing function for point at r , and defines the effective (non-zero) area of the smoothing function as the support domain of that point.

The delta function to a smoothing kernel W with a characteristic width h (also called as the smoothing length or kernel width)

$$\lim_{h \rightarrow 0} W(r, h) = \delta(r) \quad (4-7)$$

subject to the normalization

$$\int_V W(r, h) dr' = 1 \quad (4-8)$$

Equation (4-7) and equation (4-8) must tend to a δ -function as $h \rightarrow 0$ and it must be normalized therefore the area under the curve is unity. It should have a continuous and well defined first derivative in order to calculate the gradients of

quantities, and be spherically symmetric from a symmetric argument, thus depend only on $r = |r - r'|$ and h . By definition, smoothing kernel obey the criteria set out in equation (4-2) and equation (4-3).

4.1.2 PARTICLE APPROXIMATION

The system in SPH method is defined as a finite number of particles that bear individual mass and occupy individual space. Particle approximation is discretization forms of the continuous integral representation by the summation over all the particles in the radius domain of smoothing length h , and S is the support domain.

Discretization of the integral representation of a function f is

$$f(r) = \sum_{j=1}^N \frac{m_j}{\rho_j} f(r_j) W(r - r_j, h) \quad (4-9)$$

and its particle approximation is

$$\langle f(r_i) \rangle = \sum_{j=1}^N \frac{m_j}{\rho_j} f(r_j) W_{ij} \quad \text{where } W_{ij} = W(r_i - r_j, h) \quad (4-10)$$

Approximation of the value of function f with vector coordinate r at particle i is using the average of those values of the function at all the particles within the support domain radius h of particle i weighted by the smoothing function W .

For the function derivative and the Laplacian, the particle approximation are

$$\langle \nabla f(r_i) \rangle = \sum_{j=1}^N \frac{m_j}{\rho_j} f(r_j) \nabla W_{ij} \quad \text{where } \nabla W_{ij} = \frac{x_{ij}}{r_{ij}} \frac{\partial W_{ij}}{\partial r_{ij}} \quad \text{and} \quad (4-11)$$

$$r_{ij} = r_i - r_j$$

$$\langle \nabla^2 f(r_i) \rangle = \sum_{j=1}^N \frac{m_j}{\rho_j} f(r_j) \nabla^2 W_{ij} \quad (4-12)$$

x_i is a unit vector in x -direction at particle i , and x_j is a unit vector in x -direction at particle j .

If the density ρ replaces the function f , the SPH approximation for the density is

$$\rho(r_i) = \sum_{j=1}^N m_j W_{ij} \quad (4-13)$$

Equation (4-11) is referred to as summation density approach and commonly used for obtaining density in SPH.

4.2 SPH PROCEDURE FORMULATIONS

This research develop algorithm compressible 3D flow from (Liu & Liu, 2003) and (Kelager, 2006) for nearly incompressible 3D water flow.

4.2.1 FLOW EQUATIONS

The Navier-Stokes equation for incompressible and isothermal fluid is presented by

$$\rho \frac{d\mathbf{u}}{dt} = -\nabla p + \mu \nabla^2 \mathbf{u} + \mathbf{F}^{\text{external}} \quad (4-14)$$

with ρ is mass density (kg/m^3), \mathbf{u} is vector velocity (m/s), t is time (second), p is pressure (N/m^2), μ is kinematic viscosity (Ns/m^2), and \mathbf{F} is external force (N).

Equation (4-14) can be modified into

$$\rho \frac{d\mathbf{u}}{dt} = \mathbf{F}^{\text{internal}} + \mathbf{F}^{\text{external}} = \mathbf{F} \quad (4-15)$$

Then for each particle I , the acceleration becomes

$$\mathbf{a}_i = \frac{d\mathbf{u}_i}{dt} = \frac{\mathbf{F}_i}{\rho_i} \quad (4-16)$$

where \mathbf{F} is a sum of force fields, internal forces $\mathbf{F}^{\text{internal}}$ and external forces $\mathbf{F}^{\text{external}}$.

Considered as internal forces, they are pressure force and viscosity force. For external forces, they are regarded as gravitation force, surface tension, and also buoyancy force.

SPH method uses velocity-pressure formulation to solve the momentum equation. Pressure is correlated to density in the thermodynamic equation of state. Based on the ideal gas law, pressure is proportional to density. The pressure of an isothermal fluid can be determined by using a gas stiffness constant k , which in theory only depends on the amount of particles. SPH uses a modified version of the ideal gas state equation with an additional rest pressure ρ_0 . The pressure p becomes (Desbrun & Gascuel, 1996):

$$p = k(\rho - \rho_0) \quad (4-17)$$

If the pressure is known for each particle, at particle I , the pressure force is

$$\mathbf{F}_i^{pressure} = -\nabla p(r_i) \quad (4-18)$$

Viscosity force at particle I is

$$\mathbf{F}_i^{viscosity} = \mu \nabla^2 \mathbf{u}(r_i) \quad (4-19)$$

Gravitation force is

$$\mathbf{F}_i^{gravity} = \rho_i \mathbf{g} \quad (4-20)$$

The surface tension force is resulted from the force density spreading onto all potential particles.

$$\mathbf{F}_i^{surface} = -\sigma \nabla^2 c_i \frac{\mathbf{n}_i}{|\mathbf{n}_i|} \quad (4-21)$$

The buoyancy force is for gaseous fluids and caused by diffusion of temperatures. For isothermal fluid, an artificial buoyancy force can be used as

$$\mathbf{F}_i^{buoyancy} = b(\rho_i - \rho_0) \mathbf{g} \quad (4-22)$$

If simulation is applied for isothermal water, then the buoyancy coefficient can be assumed as zero.

4.2.2 PARTICLE APPROXIMATION FOR MEANDERING FLOW EQUATIONS

The mass-density at particle I is approximated as

$$\rho_i = \sum_{j=1}^N m_j W(r_i - r_j, h) \quad (4-23)$$

The pressure force with symmetrical form can be written as

$$\mathbf{F}_i^{pressure} = -\rho_i \sum_{j \neq i} \left(\frac{p_i}{\rho_i^2} + \frac{p_j}{\rho_j^2} \right) m_j \nabla W(r_i - r_j, h) \quad (4-24)$$

The viscosity force with symmetrical velocity fields is defined as

$$\mathbf{F}_i^{viscosity} = \mu \sum_{j \neq i} (\mathbf{u}_j - \mathbf{u}_i) \frac{m_j}{\rho_j} \nabla^2 W(r_i - r_j, h) \quad (4-25)$$

The surface tension force at particle I with symmetrical form is approximated as

$$\mathbf{F}_i^{surface} = -\sigma \left[\sum_j \frac{m_j}{\rho_j} \nabla^2 W(r_i - r_j, h) \right] \frac{\left[\sum_j \frac{m_j}{\rho_j} \nabla W(r_i - r_j, h) \right]}{|n_i|} \quad (4-26)$$

where $|n_i| \geq l_i$, and $l_i > 0$ is the some threshold concerning the particle concentration.

4.2.3 SMOOTHING FUNCTION (KERNEL)

The most common smoothing function (kernel) is Gaussian function as the best kernel assumption to interpret the first golden rule of SPH, according to (Monaghan, 2005).

$$W(r, h) = \frac{1}{(2\pi h^2)^{\frac{3}{2}}} e^{-\frac{|r|^2}{2h^2}}, \quad h > 0 \quad (4-27)$$

where $|r|$ is scalar distance between particle. However, it is not always the best, where $W < 0$ for all r all particles within the domain contribute to the calculation. Consequently as the number of particles increase the kernel computational cost in numerical error from particle approximation (Price, 2004).

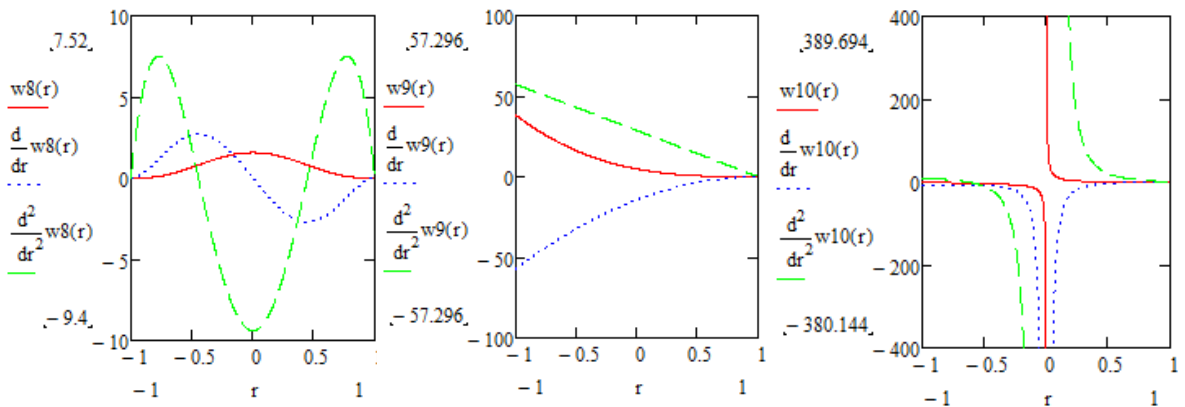


Figure 4-1. Smoothing kernel functions: poly6 ($w_8(r)$), spiky ($w_9(r)$), viscosity ($w_{10}(r)$)

Cubic spline kernels are often used for this reason, but in terms of computational accuracy, stability, and speed, (Müller, et al., 2003) designed kernels that have second order interpolation errors. The kernels are all even and normalized. Zero kernels with disappearing derivatives at the boundary are conducive to stability. The kernel is called poly6, noticeable as a simple kernel,

and preserve Gaussian bell curve (Kelager, 2006). More importantly according to (Müller, et al., 2003), r is in form of square which can be calculated without computing its square roots.

$$W_{poly6}(r, h) = \frac{315}{64\pi h^9} \begin{cases} (h^2 - |r|^2)^3, & 0 \leq |r| \leq h \\ 0, & |r| > h \end{cases} \quad (4-28)$$

$$\nabla W_{poly6}(r, h) = -\frac{945}{32\pi h^9} r (h^2 - |r|^2)^2 \quad (4-29)$$

$$\nabla^2 W_{poly6}(r, h) = -\frac{945}{32\pi h^9} (h^2 - |r|^2)(3h^2 - 7|r|^2) \quad (4-30)$$

where $|r| = r_{ij}$ which is the particle distance between particle i and j .

But kernel poly6 has disadvantage, under high pressure, particles using this kernel are likely to develop clusters. As a result, the repulsion force is gone whenever particles move very close to each other since the kernel gradient becomes zero at the center. Therefore, we are using spiky kernel as proposed by (Desbrun & Gascuel, 1996), (Müller, et al., 2003) and (Kelager, 2006). Gradient and Laplacian of spiky kernel are vanished at the boundary. This is necessary to generate repulsion forces.

$$W_{spiky}(r, h) = \frac{15}{\pi h^6} \begin{cases} (h - |r|)^3, & 0 \leq |r| \leq h \\ 0, & |r| > h \end{cases} \quad (4-31)$$

$$\nabla W_{spiky}(r, h) = -\frac{45}{\pi h^6} \frac{r}{|r|} (h - |r|)^2, \quad (4-32)$$

$$\lim_{r \rightarrow 0^-} \nabla W_{spiky}(r, h) = \frac{45}{\pi h^6}, \quad \lim_{r \rightarrow 0^+} \nabla W_{spiky}(r, h) = -\frac{45}{\pi h^6}$$

$$\nabla^2 W_{spiky}(r, h) = -\frac{90}{\pi h^6} \frac{1}{|r|} (h - |r|)(h - 2|r|), \quad (4-33)$$

$$\lim_{r \rightarrow 0} \nabla^2 W_{spiky}(r, h) = -\infty$$

Particular kernel for viscosity forces is designed by (Müller, et al., 2003) to get positive result of the Laplacian. Negative result of viscosity forces due to negative Laplacian kernel increases particles relative velocity, thus it can cause instability numerical computation. The relative viscosity can be damped by the viscosity forces on condition that the Laplacian is positive everywhere in the calculation domain (Kelager, 2006).

$$W_{viscosity}(r, h) = \frac{15}{2\pi h^3} \begin{cases} -\frac{|r|^3}{2h^3} + \frac{|r|^2}{h^2} + \frac{h}{2|r|} - 1, & 0 \leq |r| \leq h \\ 0, & |r| > h \end{cases}, \quad (4-34)$$

$$\lim_{r \rightarrow 0} W_{viscosity}(r, h) = \infty$$

$$\nabla W_{viscosity}(r, h) = \frac{15}{2\pi h^3} r \left(-\frac{3|r|}{2h^3} + \frac{2}{h^2} - \frac{h}{2|r|^3} \right), \quad (4-35)$$

$$\lim_{r \rightarrow 0} W_{viscosity}(r, h) = +\infty, \quad \lim_{r \rightarrow 0} W_{viscosity}(r, h) = -\infty$$

$$\nabla^2 W_{viscosity}(r, h) = \frac{45}{\pi h^6} (h - |r|) \quad (4-36)$$

4.2.4 BOUNDARY CONDITIONS AND INITIAL CONDITIONS

4.2.4.1 Boundary Conditions

In free surface water modeling, initial conditions and boundary conditions are defined to complete the system equations and find the solution equations numerically. Different conditions can give different results and responses in the modeling. At this time, the boundary conditions are limited to vertical and horizontal boundary.

Vertical boundary conditions for free surface water modeling is divided basically into bed and surface. The bed can be set as a datum $z_{bed} = 0.0$ [meter], and having slope if $dz \neq 0$. At the surface is free surface under atmospheric condition where the pressure $p_{surface} = 0.0$ [Pascal].

Horizontal boundary conditions is bordered on lateral x - and y -directions. As the cross points, we are using Cartesian coordinates $(0,0,0)$, and defines the axis as a center-line where $f_{axis} = f(x, y)$. At the wall, we apply $f_{wall} = f(x, y_{max,min})$ for $0 \leq x \leq L$, where L is channel length in meter.

Inlet and outlet will be defined if we set the water flows continuously. At the wall and bed, the material is chosen to be solid where there are no mass flux crossing in and out. Thus, the normal velocity to the wall and bed is zero or $\vec{v} \cdot \vec{n} = 0$. This condition is called as no-slip condition, and generally used in free surface water modeling (Ji, 2008).

4.2.4.2 Initial Conditions

For the free surface water system, we choose unsteady flow, dependent on time, hence the initial time is $t_0 = 0.0$. Initial velocities and coordinates for x , y , and z directions are set for all particles.

The free surface water system is defined as shallow water and long wave (Ji, 2008). Time step is defined for each time integration calculation and based on number of Courant-Friedrichs-Lewy (CFL) to check the numerical stability in the computation (Kao & Chang, 2012) and (Chapra, 1997).

$$\Delta t = CFL * \min\left(\frac{h}{c_i + |\vec{v}_i|}\right) \text{ for } 0 \leq CFL \leq 1 \quad (4-37)$$

where h is the SPH computation domain radius or smoothing length, c_i is gravity wave speed of propagation, and $|\vec{v}_i|$ is the magnitude of velocity for particles.

5 FLOW SIMULATIONS WITH SPH

SPH program is developed to simulate basic characteristics of meandering process which are helical flow. We simplify sine-generated channel into a curved channel in order to eliminate complex curvature factor for helical flow initiation. The program development is planning in several stages. The first stage is to build 3D fluid flow as the back bone of the program. The second stage is to handle collision between water particles to its boundary. The objectives of the experimental scenario are:

- to model water properties behavior
- to simulate secondary flow and helical flow in a curved channel

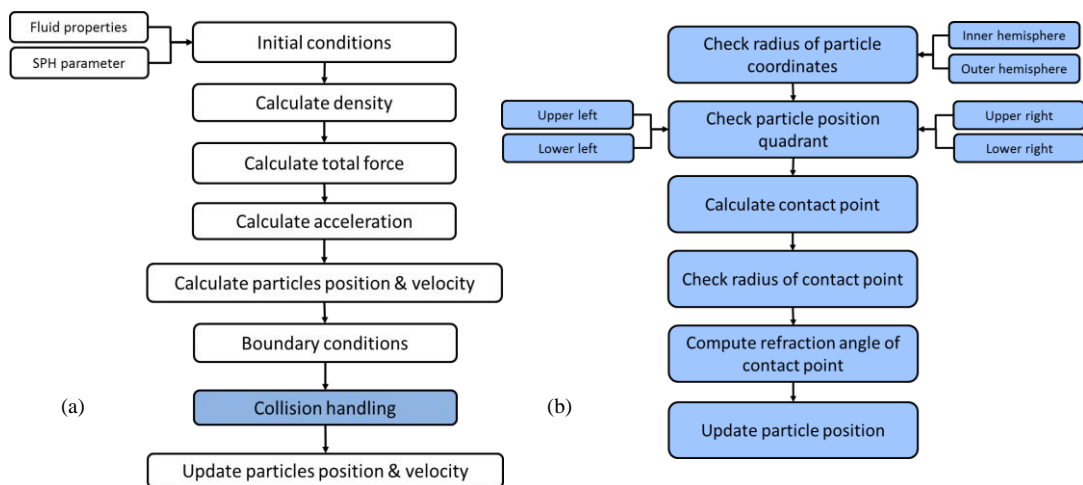


Figure 5-1. Process description for (a) the general algorithm, and (b) collision handling algorithm

5.1 3D FLUID FLOW MODEL

The program code in Figure 5-2 is writing in FORTRAN language in F95 form, and the results plot with GNUPLOT version 5.0.

Parameters is defined by water, common physics and SPH properties. Initial condition are velocity and position for each particle at zero time, and determined as input model. From the input, it calculates total force and density for each particle. Total force equals to the summation of internal forces (pressure and

viscosity), and external forces (gravity and surface tension). Then, it computes acceleration with (4-16) from total force divided by density for each particle.

Afterwards, it updates new velocity and new position from the acceleration for each particle at each time step. Later, this new velocity and new position will be used to calculate new total force and new density for each particle at next time step. The new total force and new density will be applied to compute new acceleration, and so on until it reaches maximum time step in the end.

If we define space, for each new velocity and new position, it checks collision between particles and its boundary conditions before it goes to the next time step. The space is set as a curved channel, and the collision determines water flow movement, in this case is primary flow.

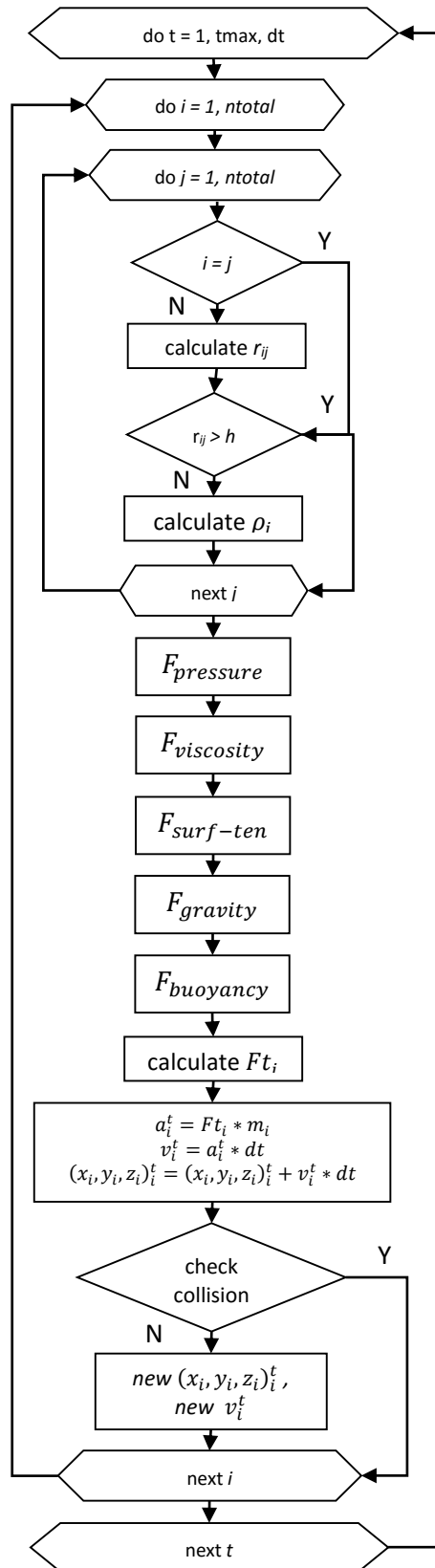


Figure 5-2. Fluid flow program flow chart

5.2 NUMERICAL SIMULATION

5.2.1 PARAMETERS AND PROPERTIES

Parameters in numerical simulation are common, fluid, and SPH properties as shown in Table 5-1.

Table 5-1. Parameter properties

Fluid				SPH & common			
Description	Symbol	Value	Unit	Description	Symbol	Value	Unit
Viscosity	μ (mu)	0.01	Pa.s	Gravitational acceleration	g	[0, 0, -9.819] ^T	m/s ²
Density rest	at rest	1000.0	kg/m ³	Pressure	p	101325 (1)	Pa (Atm)
Surface tension	σ (sigma)	0.0736	N/m	Time step	Δt	0.01	s
Stiffness	ka	0.00001	J	Smoothing length	h	0.1	m
Restitution	cr	1.0	-	Threshold	lt	0.001	
Buoyancy	bu	0.0	-	Mass	mass	0.49622	kg
Temperature	T	293.15 (20)	K (°C)	Particle number	n	4811	-

Noted that simulations use 0.01 second for each time step. This value is chosen after several trials from 0.001 second up to 1 second, and checked with Courant number in equation (4-37). If the time step is smaller than 0.01, the simulations take a longer computation time especially for big particle numbers. If the time step is bigger than 0.01, the simulation computations become unstable and stuck in the middle of running program.

5.2.1.1 Checking sensitivity of fluid properties and modeling parameter

Discretizing fluid system into large particle number results in consistent accuracy but also high runtime computation as stated by (Liu & Liu, 2003) and can be seen in the following Figure 5-3. In this research, we varied particle number from 10 up to 4000 particles. Nevertheless, this simulation uses 4811 particle numbers to gain the accuracy of the solution.

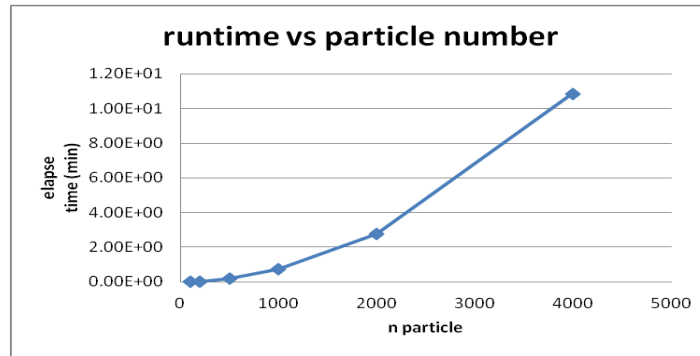


Figure 5-3. Runtime versus particle number

Fluid properties and modeling parameter is simulated through several loops in order to see how the system response under parameters variation of density and pressure.

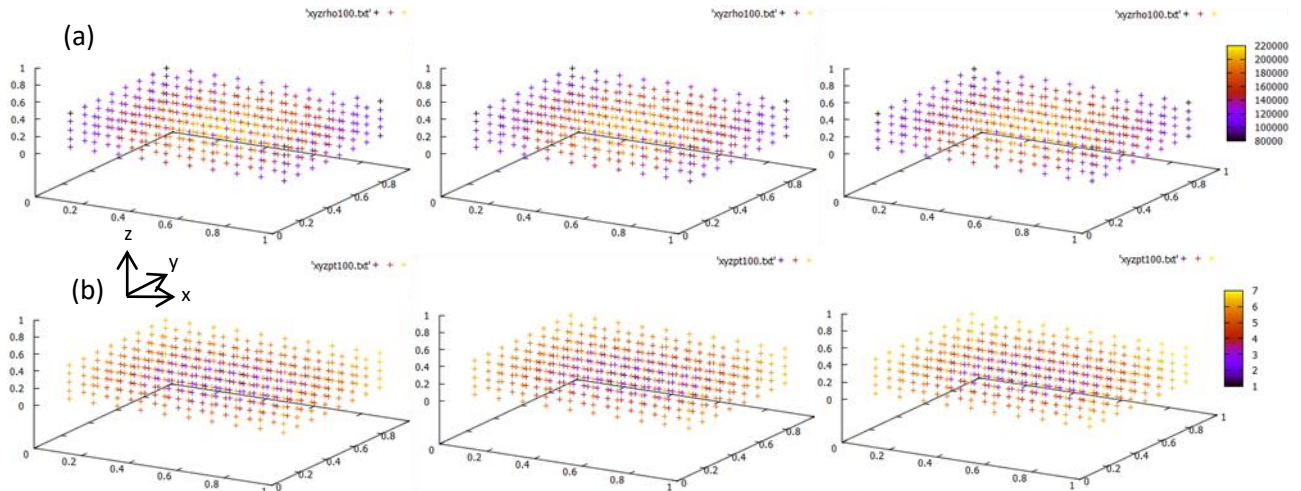


Figure 5-4. At $t = 100 dt$, (a) Density Response (left to right) Due to the Difference of Rest Density 100 kg/m^3 , 1000 kg/m^3 , 10000 kg/m^3 ; (b) Pressure Response (left to right) Due to the Difference of Rest Density 100 kg/m^3 , 1000 kg/m^3 , 10000 kg/m^3

The basic fluid properties are using three variations; rest density (100, 1000, 10000 kg/m³), mass (0.48, 480, 480000 kg), viscosity (1.007e-0, 1.007e-3, 1.007e-6 Pa.S), and initial velocity ($v_x = 10$ m/s, $v_y = 10$ m/s, $v_z = 10$ m/s, arbitrary). The numerical property is smoothing length (0.1, 1.0, 10 m). The time stepping dt is 0.001 s, and looping for 100 times.

Rest density, mass, viscosity, and initial velocity are the fluid properties that have significant influence on density and pressure of fluids. Rest density is a condition where fluid has no attractive and repulsive forces. Increasing value of rest density will expand fluid since its density is a way denser than rest density. The pressure tends to stay unchanged since its volume is enlarging. Mass gives resistance to fluid expansion due to gravity force. It reduces the repulsive force and slows the expansion. Denser fluid has higher viscosity holds the repulsive force for the same amount of fluid mass.

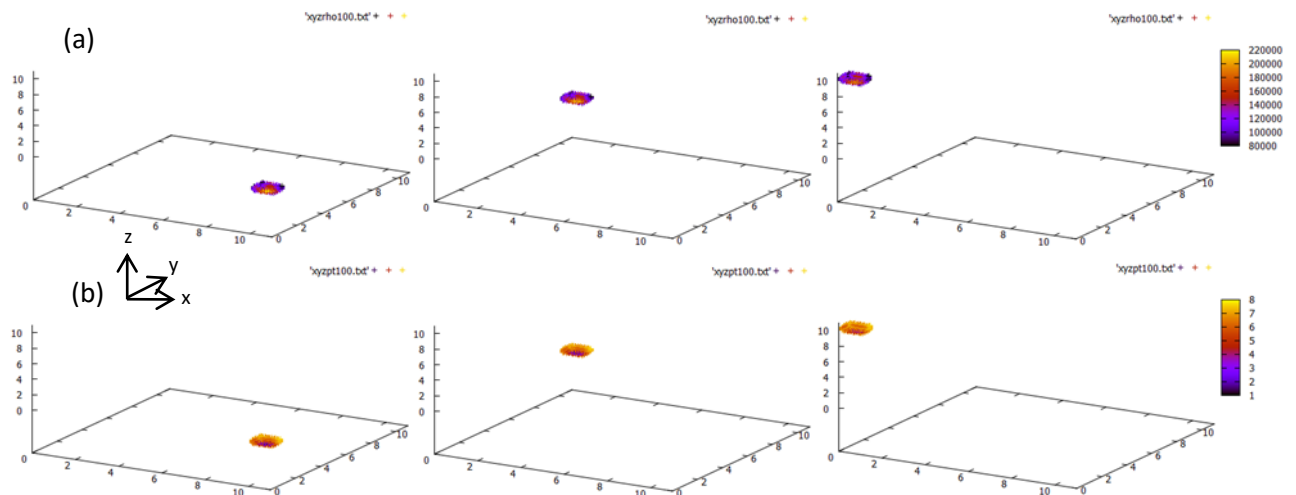


Figure 5-5. At $t = 100 dt$, (a) Density Response (left to right) Due to the Difference of Initial Velocity ($v_x = 10$ m/s, $v_y = 10$ m/s, $v_z = 10$ m/s; (b) Pressure Response (left to right) Due to the Difference of Rest Initial Velocity ($v_x = 10$ m/s, $v_y = 10$ m/s, $v_z = 10$ m/s

Initial velocities drift the fluid particles and work as an advective term, while the densities and pressures expand the fluid's volume and act as a dispersive term.

Up to this point, the 3D flow SPH program give a stable results as expected from fluid properties. In running time integration based on Verlet method, the program runs smoothly for each given time.

The basic of SPH is presented in the order from its formulations, integral representations and kernel functions, and particle approximations. The SPH formulations are developed for 3D fluid flow and sedimentation transport equations. The logical frame of the program development is drawn in an algorithm, and the program code is written in FORTRAN language.

The numerical experimental results show that the program has capability to simulate the basic behavior of fluid properties as the basis characteristics of meandering river. The calculation is stable during the time looping for the given initial particles conditions.

The next stage, the 3D flow program will consider the collision handling when the fluid particles hit the boundary.

5.2.2 BOUNDARY CONDITIONS

For basic simulation, the system are bounded as a box that has length, width and height (depth). There are two ways to build the boundaries, by generating stacks of particles or setting range of walls.

5.2.2.1 Collision handling at plane area

As starter, boundaries is drawn as straight wall at certain coordinate such $x = a$, where a is a constant parameter.

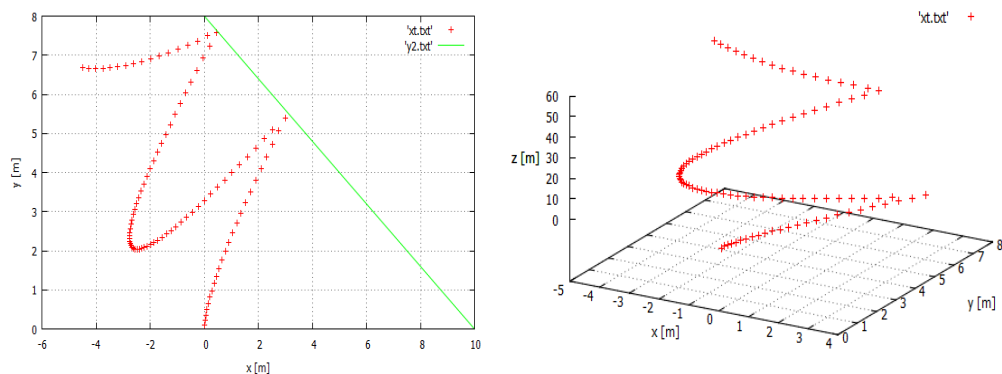


Figure 5-6. Particle interactions with plane area

5.2.2.2 Collision handling at curved wall

In order to set particle interactions at curved wall, boundaries are drawn as standing tube.

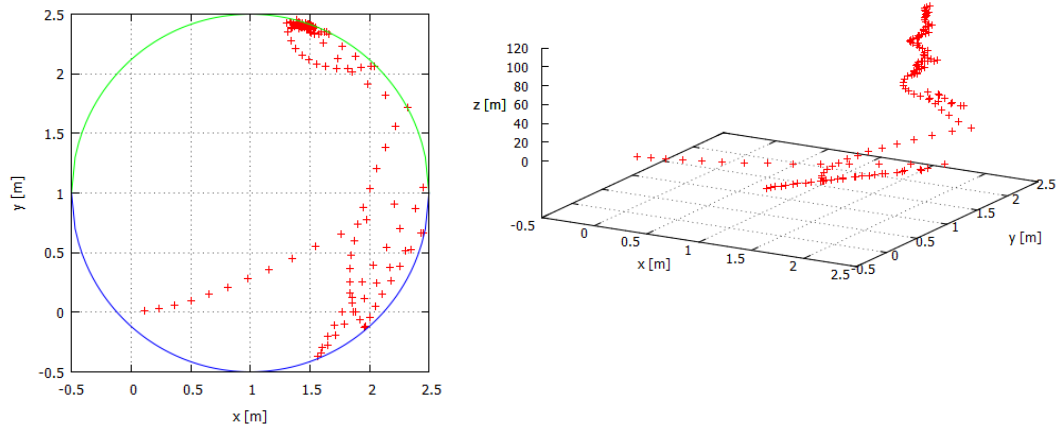


Figure 5-7. Particle interactions with cylindrical wall

5.2.2.3 Collision handling at curved channel

Meander morphology is a very complex geometry. Thus, we need to simplify it into a curved channel in order to separate the effect of helical flow formation from complex geometry.

Collision handling works whenever there is contact with the walls; four straight walls and four quarter-circle walls. At $t = t$, coordinate of a particle i is $(x(i), y(i), z(i))$, and at $t = t + dt$, its coordinate becomes $(xt(i), yt(i), zt(i))$.

A contact point is $(xc(i), yc(i))$ where a particle collides with a wall at any $zc(i)$. We consider that curved channel has very high wall. At this time, we use Snell's law where angle and velocity of incidence equals to angle and velocity refraction.

Center of curved channel has coordinate at x - and y -coordinate $(xr, yr) = (2, 3)$, and any z -coordinate zr . Radius of outer hemisphere from the center is $rr = 2 \text{ meter}$, and of inner hemisphere is $rr2 = 1 \text{ meter}$. The bed of curved channel is set up at $zbase = 0 \text{ meter}$ for all x - and y -coordinates.

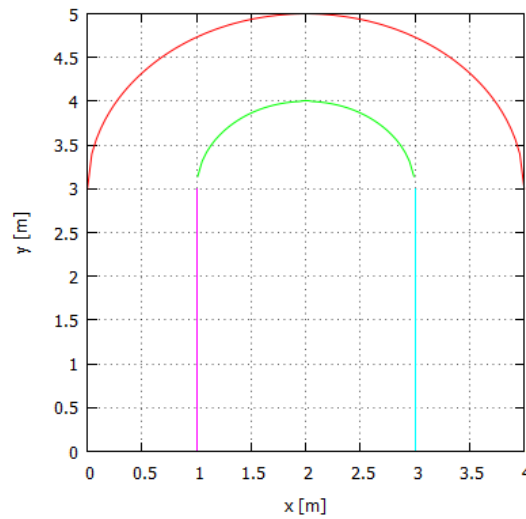


Figure 5-8. Boundary conditions for a curved channel

Coordinate in x -direction in meter for each plane wall are $xbase1 = 0$, $xbase2 = 1$, $xbase3 = 3$, and $xbase4 = 4$. Angle of refraction is in radians, and depends on quadrant of particle coordinate.

Area of particle movement is wherever (1) $y(i)$ is less than y_r then particle collision uses algorithm for plane walls, or (2) $y(i)$ is greater than or equivalent to y_r thus particle collision utilizes algorithm for curved walls.

Plane walls

A particle collides a plane wall whenever (1) $xt(i) \leq xbase1$, (2) $xbase2 \leq xt(i) \leq xbase3$, or (3) $xbase4 \leq xt(i)$. Calculation of contact point is determined as in the following,

$$xc(i) = xbase, \text{ depends where a particle collides} \quad (5-1)$$

$$yc(i) = y(i) - \left(\frac{(x(i) - xc(i)) * (y(i) - yt(i))}{x(i) - xt(i)} \right) \quad (5-2)$$

$$\gamma = atan \left(\frac{yc(i) - yt(i)}{xc(i) - xt(i)} \right) \quad (5-3)$$

Curved walls

Collision condition at curved channel whenever radius of a particle relatively to the center of a curved channel is (1) greater than outer hemisphere radius ($rxt > rr$), or (2) less than inner hemisphere radius ($rxt < rr2$).

$$rxt = \sqrt{(xt(i) - xr)^2 + (yt(i) - yr)^2} \quad (5-4)$$

Contact point is located at hemisphere. There are two initial guesses $xc(i)$ and $yc(i)$. Coordinate $yc(i)$ is estimated between $y(i)$ and $yt(i)$. Computation of $yc(i)$ uses bisection method (Chapra & Canale, 2010) and (Cheney & Kincaid, 2008), afterward $xc(i)$ is calculated under condition, if

$rxt > rr$ then,

$$xc(i) = xr - (((rr + yc(i) - yr)^{0.5}) * ((rr - yc(i) + yr)^{0.5})), (xt(i) \leq xr) \quad (5-5)$$

$$xc(i) = xr + (((rr + yc(i) - yr)^{0.5}) * ((rr - yc(i) + yr)^{0.5})), (xt(i) > xr) \quad (5-6)$$

$rxt < rr2$ then,

$$xc(i) = xr - (((rr2 + yc(i) - yr)^{0.5}) * ((rr2 - yc(i) + yr)^{0.5})), (xt(i) \leq xr) \quad (5-7)$$

$$xc(i) = xr + (((rr2 + yc(i) - yr)^{0.5}) * ((rr2 - yc(i) + yr)^{0.5})), (xt(i) > xr) \quad (5-8)$$

After contact point coordinates is set up, radius of contact point from the center of hemisphere is calculated only to check whether the radius falls right at one of hemisphere walls.

$$rc = \sqrt{(xc(i) - xr)^2 + (yc(i) - yr)^2} \quad (5-9)$$

Refraction angle computation depends on where the location of contact point. The angle detection varies by hemisphere radius, slope between contact point and curved channel center, and contact point quadrant.

If $rxt > rr2$ where a particle lies outside outer hemisphere then,

$$mc = \left(\frac{(rr - xc(i) + xr)^{0.5}}{2 * ((rr + xc(i) - xr)^{0.5})} \right) - \left(\frac{(rr + xc(i) - xr)^{0.5}}{2 * ((rr - xc(i) + xr)^{0.5})} \right) \quad (5-10)$$

Else if $rxt < rr2$ where a particle remains inside inner hemisphere then,

$$mc = \left(\frac{(rr2 - xc(i) + xr)^{0.5}}{2 * ((rr2 + xc(i) - xr)^{0.5})} \right) - \left(\frac{(rr2 + xc(i) - xr)^{0.5}}{2 * ((rr2 - xc(i) + xr)^{0.5})} \right) \quad (5-11)$$

Next steps are calculation of refraction angle γ :

$$x1 = xr \quad (5-12)$$

$$y1 = yc(i) + mc * (x1 - xc(i))$$

$$\alpha = atan\left(\frac{y1 - yc(i)}{x1 - xc(i)}\right) \quad (5-13)$$

$$\beta = atan\left(\frac{yt(i) - yc(i)}{xt(i) - xc(i)}\right) \quad (5-14)$$

$$\alpha = atan\left(\frac{y1 - yc(i)}{x1 - xc(i)}\right) \quad (5-15)$$

$$\theta = \beta - \alpha \quad (5-16)$$

$$\eta = atan\left(\frac{y(i) - yc(i)}{x(i) - xc(i)}\right) \quad (5-17)$$

If mc is positive then,

$$\delta = \alpha - \theta \quad (5-18)$$

Else if mc is negative then,

$$\delta = \alpha + \theta \quad (5-19)$$

The challenging part is where we have to identify the particle position quadrant, because previously we have to determine its incidence angle quadrant as relative to its contact point. After refraction angle of each particle is calculated, each particle position is updated where,

$$rcxt(i) = \left((xt(i) - xc(i))^2 + (yt(i) - yc(i))^2 \right)^{0.5} \quad (5-20)$$

$$xt(i) = xc(i) + rcxt(i) * \cos(\gamma) \quad (5-21)$$

$$yt(i) = yc(i) + rcxt(i) * \sin(\gamma) \quad (5-22)$$

$$zt(i) = 2 * zbase - zt(i) \quad (5-23)$$

$$vxt(i) = ((vxt(i) ** 2 + vxt(i) ** 2) ** 0.5) * \cos(\gamma) \quad (5-24)$$

$$vyt(i) = ((vxt(i) ** 2 + vxt(i) ** 2) ** 0.5) * \sin(\gamma) \quad (5-25)$$

$$vzt(i) = -1 * vzt(i) \quad (5-26)$$

The algorithm for curved channel collision handling can be seen at Figure 5-9 in the following.

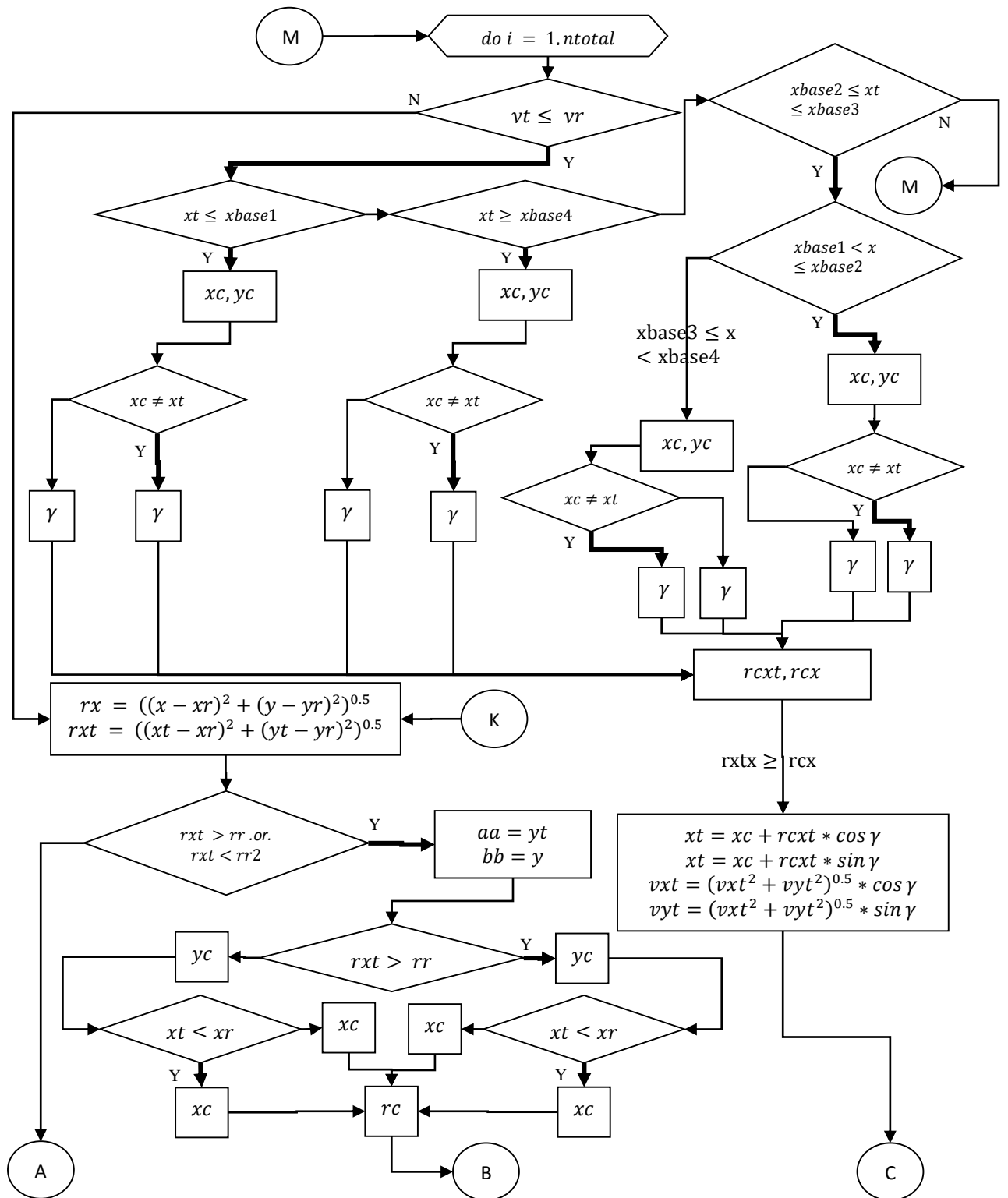


Figure 5-9. Particle interactions with curved channel flow chart (part 1 of 4)

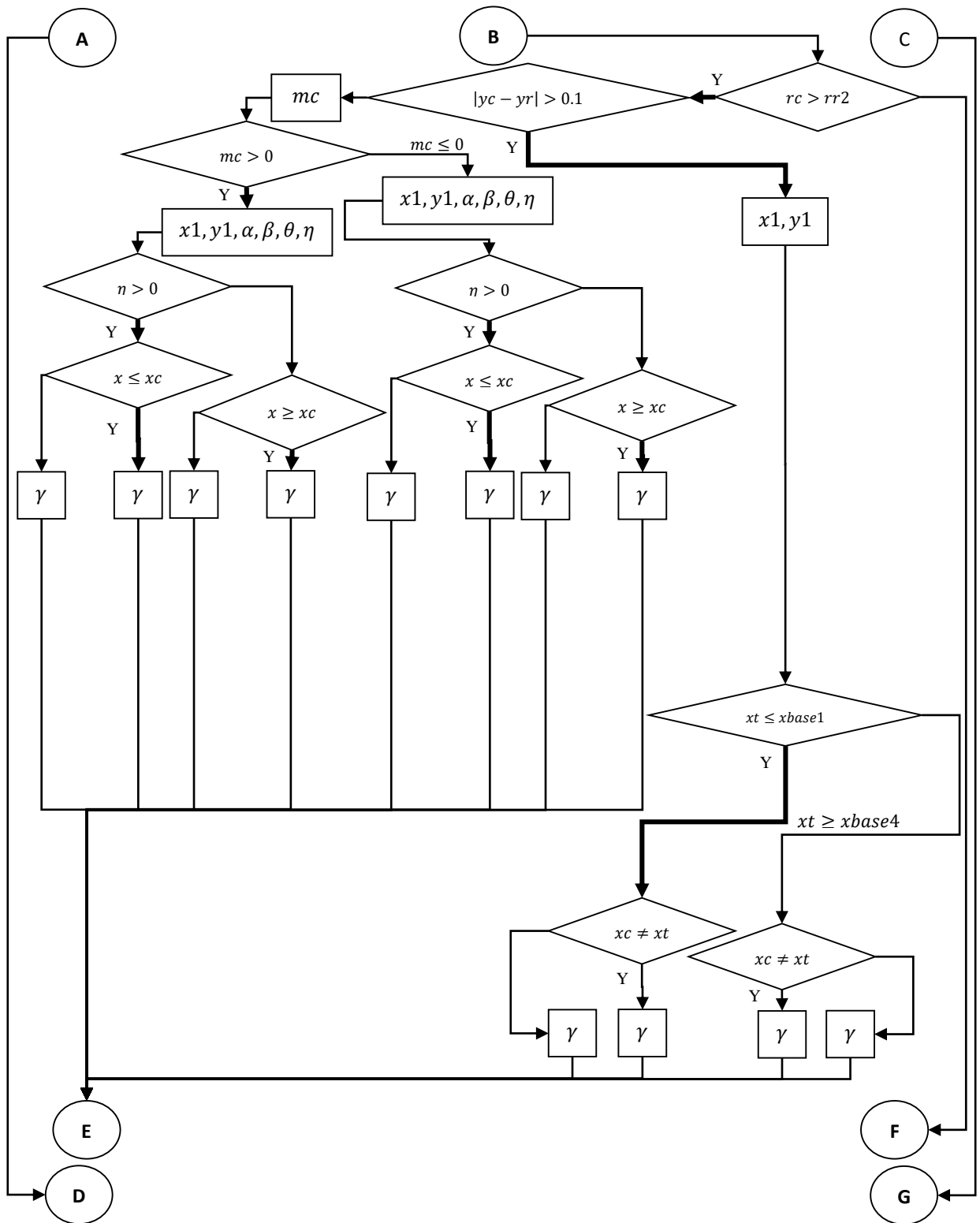


Figure 5-9. Particle interactions with curved channel flow chart (part 2 of 4)

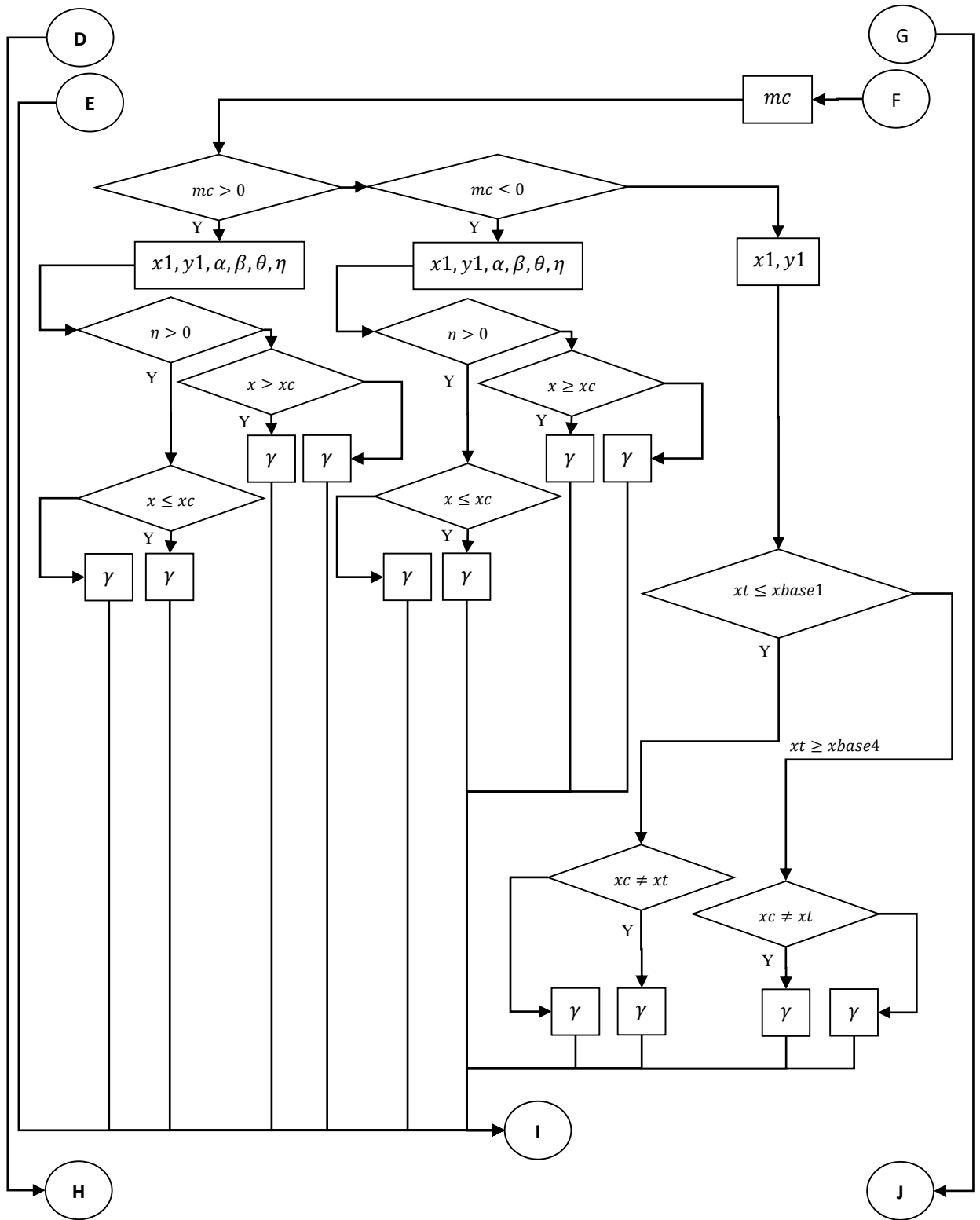


Figure 5-9. Particle interactions with curved channel flow chart (part 3 of 4)

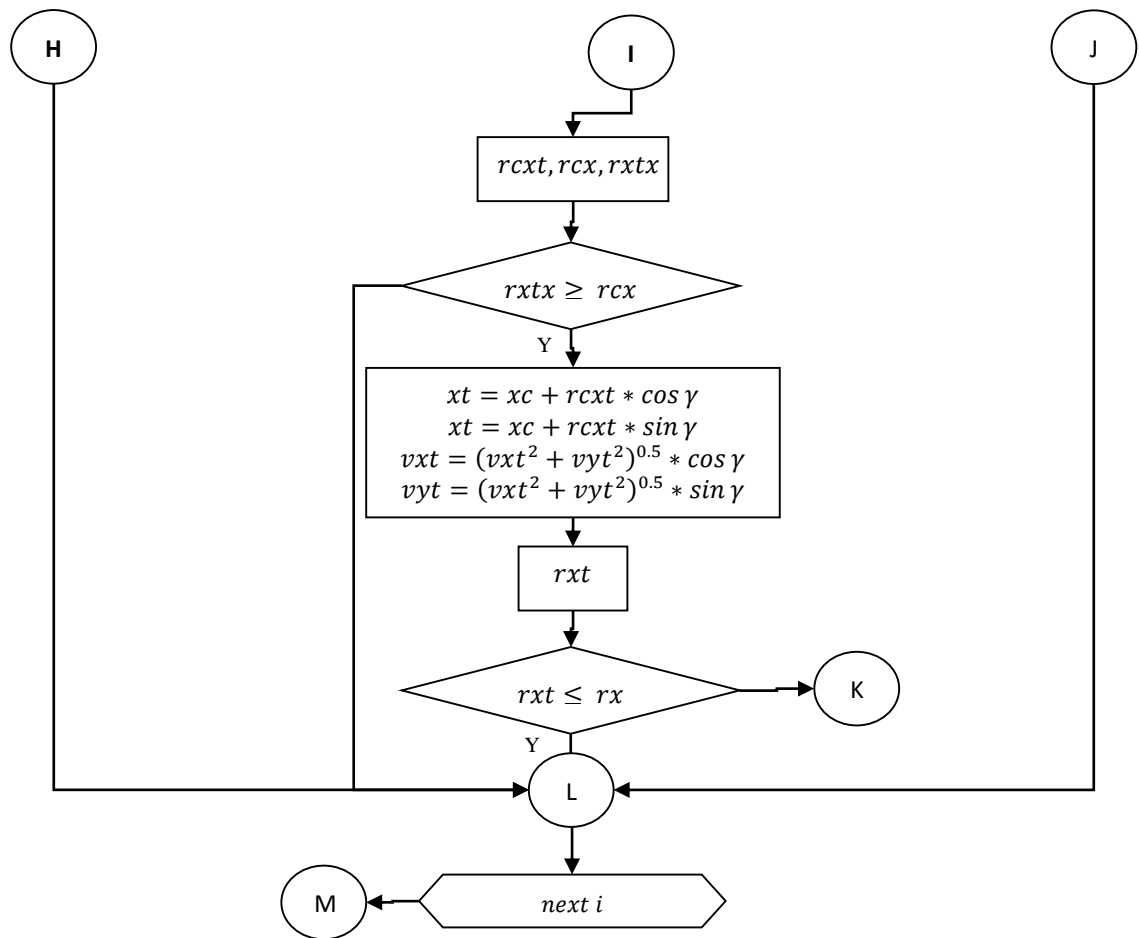


Figure 5-9. Particle interactions with curved channel flow chart (part 4 of 4)

5.2.3 INITIAL CONDITIONS

There are 4811 particle numbers. Initial time, set at $t = 0$, all particles forms as a cube with dimension of 1 meter width by 1 meter length by 1 meter height, and weighs 0.9622 kilogram.

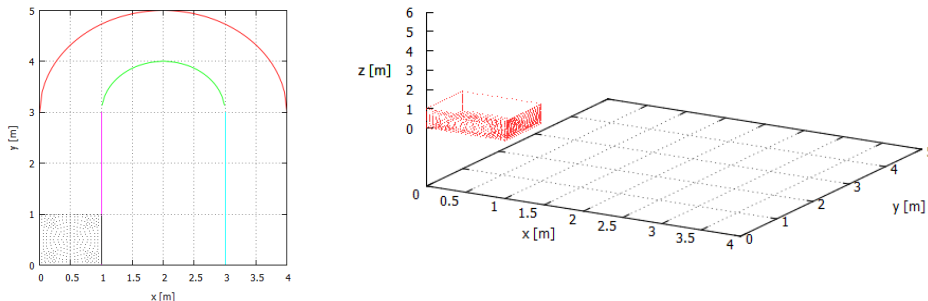


Figure 5-10. Initial condition for particle interactions with curved channel plan and 3D view

Initial velocity is set at variation afterwards in order to see particles flow behavior. Particle number independence test is done by using particle number resolution at initial from 1000 to 9622 particles. The solution is independent to particles number at 4811 particles.

5.2.4 FLOW SIMULATIONS IN CURVED CHANNEL

Scenario simulations are at first checking refraction angles as a result of a particle interaction with curved channel walls. Next, initial velocity is varied between inviscid and viscous flow, and then by gravity magnitudes.

5.2.4.1 Inviscid Flow

At initial conditions, all particle has inviscid uniform velocity only in y -direction $v_{y0} = 0.8$ m/s. All particles have the same fluid properties as mentioned above in table 5.1.

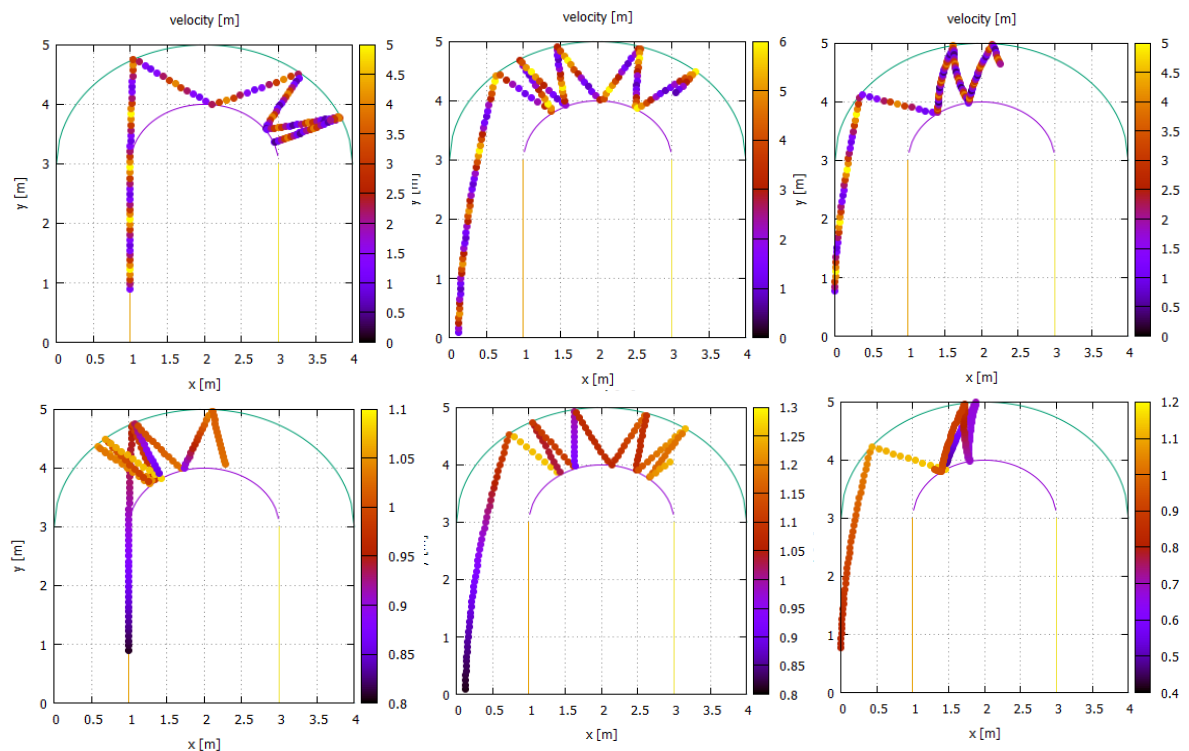


Figure 5-11. Checking angle refraction for a particle interaction in a curved channel plan view with gravity presence (upper row), and gravity absence (lower row)

Above in figure 5.15, colors represent velocity vector magnitudes. Each particle moves and refracts following Snell's law where refraction angle is equal to incident angle, in plan view. However, in 3D view and vertical direction as seen in figure 5.16, particles move as hopping bugs. This happened because gravity force is more than 100 times larger than other forces namely, pressure force, viscosity force, and surface tension force. Before a particle moves in x - or y -direction, it has already pulled down in a parabolic movement. Afterwards, we neglected gravity force in order to see how particles flow behave. Hopping bugs movement is no longer exist but particles move toward with positive value in x -, y -, and z -direction. Positive value of accelerations come from positive value of forces.

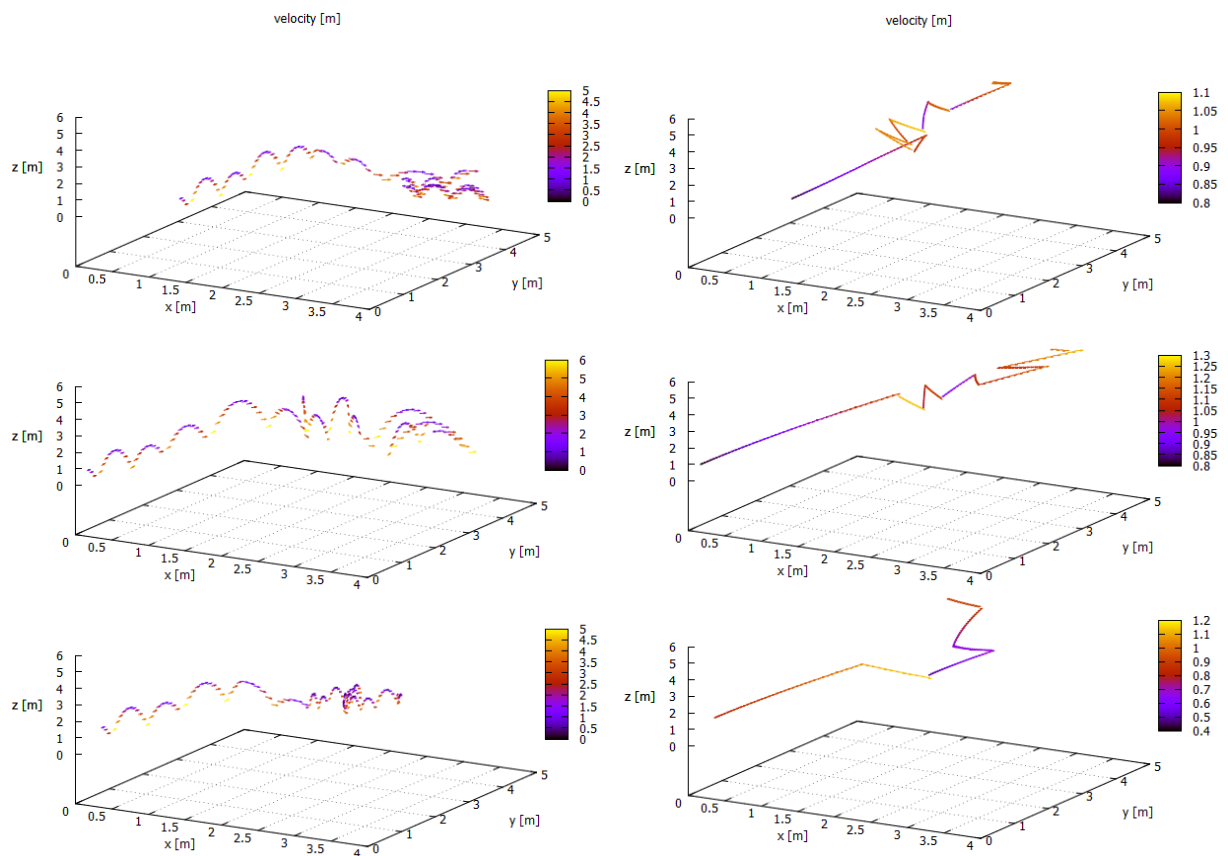


Figure 5-12. Angle refraction for a particle interaction in a curved channel 3D view with gravity presence (left), and gravity absence (right)

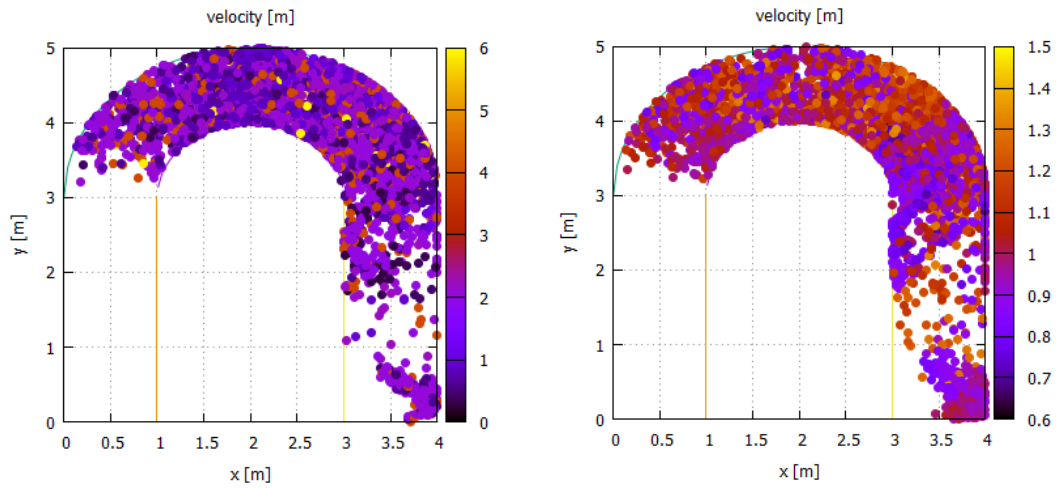


Figure 5-13. Transient inviscid flow simulation at $t = 15$ s in a curved channel plan view with gravity presence (left), and gravity absence (right)

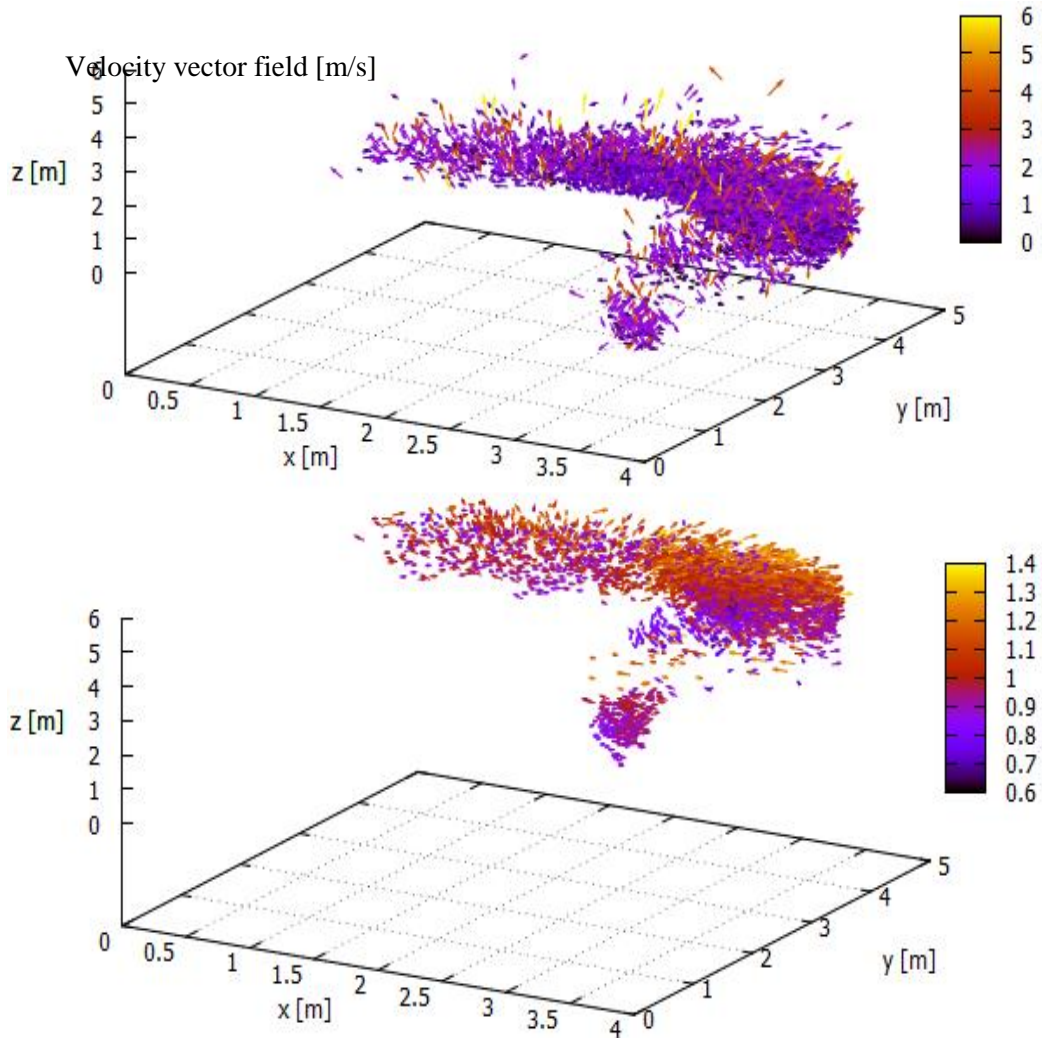


Figure 5-14. Transient inviscid flow simulation at $t = 15$ s in a curved channel 3D view with gravity presence (upper), and gravity absence (lower)

In momentum equation if gravity force is set as zero, thus it remains pressure force, viscosity force, and surface tension force. Positive pressure force expands fluid particles outward. Positive viscosity force moves fluid particles upward since velocity gradient is positive. Surface tension force limits fluid expansion, it keeps distance among particles close enough to stay intact.

5.2.4.2 Viscous Flow

Particles have initial viscous velocity. Velocity profile is in parabolic shape in x - and z -direction, where maximum velocity $v_{y_{max}}$ is caused by viscosity μ and energy slope S_o (Potter, et al., 2012) and (Wilkes, et al., 2006).

$$v_{y_{max}} = \left(\frac{1}{2 * \mu}\right) * S_o * (d^2 - x^2) \text{ where } S_o = 0.01 \quad (5.27)$$

$$v_{y_o}(x, z) = \left(v_{y_{max}} * \left(1 - \left(\frac{(x-d)^2}{d^2}\right)\right)\right) + \left(v_{y_{max}} * \left(1 - \left(\frac{(z-h)^2}{h^2}\right)\right)\right) \text{ where } d = 0.5 \text{ meter, and } h = 0.667 \text{ meter} \quad (5.28)$$

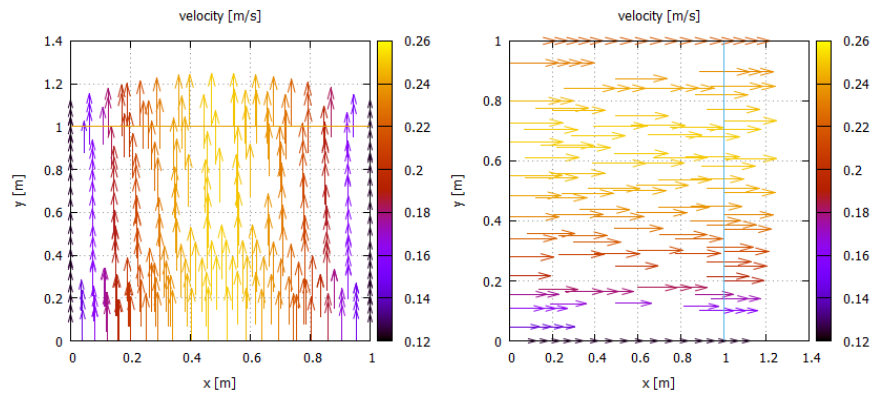


Figure 5-15. Viscous velocity profile (left) at $z = 0.667$ meter, (right) at $x = 0.50$ meter

Whenever using 4811 particle numbers, flow simulation may behaves differently rather than water flow. Therefore, we adjust viscosity from 0.001007 into 0.01 pa.s.

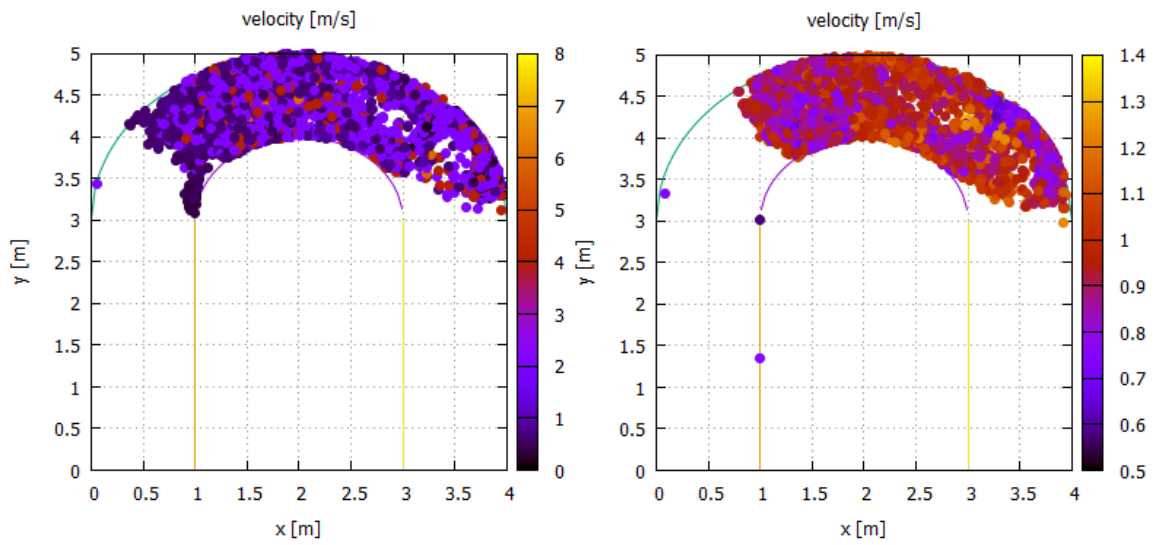


Figure 5-16. Transient viscous flow simulation at $t = 15$ s in a curved channel plan view with gravity (left) presence, and (right) absence

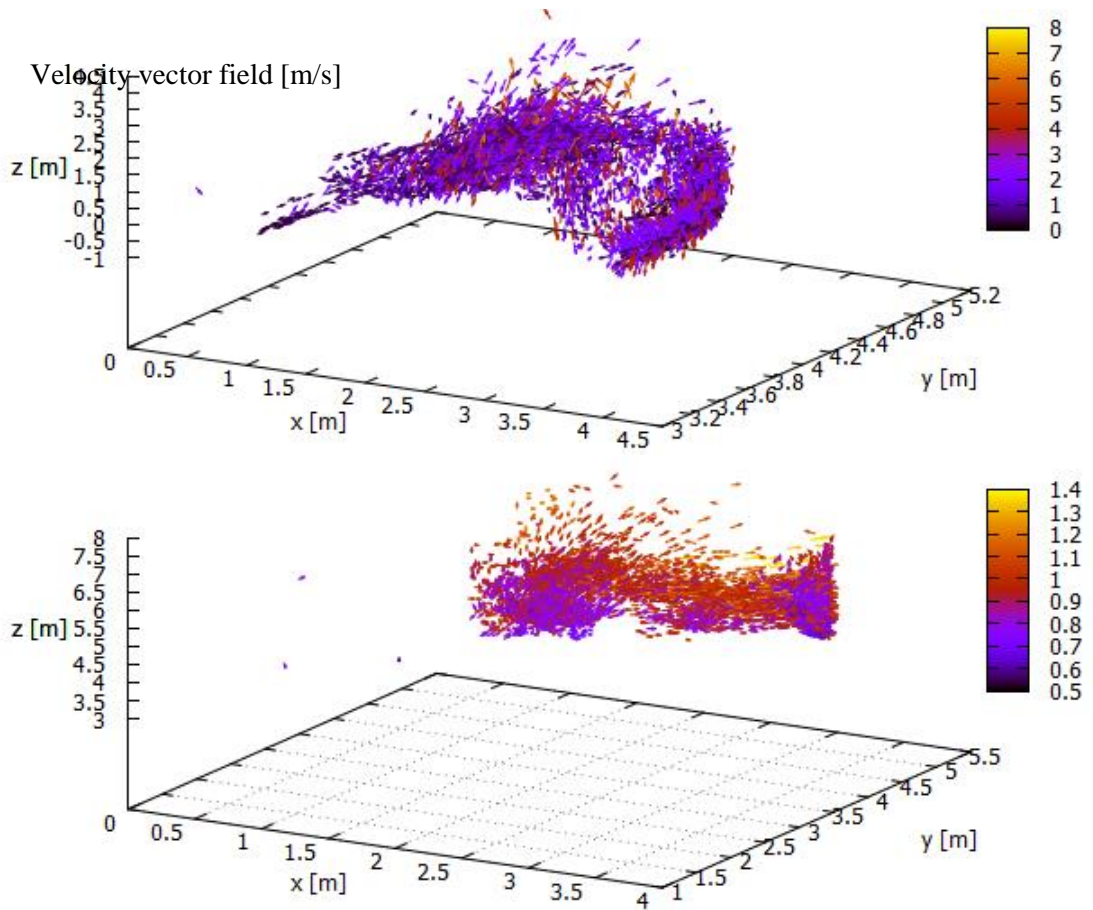


Figure 5-17. Transient viscous flow simulation at $t = 15$ s in a curved channel 3D view with gravity (upper) presence, and (lower) absence

5.2.4.3 Vorticity

In order to invoke helical movement in curved channel, vorticity is added at initial velocity.

$$v_{xo}(z) = cz * z - bz \text{ where } cz = 1 \text{ and } bz = 0.5 \quad (5.29)$$

$$v_{zo}(x) = bx - cx * x \text{ where } cx = 1 \text{ and } bx = 0.5 \quad (5.30)$$

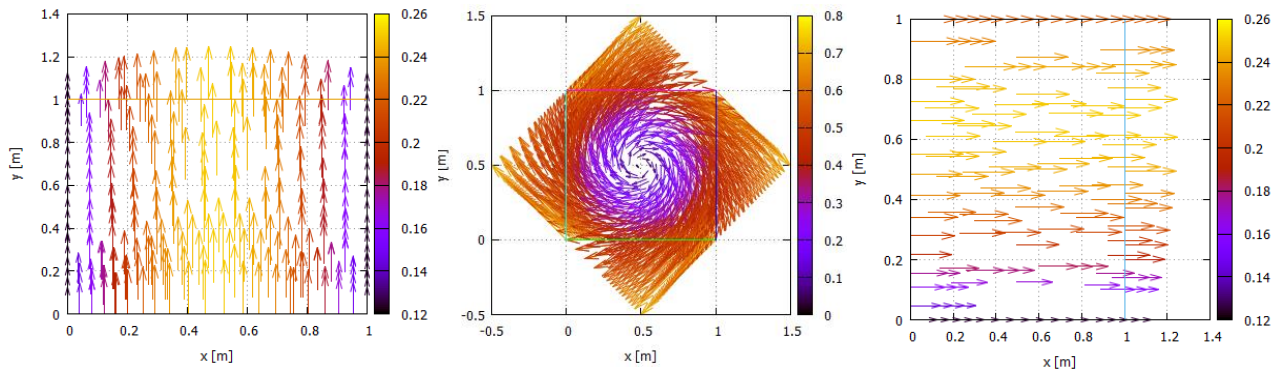


Figure 5-18. Viscous velocity profile in [m/s] (left) at $z = 0.667$ meter, (middle) $y = 0.5$ meter, and (right) at $x = 0.50$ meter

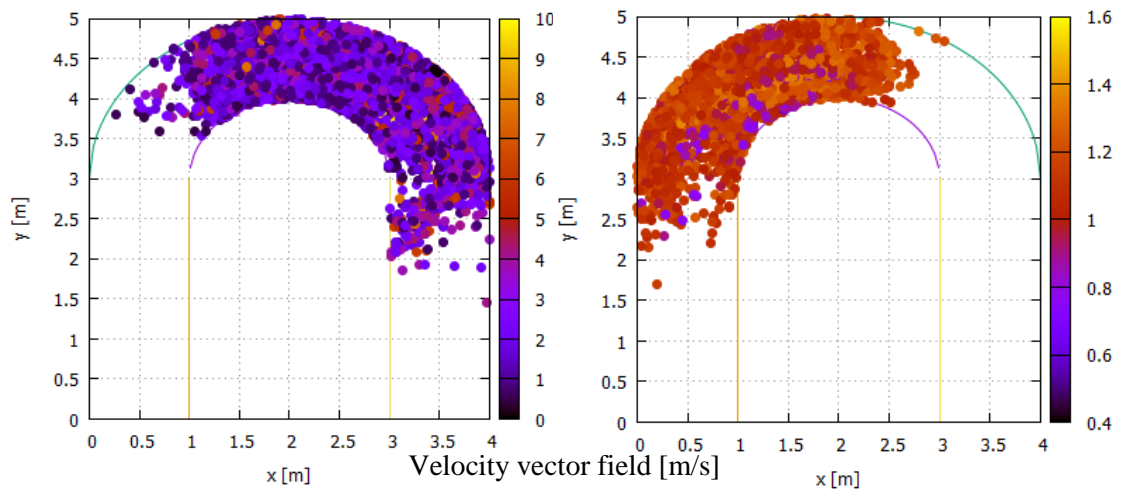


Figure 5-19. Transient viscous vorticity flow simulation at $t = 15$ s in a curved channel plan view with gravity (left) presence, and (right) absence

Vorticity strength is expressed by cz and cx constants, whereas vorticity center position bz and bx constants. The stronger vorticity at initial is the stronger particles collision to the walls, as consequence particles flow might be immovable. Therefore, we chose $cx = cz = 1$. Since initial particles positions are placed in 1

meter length and 1 meter height, then the vorticity center constants in z - and x -directions are $b_x = b_z = 0.5$ meter.

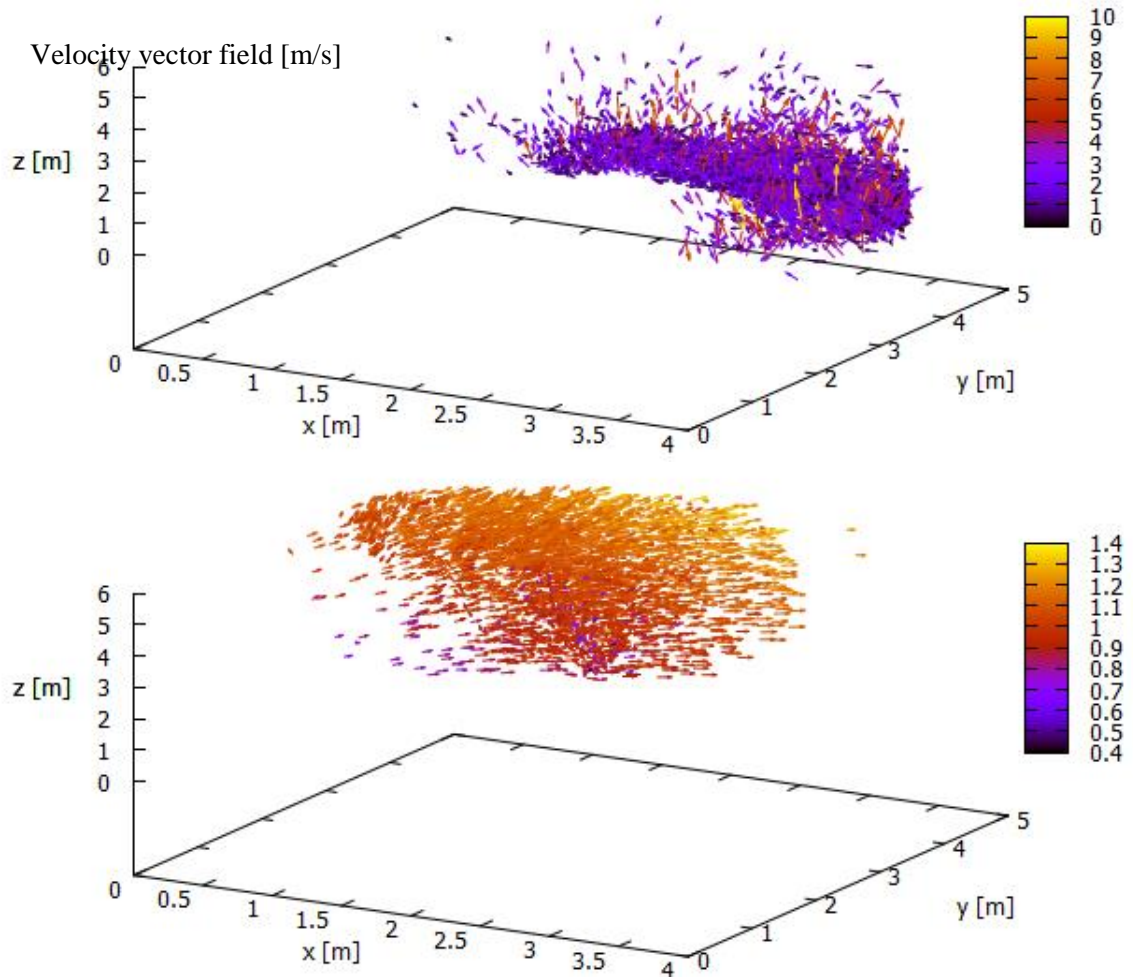


Figure 5-20. Transient viscous vorticity flow simulation at $t = 15$ s in a curved channel 3D view with gravity (upper) presence, and (lower) absence

5.2.4.4 The effect of fluid properties

We run flow simulations into cases based on the variation of vorticity, mass, viscosity, gravity, and surface tension. First simulation type, we varied gravity magnitude into 1% g . For all simulation types, we consider the occurrence of vorticity at initial conditions. Second type simulation, with the purpose to balance gravity force magnitude, we altered fluid properties such the value of viscosity for viscosity force, rest density and mass for pressure force, and surface tension for surface tension force.

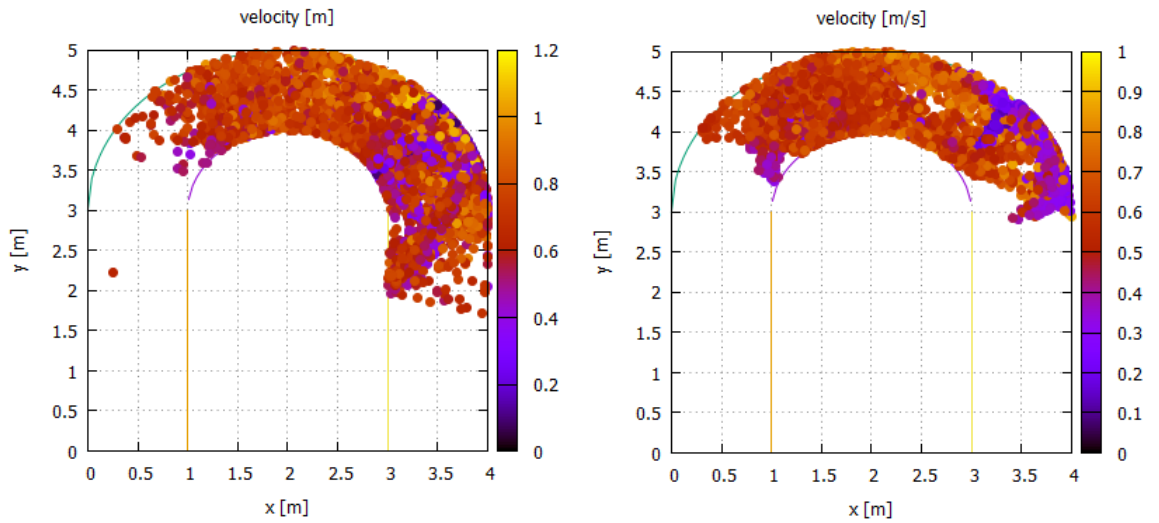


Figure 5-21. Flow simulation with 1% of gravity magnitude in plan view (left) with vorticity, and (right) without vorticity

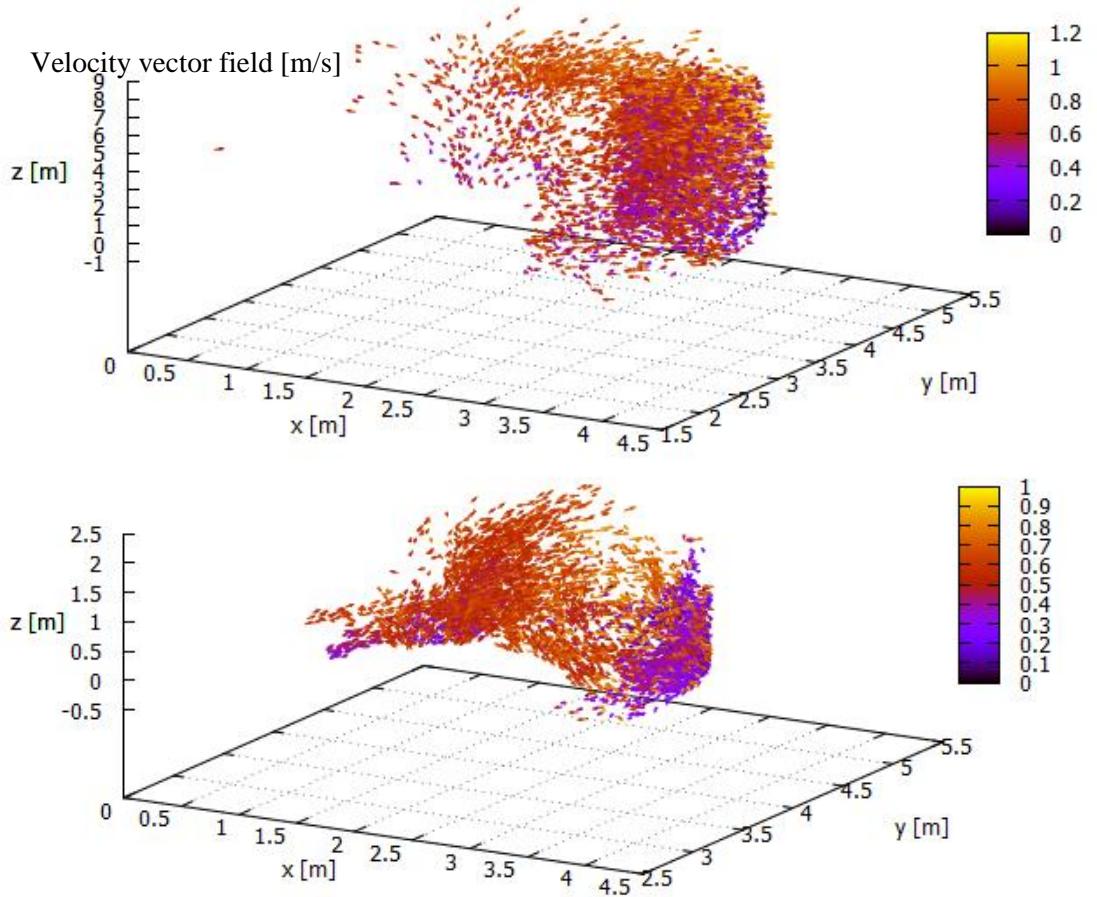


Figure 5-22. Flow simulation with 1% of gravity magnitude in 3D view (upper) with vorticity, and (lower) without vorticity

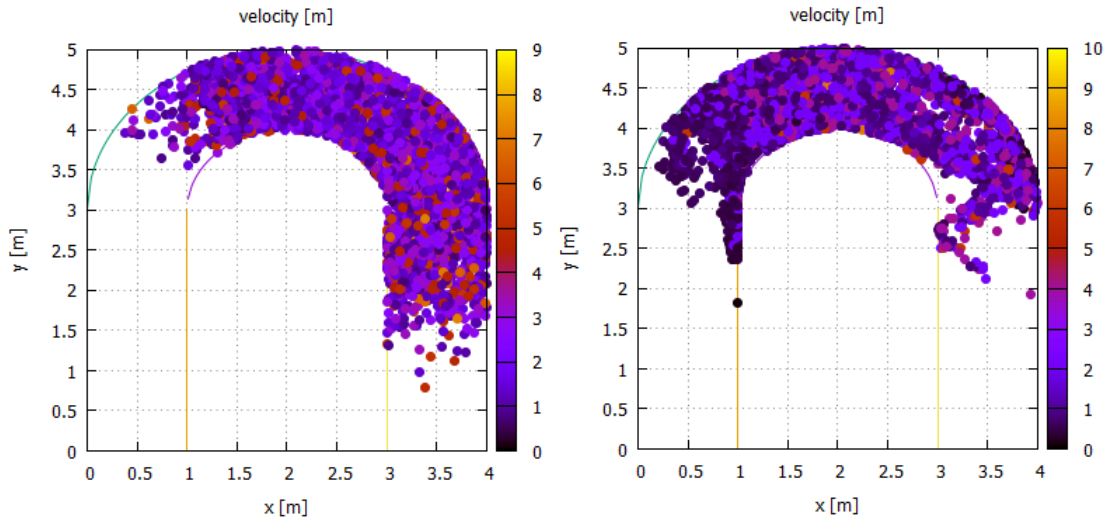


Figure 5-23. Flow simulation with 100 times of viscosity, mass, and surface tension magnitude in plan view (left) with vorticity, and (right) without vorticity

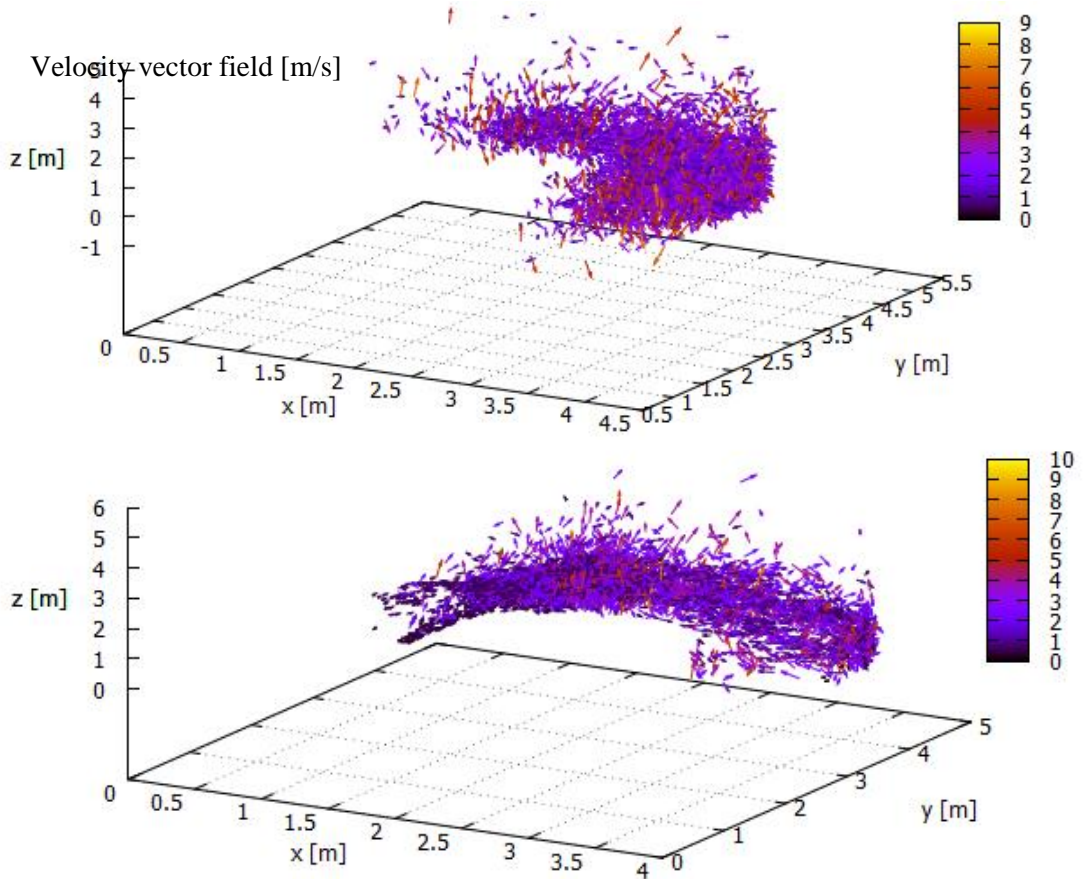


Figure 5-24. Flow simulation with 100 times of viscosity, mass, and surface tension magnitude in 3D view (left) with vorticity, and (right) without vorticity

5.3 RESULTS DISCUSSION

SPH program run water simulations in a curved channel for inviscid, viscous flow, vorticity, mass, viscosity, gravity, and surface tension. Results is presented in Figure 5-25 where particles flow act like fluid flow. Simulation run from zero to fifteen seconds. Initial condition is inviscid flow where $v_{y0} = 0.8$ m/s. At first in straight channel, particles move straight forward. When they enter in the curved part, they collide and turn directions as caused by collisions with curved walls. The collisions transfer momentum from outer to inner curved wall, then bounce back, and keep rebounding until they exit the curved part.

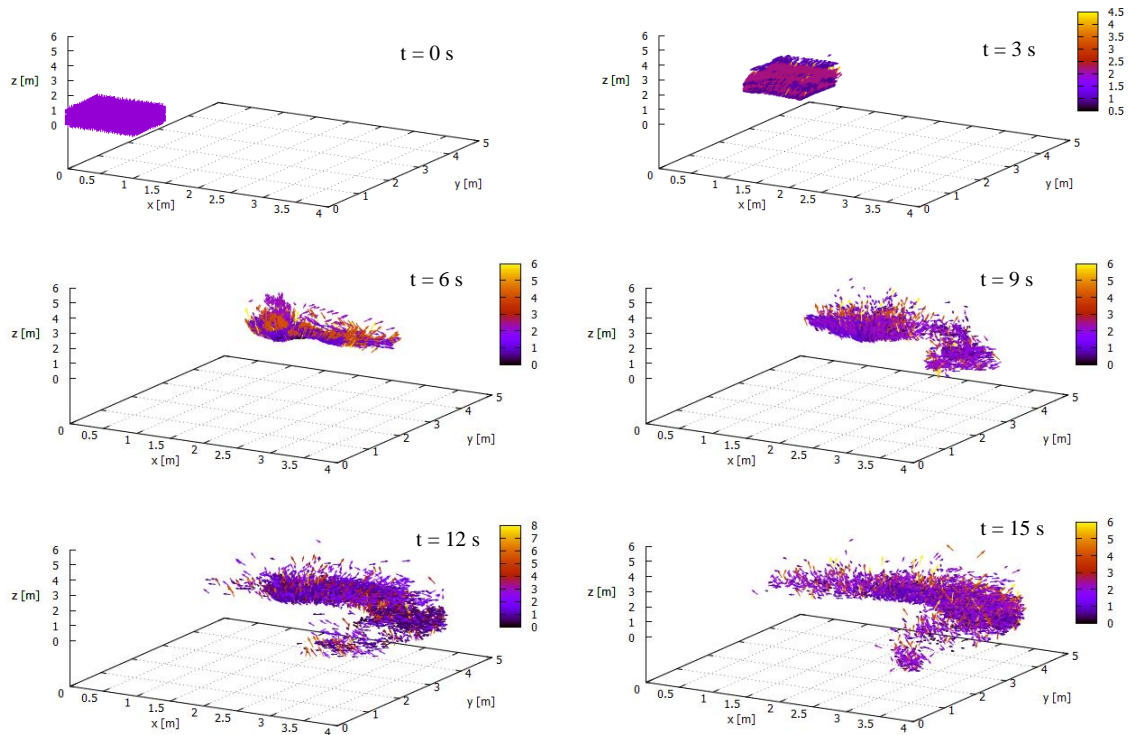


Figure 5-25. Particle flows with water properties from $t = 0, 3, 6, 9, 12,$ and 15 second (from upper left in clockwise direction); colors represent velocity [m/s]

This pattern may appear as helical but if we look closely to a particle flow path, the refraction angle is too sharp, as in Figure 5-11. This can be happened due to collision handling method. At this time, the contact between particle and boundary is governed by Snell's law.

Figure 5-26 shows a particle flow path that run from 0 to 15 seconds from the simulation in preceding Figure 5-25. The pattern is quite satisfactory in a plan view, but in 3D view we see a hooping bug movement or a particle jumping in vertical direction in upper left Figure 5-26. This is happened because the magnitude of gravity force is rather dominant than pressure force, viscosity force, and surface tension force. The ratio of gravity force to other force ranges between 100 to 150 times bigger.

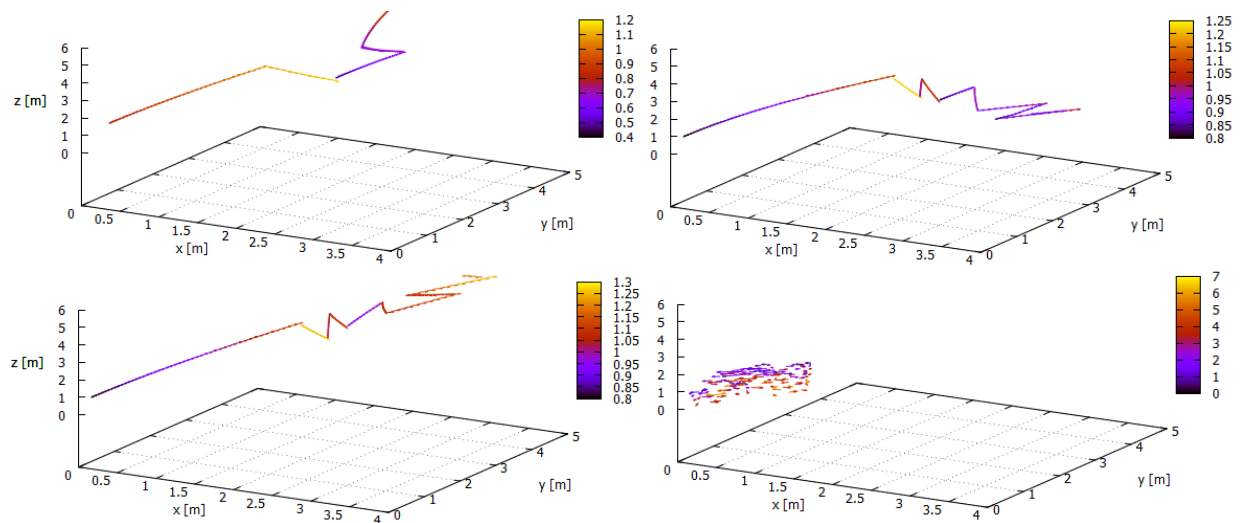


Figure 5-26. Particles collision handling (upper left) with gravity, (upper right) with 1% * gravity, (lower left) without gravity, and (lower right) with 10% mass; colors represent velocity [m/s]

In order to solve the jumping particles movement, the main parameters in vertical forces are gravity and particle mass, and these will be varied. Firstly, we reduce the gravity acceleration into 1% of its magnitude. Secondly, we set zero gravity, and lastly, we decrease the mass into 10% mass as displayed in Figure 5-26. In upper right figure, since we use 1% coefficient of gravity, the particle movement in time is no longer jumping. However, if we set zero gravity, the particle movement is expanding and ascending towards the initial location as in lower left figure. The last one, we reduce the mass into 10%, the particle moves randomly without any pattern as in lower right figure.

We can conclude that flow simulation using water properties develops velocity predominantly governed by gravity. Despite the fact, as discussed in previous sub-sub-chapter 5.2.4 above, we have settled that all parameter magnitudes is within sensitivity range and none is dominant. Consequently, a question emerges why the magnitude is imbalanced between gravity forces with other forces. Therefore, we need to consider the effect of gravity magnitude, and each fluid properties that is employed in momentum equation. We run eight cases of for water flow simulation, as in Table 5.2 below.

All cases are run with 1% as a coefficient for gravity magnitude and water properties, except for case number 6. Cases number 1, 2, 3, and 4 are inviscid water flow simulations. In these cases, particles are still behaving like 2D case as discussed along with Figure 5-25 and Figure 5-26 above. As follows, particles are simulated with initial viscous flow, vorticity, and vorticity viscous flow.

Table 5.2. Simulation Cases

Case #	Properties	vxo	vyo	vzo	rest density	mass	viscosity	gravity	surface tension	Remarks
1	gravity, inviscid	0	Constant	0	1000	0.9622	0.001007	9.819	0.0736	Particle jumping due to gravity and particle mass. Magnitude of gravity and mass will be varied.
2	1% gravity, inviscid	0	Constant	0	1000	0.9622	0.001007	1%*9.819	0.0736	No longer jumping particle with 1% gravity, or zero gravity, or 10% mass. But, still no helical flow.
3	zero gravity, inviscid	0	Constant	0	1000	0.9622	0.001007	0	0.0736	
4	gravity, inviscid, 10% mass	0	Constant	0	1000	9.62E-02	0.001007	9.819	0.0736	Initial viscous flow, and/or vorticity will be given, but using only 1% gravity and back to 100% mass.

Case #	Properties	vxo	vyo	vzo	rest density	mass	viscosity	gravity	surface tension	Remarks
5	1% gravity, viscous	0	Parabolic	0	1000	0.9622	0.001007	1%*9.819	0.0736	Not yet helical, but secondary flow start to form.
6	1% gravity, viscous, 1000% viscosity	0	Parabolic	0	1000	0.9622	0.01	1%*9.819	7.36	
7	1% gravity, vorticity	y	Constant	y	1000	0.9622	0.001007	1%*9.819	0.0736	No secondary flow, helical movement only occurs before entering hemisphere
8	1% gravity, viscous vorticity	y	Parabolic	y	1000	0.9622	0.001007	1%*9.819	0.0736	There is secondary flow, helical start to form after leaving hemisphere

Case number 5 is water flow simulation with initial viscous flow in y-direction. Case number 6 is the same with case number 5 simulation, but only its viscosity value is 10 times bigger. Bigger viscosity value only makes slower movement but do not give much effect in the developing on helical flow. Flow simulations in case number 5 and 6 do not yet produce helical movement, but the secondary flow starts to form after particles outflow from hemispheres part of the curved channel, as drawn in Figure 5-32.

With the intention of generating helical movement, particles simulation includes vorticity at initial condition. Case number 7 is water flow simulation with initial vorticity in x- and z-directions. The helical movement appears but only lasted before entering the hemispheres. After that, particles move under collision handling and then get stuck in the middle of the hemispheres. Particles hardly move forward. This may be happened because there is no viscous effect. Frictions between particles and the walls are bigger than the forces to move forward. Nonetheless, the secondary flow start to develop in the hemispheres, we can see

in Figure 5-30 some of the velocity vectors are making alternate movement due to the main flow.

Thus, in case number 8, water flow simulation incorporates a combination of initial vorticity and viscous flow. In Figure 5-36, secondary flow starts to build in the hemisphere but helical movement is not yet created. Nevertheless, as represented in Figure 5-36, helical flow begins to develop at the downstream of the hemispheres. Even though, it is not yet in a full circular shape but helical flow is initiated.

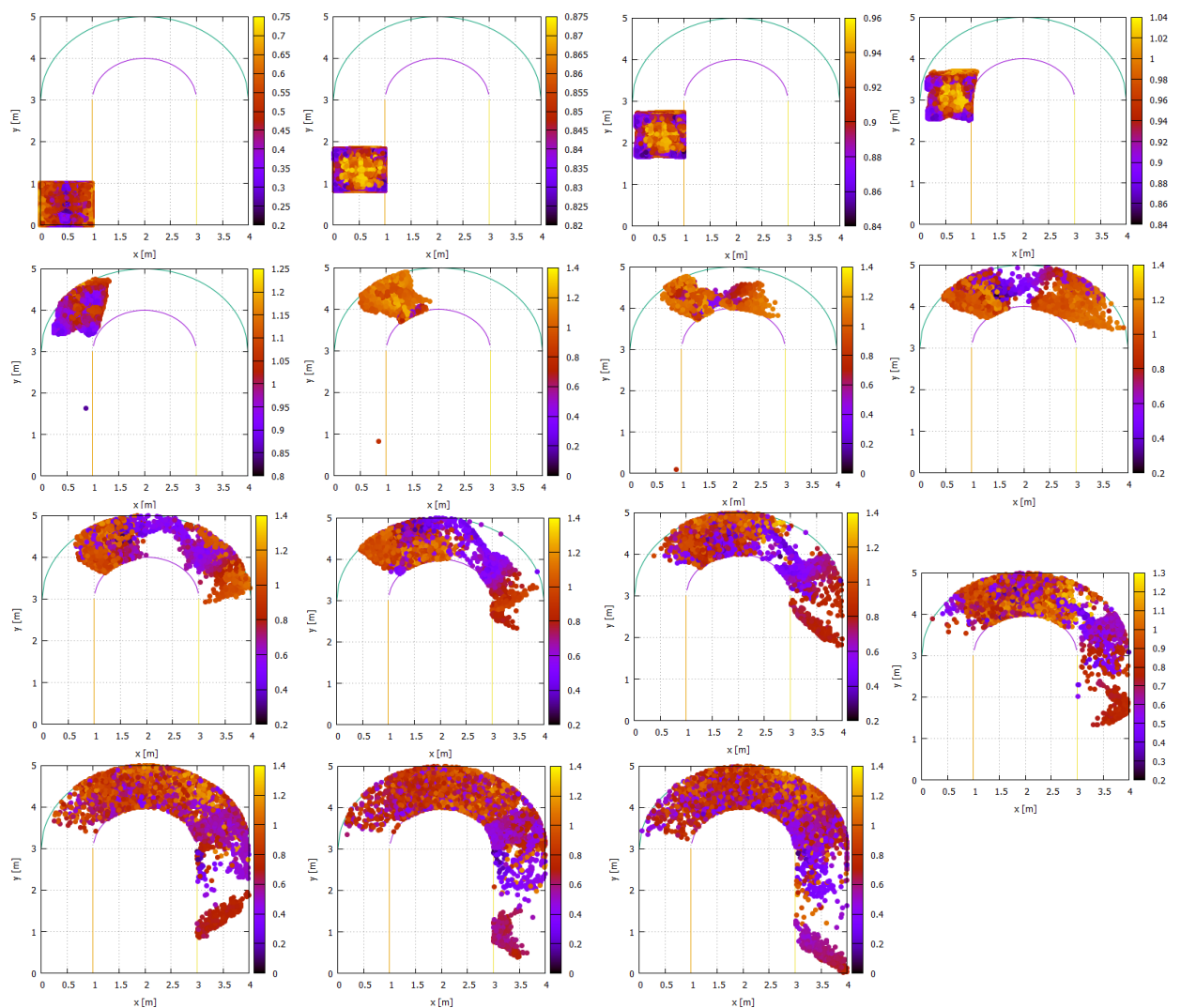


Figure 5-27. Particles collision handling in curved channel with 1% gravity, initial inviscid flow, time 14 seconds in 3D view, time step 1 s, each color represents velocity [m/s]

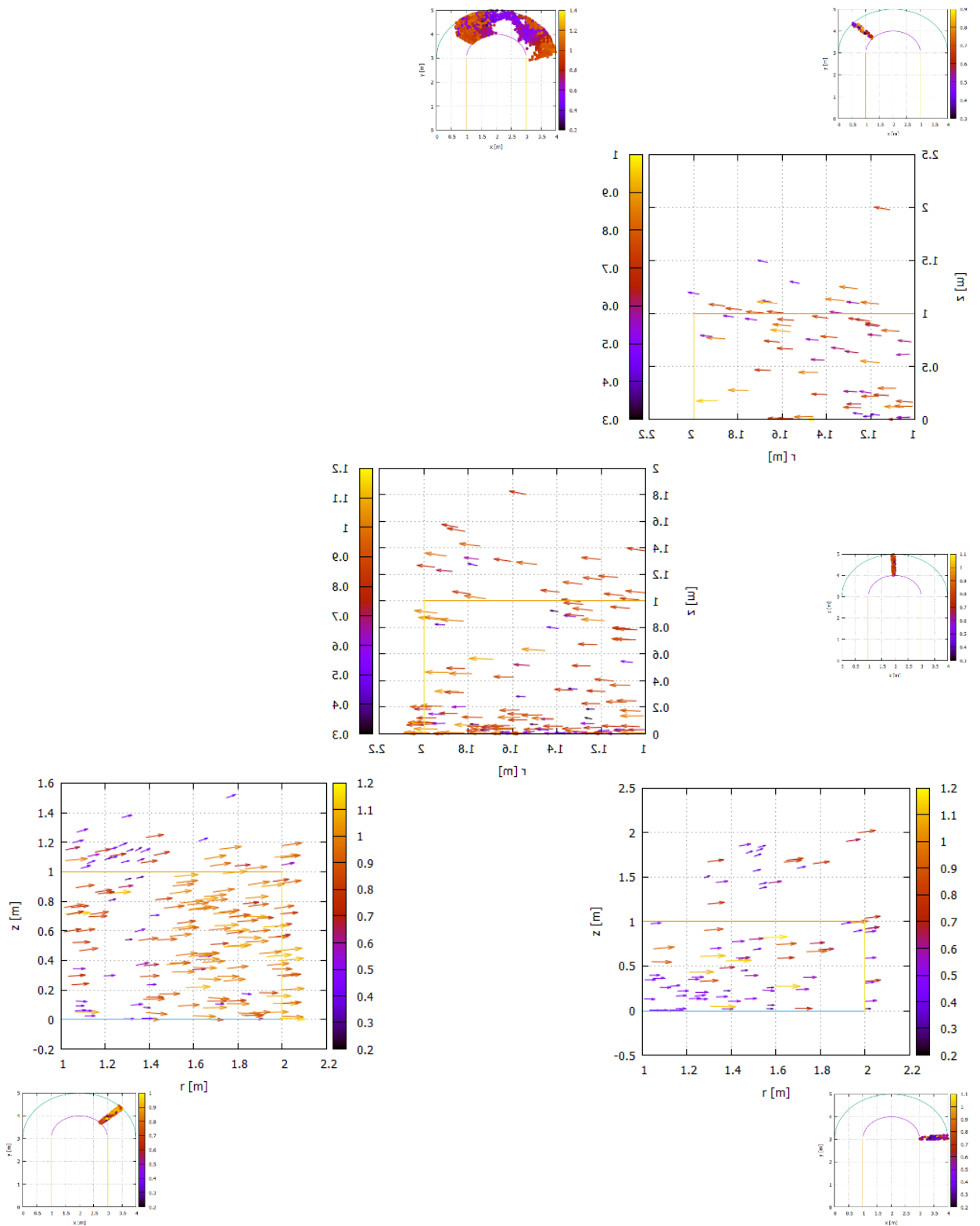


Figure 5-28. Particles collision handling in curved channel with 1% gravity, initial inviscid flow, time 14 seconds for cross sections at the hemispheres

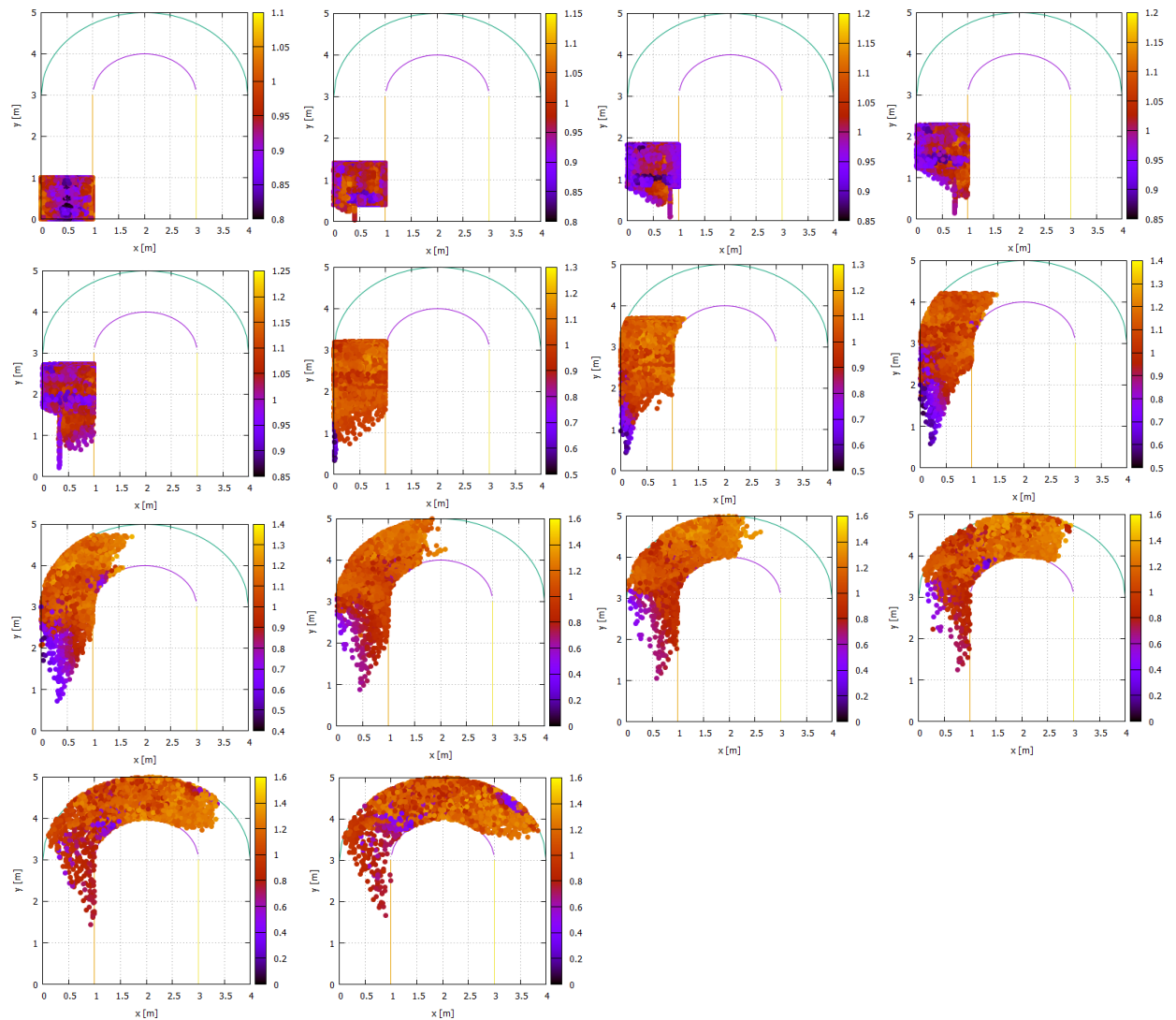


Figure 5-29. Particles collision handling in curved channel with 1% gravity, initial vorticity flow, time 6.5 seconds in 3D view, time step 0.5 s, each color represents velocity [m/s]

Figure 5-27 above shows particles movement with initial inviscid flow in 14 seconds and time step 1 second. Particles move straightly forward in 4 seconds and start to collide with hemisphere walls for the next 5 seconds. Particles cubicle formation starts to break in seventh second, and tries to initiate a swirl but fails. Particles keep zigzagging towards downstream until fourteenth second.

Figure 5-28 above gives particles movement in cross section at the hemispheres. However, it shows that particles move outward as caused by centripetal forces but there is not a helical movement.

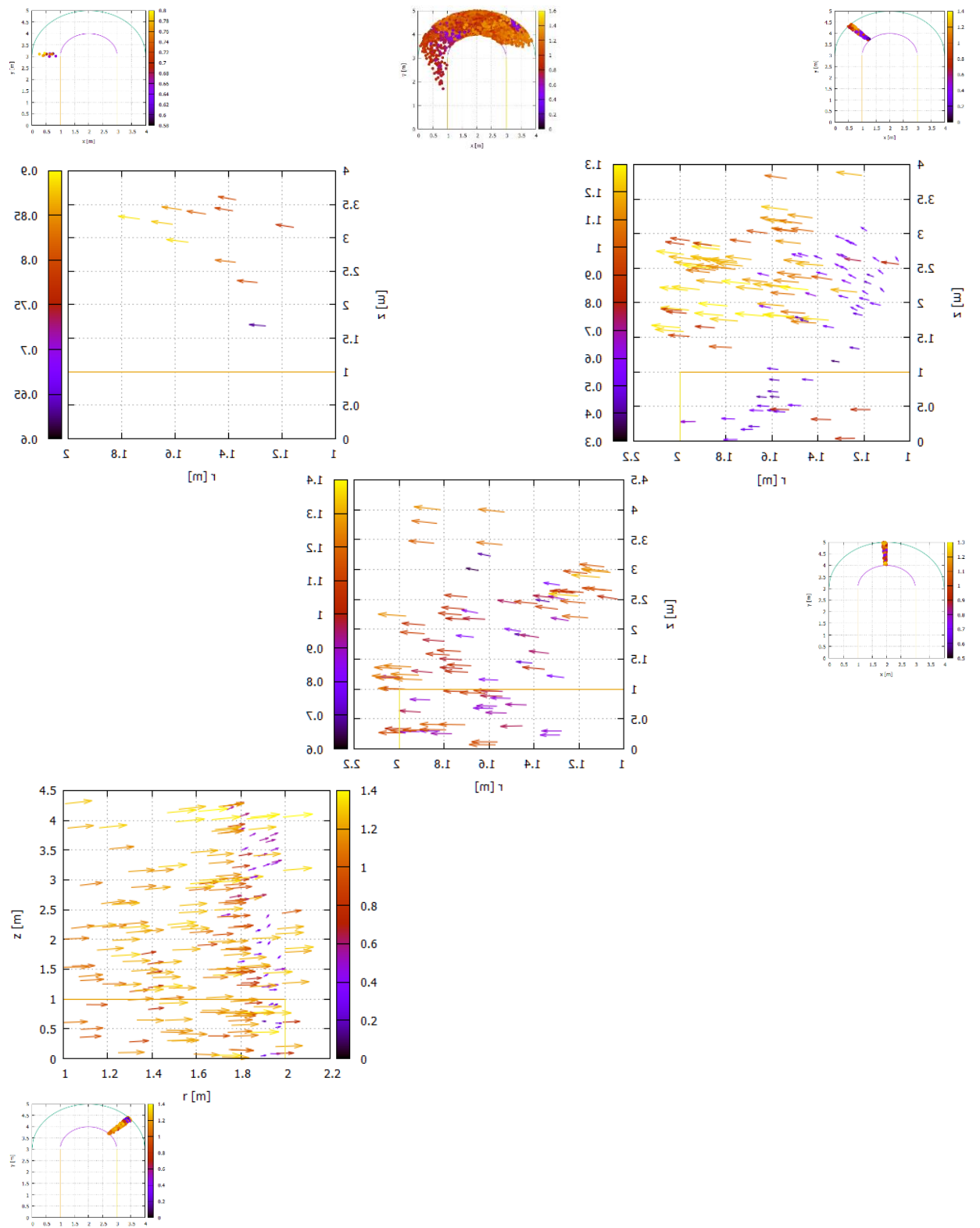


Figure 5-30. Particles collision handling in curved channel with 1% gravity, initial vorticity flow, time 6.6 seconds for cross sections at the hemispheres

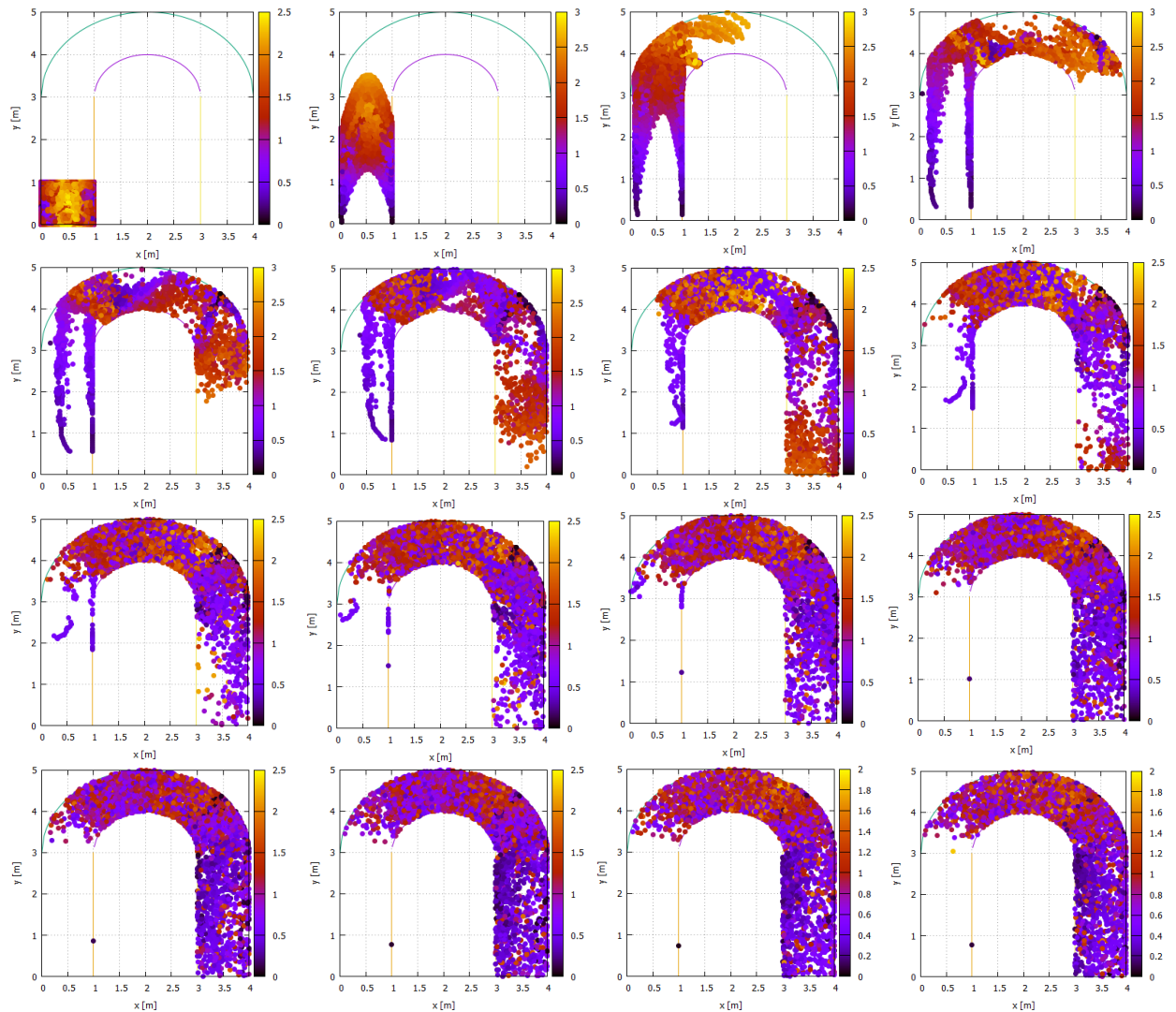


Figure 5-31. Particles collision handling with curved channel with 1% gravity, initial viscous flow, time 15 seconds in 3D view, time step 1 s, color represents velocity [m/s]

Figure 5-29 above describes particles movement with initial vorticity flow in 6.5 seconds. This simulation run faster than simulation with initial inviscid flow. Vorticity increases friction between particles and the walls thus it makes particles stuck inside the hemispheres. The simulation program stops running in middle of the computation.

Figure 5-30 above displays particles movement in cross sections at the hemispheres. At the downstream hemispheres, particles move outwards the outer hemisphere and then swirl back towards the inner hemisphere. Helical motion starts to form but unfortunately the simulation stuck there.

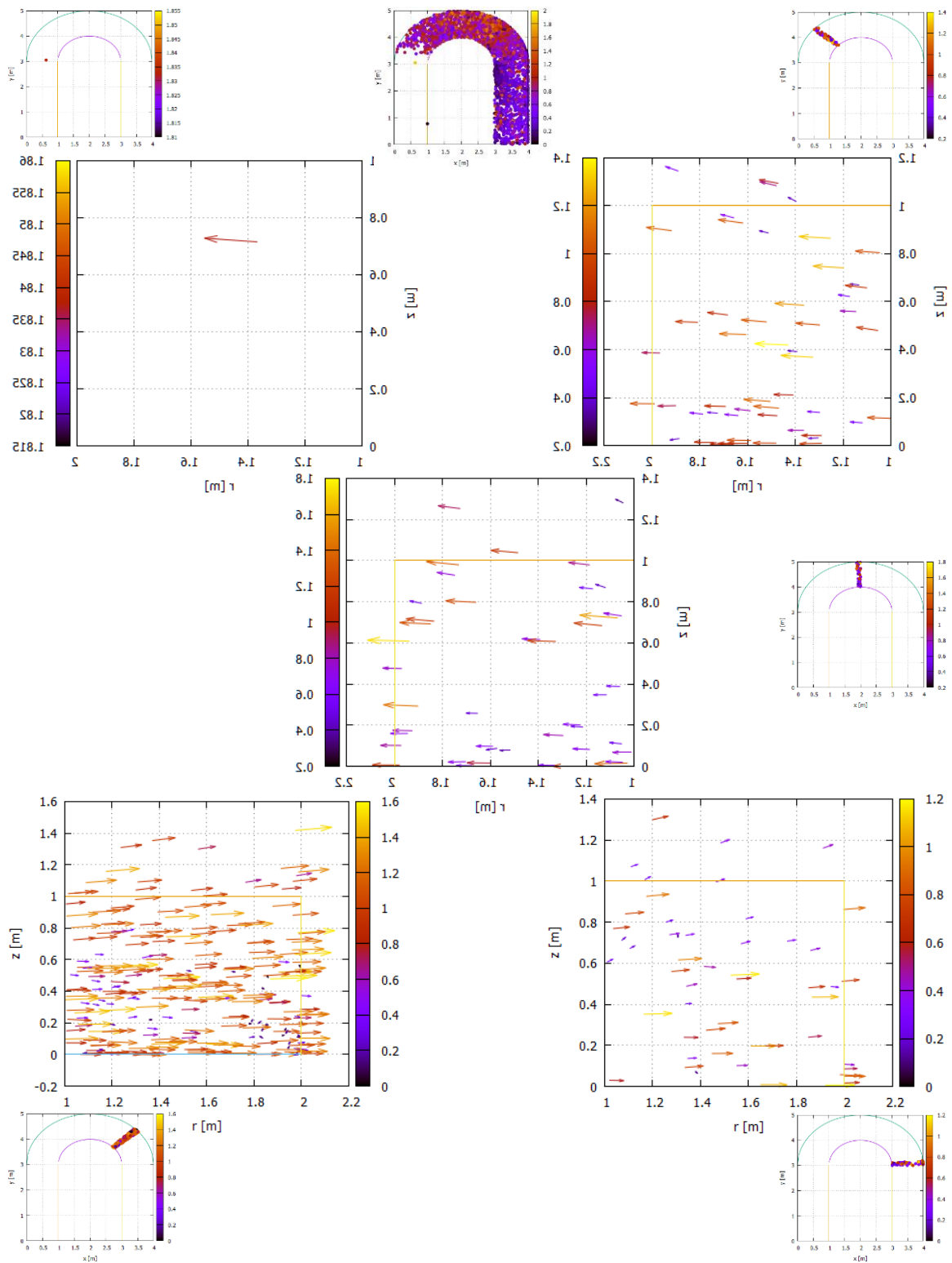


Figure 5-32. Particles collision handling with curved channel with 1% gravity, initial viscous flow, time 15 seconds for cross sections at the hemispheres

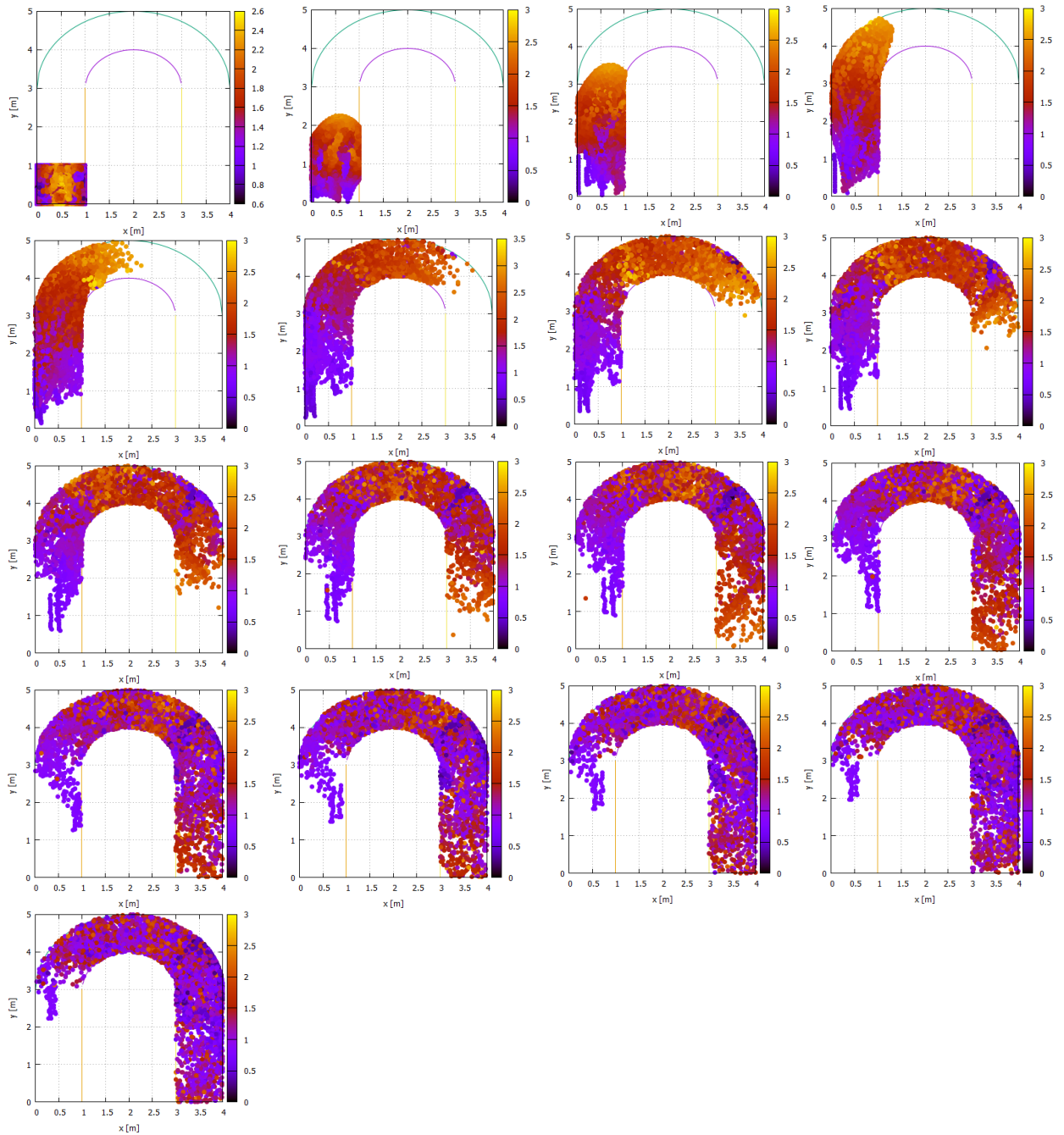


Figure 5-33. Particles collision handling with curved channel with 1% gravity, initial viscous vorticity flow, time 8 seconds in 3D view, time step 0.5 s, color represents velocity [m/s]

Figure 5-31, flow simulation uses viscous flow initially. Particles in the center of cross section move fast but particles near the walls shift slowly due to the frictions. In Figure 5-32, helical formation starts to develop but it is not noticeable enough if we compare it to the primary flow.

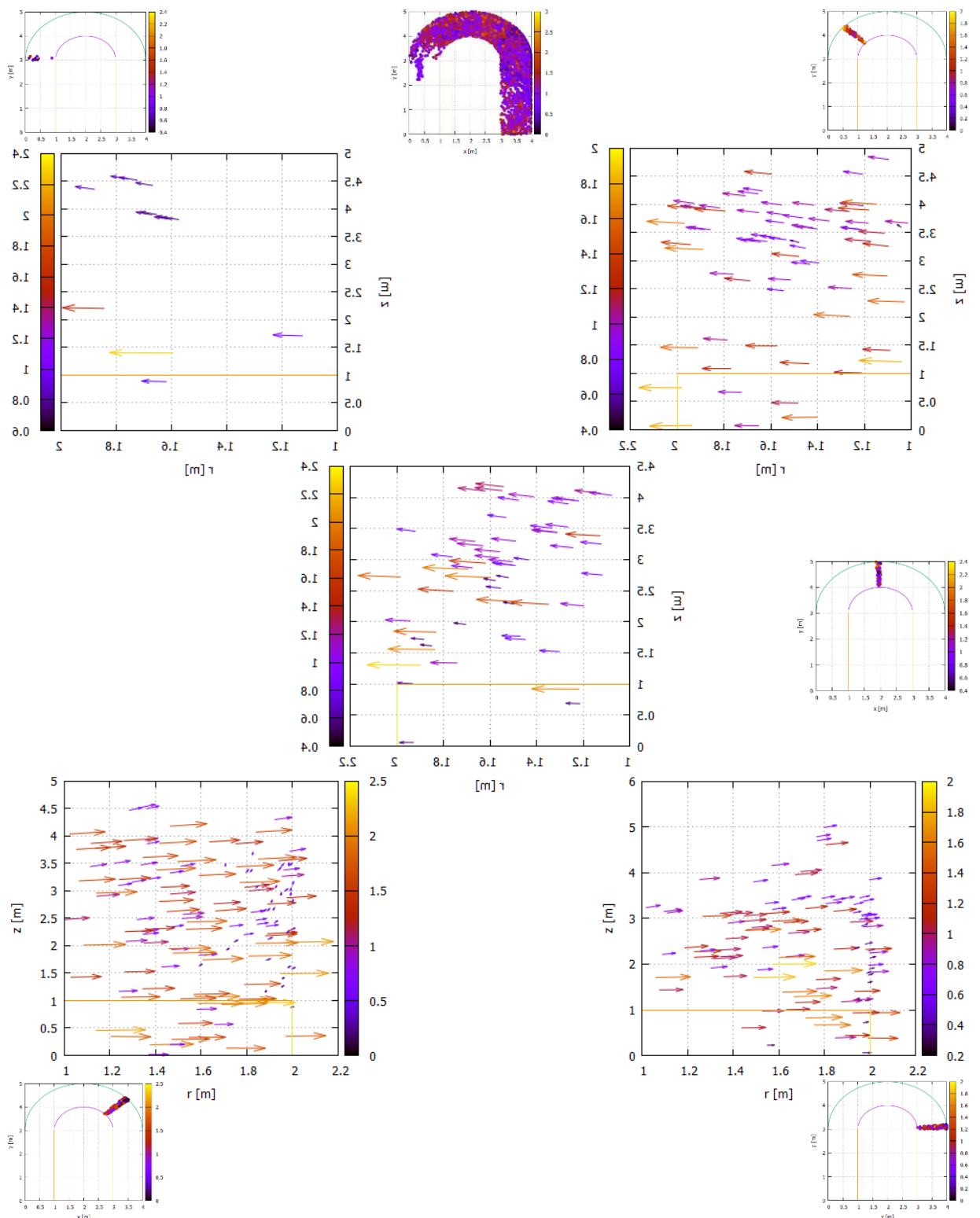


Figure 5-34. Particles collision handling with curved channel with 1% gravity, initial viscous vorticity flow, time 8 seconds for cross sections at the hemispheres

SPH simulation with initial viscous flow have shown that viscous effect plays significant role in the formation of helical flow. In order to magnify the strength of helical formation, the simulation adds both vorticity and viscous effects at initial velocities. In Figure 5-33, particles move faster, smoothly swirl through the hemisphere, and flow towards the downstream. Figure 5-34, as expected, the helical flow starts to form in the downstream of the hemispheres.

From discussion above, we just focus in the hemisphere part of curved channel. Then we look farther at the downstream of hemisphere.

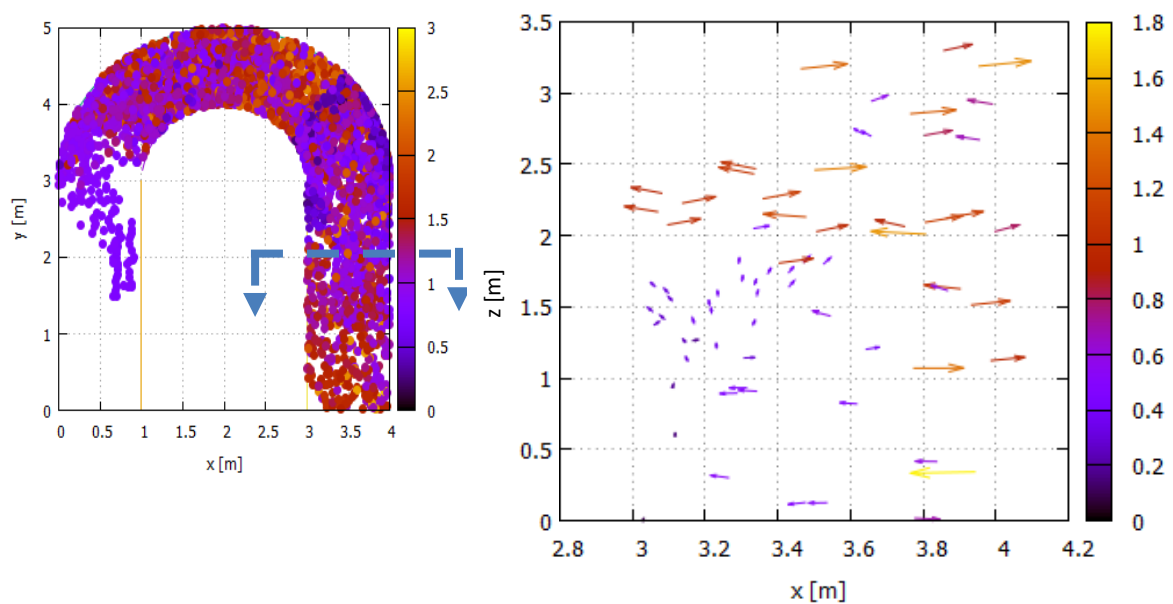


Figure 5-35. Helical formation with initial vorticity viscous flow simulation at $t = 6.5$ seconds; colors represent velocity [m/s]

Helical flow is formed after water flows exit the hemisphere of Figure 5-33, and more clearly in Figure 5-35. Some particles move from channel bottom towards outer wall then they swirl up backward against outer wall. This motion initiates helical flow. We may improve the helical shape by varying magnitudes of initial vorticity and viscous flow.

5.3.1 RESULTS COMPARISON

Wang and Liu (2015) describe their findings from experimental investigation of flow structures in a bend flume. We will use this experimental results to compare with SPH results and RMA results for verification. We adjust

the channel geometry in SPH with respect to their experimental set up. Width channel is 0.30 meter, initial depth is set at 0.16 meter, center coordinate of the hemispheres is (0.80, 0.80, z) meters, inner hemisphere radius is 0.50 meter, and outer hemisphere radius is 0.80 meter.

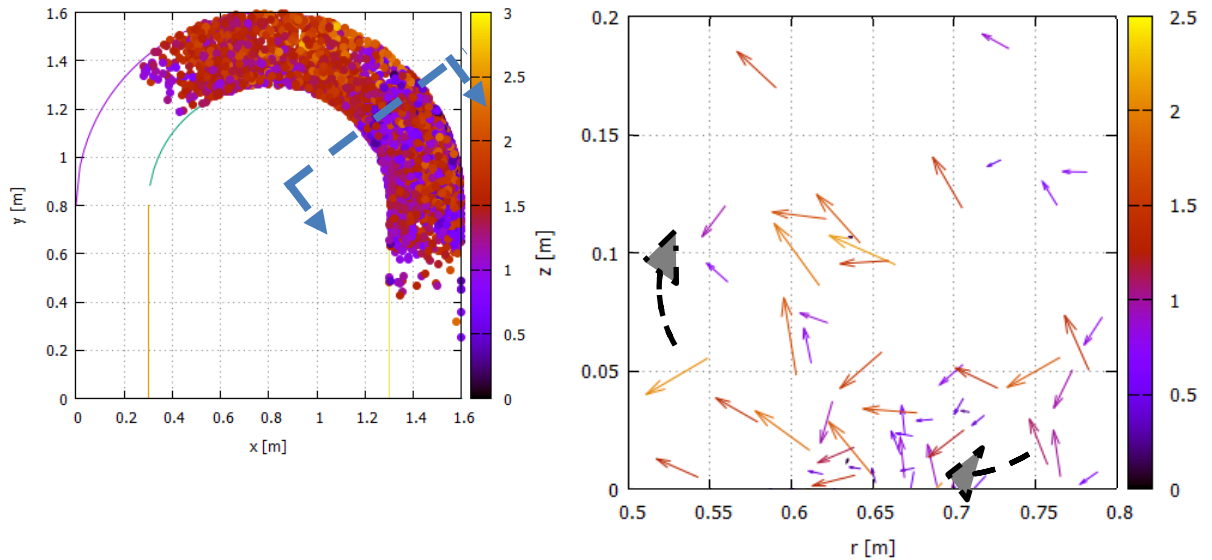


Figure 5-36. Helical formation with SPH simulation, initial vorticity viscous flow, and results at $t = 2.35$ seconds; colors represent velocity [m/s]

At first, when we used coefficient gravity, particles were flowing and expanding like gas. At the cross section intended in Figure 5-36, depth of particles flow became 11 meter instead of 0.2 meter. It was because the gravity force was too weak due to the coefficient we set at the equation. Then, we took coefficient out from the gravity force equation. Afterwards, particles behave like water as in Figure 5-37 where the average depth is less than 0.2 meter, its velocity range close range between 0.50 m/s and 2.50 m/s. Particles start to move in helical formation though it is not strong. From the bottom, some particles move towards outer wall then they turn back against outer wall.

From particles calculation, at $t = 2.35$ s, average velocity is 1.29 m/s with minimum 0.04 m/s, and maximum 2.82 m/s. Average relative pressure is 0.034 Pa, with minimum 0.003 Pa and maximum 0.188 Pa. Average density is 4383.8 kg/m³, with minimum 1392.6 kg/m³ and maximum 19798.9 kg/m³. At this point, we can consider that the particles calculation behaves close to the experiment result as in Figure 5-40.

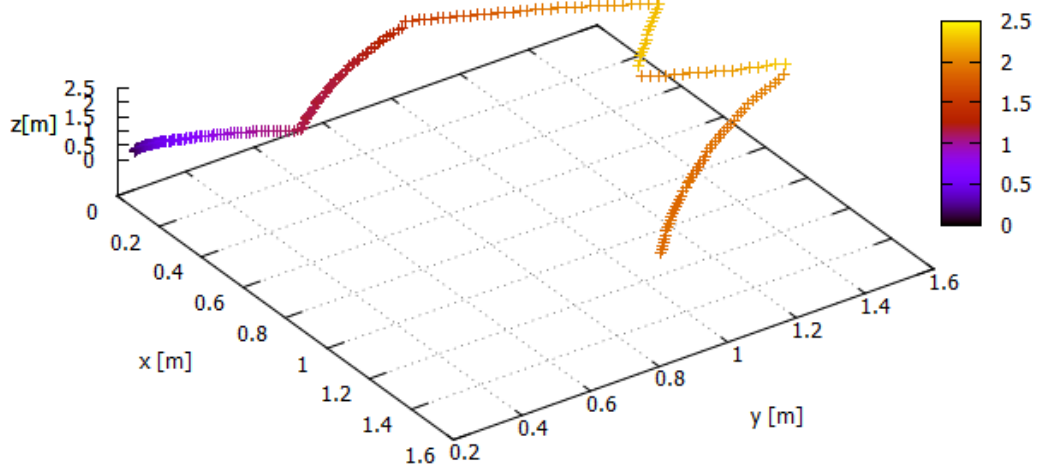


Figure 5-37. Checking angle refraction for a particle interaction; colors represent velocity [m/s]

In Figure 5-38, high pressure and high density particles coordinates are located with the same low velocity particle coordinates. This is reasonable since crowded particles push particles to its surrounding but it is limited to space. Particles movement is decelerated. Thus, particles have high pressure.

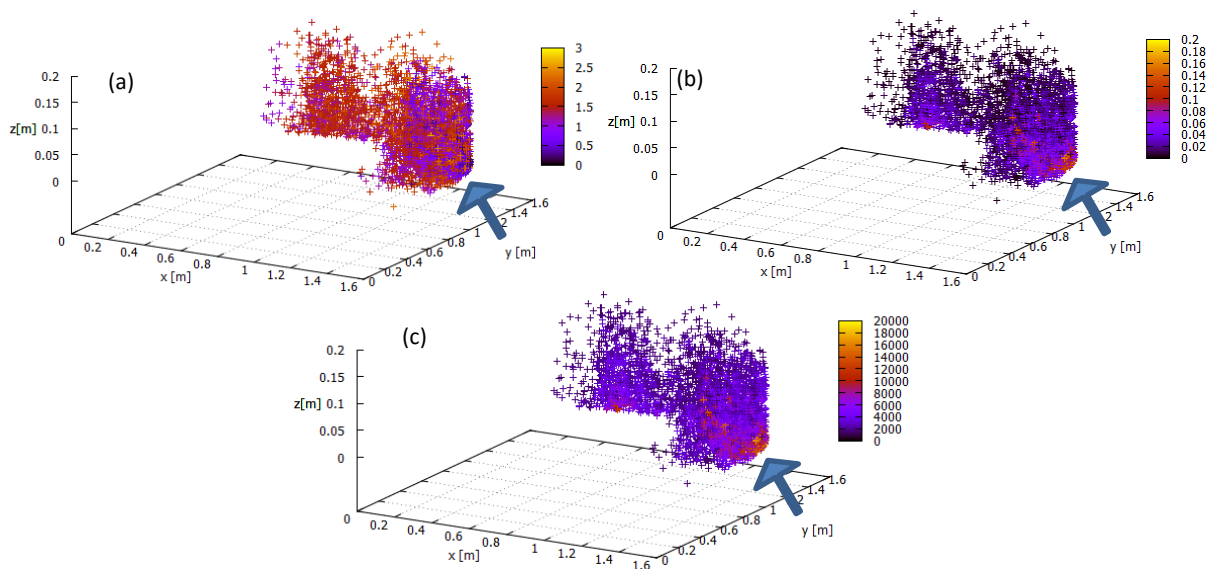


Figure 5-38. Particles value of: (a) velocity [m/s], (b) pressure [Pa], and (c) density [kg/m³]

Simulation with RMA is run with the same setting with Wang and Liu's (2015) experiments. Helical flow pattern from SPH model in Figure 5-36 has the same pattern with helical flow patterns from RMA model in Figure 5-39, and follows the pattern with the experiment results in Figure 5-40.

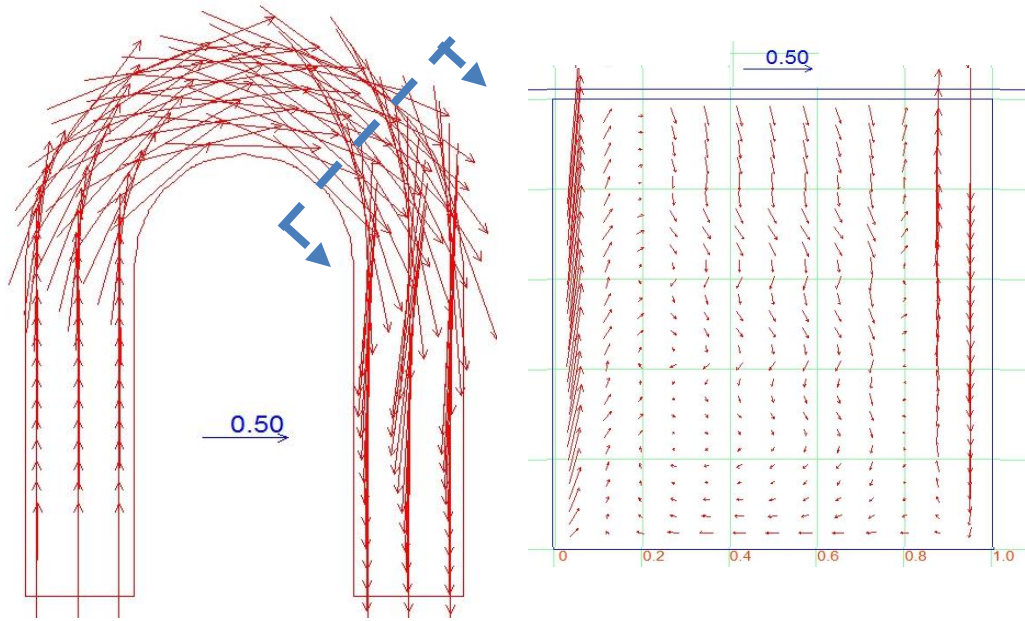


Figure 5-39. Helical formation with RMA simulation at $t = 1.5$ seconds; colors represent velocity [m/s]

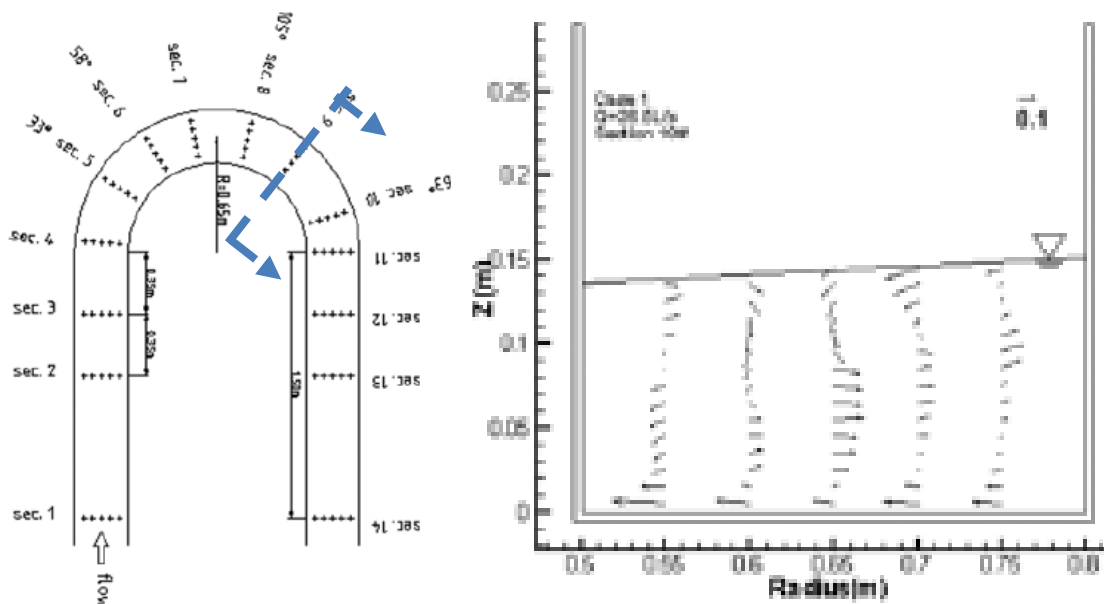


Figure 5-40. Helical formation from experiment investigation of flow structures (Wang & Liu, 2015)

Helical formation with SPH, RMA, and even in the experiments is not fully in circular shape but rather has tendency to form like a spinal cord as Figure 5-41.

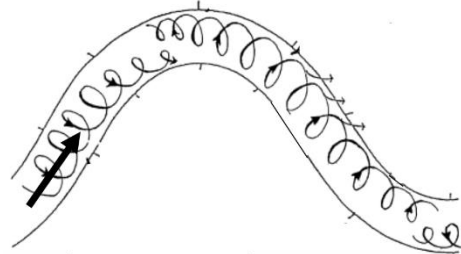


Figure 5-41. Theoretical sketch of helical flows in a curved channel, modified from “flow structure past flood channel facility meanders” (Wormleaton & Ewunetu, 2006)

At the bottom channel, velocity vectors move toward outer bank then sweeps back to inner bank near water surface, and forms helical motion. This helical flow pattern is consistent with the patterns from very recently experiment investigation by Wang and Liu (2015) in Figure 5-40, and theoretical sketch of helical flows in a curved channel by Wormleaton and Ewunetu (2006) Figure 5-41.

6 CONCLUSIONS AND CONTRIBUTIONS

6.1 CONCLUSIONS

This research intended to develop SPH method for modeling meandering dynamics basic characteristics. There are two main parts; (1) modeling meandering dynamics with RMA-10 and RMA-11, and (2) development SPH method to simulate helical flow in a curved channel. From Part 1, we conclude that:

- 1) Most important characteristics of meandering phenomena are dynamics of flow and transport characteristics, and dynamics of morphology.
- 2) In regard to dynamics of flow characteristics, this study has identified that the key characteristic is helical flow.
- 3) With respect to dynamics of transport characteristics, this study has identified that the key characteristics are sediment erosion at the outer banks and deposition in the inner banks.
- 4) This work has shown that RMA is capable to simulate meander of those two characteristics; helical flow and sediment transport.
- 5) The patterns of flow structures computed by RMA can be compared with both measurement results by Hasegawa (1983) and by Xu and Bai (2013).
- 6) In detail, RMA results show that for higher flow velocity is situated at the outer banks and lower velocity is in the inner banks. Large deviation angle (110°) channel shifts the maximum velocity zones and determines the direction of channel migration to downstream. For small deflection angles (30°) location of maximum erosion-deposition zones near the crossover of the sinuosity, for intermediate deflection angles (70°) location of maximum erosion-deposition zones between the crossover and apex of the sinuosity, and for large deflection angles (110°) location of maximum erosion-deposition zones near the apex of the sinuosity, these are agreed with experiments of (Odgaard, 1989), (da Silva, 2006), (da Silva, et al., 2006), and (Esfahani & Keshavarzi, 2012).
- 7) But, since RMA is based on stationer grid, it is not able to simulate the meander dynamics of morphology.

- 8) Nevertheless, any effort to overcome this lack, the model has to possess the above two capabilities; flow velocity and sediment transport characteristics.
- 9) Or in other words, these results from this study can be used as reference to develop other model, and we propose SPH method to helical flow.

From Part 2, we achieve that:

- 1) The very basic characteristic in meandering dynamics is helical flow.
- 2) Helical flow is initiated by adding up viscous flow and vorticity at initial conditions.
- 3) Formation of helical flow is generated downstream hemispheres part of the curved channel.
- 4) Viscous flow plays the main role in the development of helical flow.
- 5) Helical flow pattern from SPH model can be compared with helical flow patterns from RMA model.
- 6) The helical flow pattern is consistent with the patterns from very recently experiment investigation by Wang and Liu (2015), and theoretical sketch of secondary flows in a curved channel by Wu (2008) and Wormleaton & Ewunetu (2006).
- 7) SPH method is able to predict realistically helical flow as a result of curvature, agreed with Camporeal et al. (2007), and even without sediment transport, agreed with da Silva (2006) and Yalin (1993).

6.2 RESEARCH CONTRIBUTIONS

SPH becomes popular in Hydraulics community. Our contribution with this research is developing SPH method for modeling helical flow in a curved channel with the aim of simulating meandering dynamics. This is all along with advancement of SPH in Hydraulics. Four grand challenges in SPH applications in Hydraulics, according to SPHERIC community (Violeau & Rogers, 2015), are convergence, numerical stability, boundary conditions, and adaptivity. This research participates to the two of SPH challenges; (1) boundary conditions where we used simple geometries based on Snell's law to represent basic particle

responses to channel walls, and (2) adaptivity where we adapted SPH for nearly incompressible method for basic hydraulics phenomenon in a curved channel that is note bene an incompressible flow.

6.3 SUGGESTIONS FOR FUTURE RESEARCH

Development SPH method for modeling helical flow in a curved channel is the very first step to model meandering dynamics. Near future research is to couple SPH model with advective dispersive equation for sediment transport modeling in a curved channel. Then, research may continue with momentum transfer elaboration to model scouring process in a curved channel.

REFERENCES

- Aristodemo, F., Federico, I., Veltri, P. & Panizzo, A., 2010. Two-phase SPH modelling of advective diffusion processes. *Environmental Fluid Mechanics*, Volume 10, pp. 451-470.
- Bates, P. D., Lane, S. N. & Ferguson, R. I., 2005. *Computational Fluid Dynamics: Applications in Environmental Hydraulics*. s.l.:John Wiley and Sons, Ltd..
- Beresh, S. J., Henfling, J. F. & Spillers, R. W., 2010. Meander of a fin trailing vortex and the origin of its turbulence. *Exp Fluids*, Volume 49, pp. 599-611.
- Binns, A. D., 2012. *Nature and time-scale of bed morphological adjustments towards equilibrium in meandering streams: an experimental study*, Kingston: Queen's University.
- Blanckaert, K. & de Vriend, H. J., 2010. Meander Dynamics: A Nonlinear Model without Curvature Restrictions for Flow in Open-Channel Bends. *Journal Geophysical Research Atmosphere*, 115(F04011).
- Camporeal, C., Perona, P., Porporato, A. & Ridolfi, L., 2007. Hierarchy of Models for Meandering Rivers and Related Morphodynamic Processes. *Reviews of Geophysics* , 45(1), pp. 1-28.
- Chanson, H., 2004. *Environmental Hydraulics of Open Channel Flows*. s.l.:Elsevier Butterworth-Heinemann.
- Chapra, C. S., 1997. *Surface Water-Quality Modeling*. International ed. s.l.:McGraw-Hill.
- Chapra, S. C. & Canale, R. P., 2010. *Numerical Methods for Engineers*. Sixth ed. New York: McGraw-Hill.
- Cheney, W. & Kincaid, D., 2008. *Numerical Mathematics and Computing*. Sixth ed. s.l.:Thomson Brooks/Cole.
- Clark, L. A. & Wynn, T. M., 2007. Methods for Determining Streambank Critical Shear Stress and Soil Erodibility: Implications for Erosion Rate Predictions. *Transactions of the ASABE, American Society of Agricultural and Biological Engineers*, 50(1), pp. 95-106.
- Corney, R. K. T. et al., 2006. The orientation of helical flow in curved channels. *Sedimentology*, Volume 53, p. 249.
- da Silva, A. F. & El-Tahawy, T., 2006. *Location of hills and deeps in meandering streams: An experimental study*. Lisbon, Portugal, Taylor & Francis, p. 1097.
- da Silva, A. M. F., 2006. On why and how do rivers meander. *Journal of Hydraulic Research*, pp. 579-590.
- da Silva, A. M. F. & Ahmari, H., 2009. Size and effect on the mean flow of large-scale horizontal coherent structures in open-channel flows: an experimental study. *Canadian Journal Civil Engineering*, 36(9), pp. 1643-1655.

- da Silva, A. M. F. & El-Tahawy, T., 2008. On the location in flow plan of erosion-deposition zones in sine-generated meandering streams. *Journal of Hydraulic Research*, 46(S1), pp. 49-60.
- da Silva, A. M. F., El-Tahawy, T. & Tape, W. D., 2006. Variation of Flow Pattern with Sinuosity in Sine-Generated Meandering Streams. *Journal of Hydraulics Engineering*, pp. 1003-1014.
- da Silva, A. M. F. & Yalin, M. S., 2006. *On the bed deformation in meandering streams*. Lisbon, Portugal, Taylor & Francis, p. 1119.
- Dai, W. H., 2008. *On the simulation and prediction of bed morphological adjustments of equilibrium in alluvial meandering streams*, Kingston: Queen's University.
- Darby, S. E. & Peakall, J., 2012. Modelling the equilibrium bed topography of submarine meanders that exhibit. *Geomorphology*, Volume 163-164, pp. 99-109.
- de Vriend, H. J., 1977. A Mathematical Model of Steady Flow In Curved Shallow Channels. *Journal of Hydraulic Research*, 15(1), pp. 37-54.
- Desbrun, M. & Gascuel, M. -P., 1996. Smoothed Particles: A new paradigm for animating highly deformable bodies. In: *Computer Animation and Simulation '96*. s.l.:Springer Vienna, pp. 61-76.
- Duan, J. G. & Julien, P. Y., 2010. Numerical Simulation of Meandering Evolution. *Journal of Hydrology*, Volume 391, pp. 34-46.
- Einstein, A., 1926. The Cause of the Formation of Meanders in the Courses of Rivers and of the So-Called Baer's Law. *Die Naturwissenschaften*, Volume 14.
- Engel, F. L. & Rhoads, B. L., 2012. Interaction among mean flow, turbulence, bed morphology, bank failures and channel planform in an evolving compound meander loop. *Geomorphology*, 163-164(15), pp. 70-83.
- Ervine, D. A., Willetts, B. B., Sellin, H. J. & Lorena, M., 1993. Factors Affecting Conveyance in Meandering Compound Flows. *Journal of Hydraulic Engineering*, 119(12), pp. 1383-1399.
- Esfahani, F. S. & Keshavarzi, A., 2012. Dynamic mechanism of turbulent flow in meandering channels: considerations for deflection angle. *Stochastic Environmental Research and Risk Assessment* , pp. 1093-1114.
- Fischer, H. B. et al., 1979. *Mixing in Inland and Coastal Waters*. s.l.:Academic Press, Inc..
- Garde, R. J., 2006. *River Morphology*. s.l.:New Age International (P) Ltd..
- Gingold, R. A. & Monaghan, J. J., 1977. Smoothed particle hydrodynamics: theory and application to non-spherical stars. *Mon. Not. Royal Astronomical Society*, Volume 181, pp. 375-389.
- Gomez-Gesteira, M., Rogers, B. D. & Dalrymple, R. A., 2010. State-of-the-art of classical SPH for free-surface flows. *Journal of Hydraulic Research*, 48(Extra Issue), pp. 6-27.

- Gomez-Gesteira, M., Rogers, B. D., Dalrymple, R. A. & Crespo, A. J. C., 2010. State-of-the-art of classical SPH for free-surface flows. *Journal of Hydraulic Research*, 48(Extra), p. 6–27.
- Gomez-Gesteira, M. et al., 2010. Foreword: SPH for free-surface flows. *Journal of Hydraulic Research*, 48(Extra), pp. 3-5.
- Güneralp, İ., Abad, J. D., Zolezzi, G. & Hooke, J., 2012. Advances and challenges in meandering channels research. *Geomorphology*, Volume 163-164, pp. 1-9.
- Gyr, A., 2011. Old and new concepts based on coherent structures for understanding sediment transport. *International Journal of Sediment Research*, 26(3), pp. 378-386.
- Hasegawa, K., 1983. A study on flows and bed topographies in meandering channels. *Proceedings JSCE*, Volume 338, pp. 105-114.
- Hirsch, C., 2007. *Numerical Computation of Internal and External Flows: Volume 1 Fundamentals of Computational Fluid Dynamics*. Second ed. s.l.:Butterworth-Heinemann.
- Hussain, A. K. M. F., 1983. Coherent Structures—Reality and Myth. *Physics of Fluids*, Volume 26.
- Ji, Z. G., 2008. *Hydrodynamics and Water Quality: Modeling Rivers, Lakes, and Estuaries*. s.l.:Wiley Interscience.
- Julien, P. Y., 2002. *River Mechanics*. s.l.:Cambridge University Press.
- Kao, H. -M. & Chang, T. -J., 2012. Numerical modeling of dambreak-induced flood and inundation using smoothed particle hydrodynamics. *Journal of Hydrology*, Volume 448-449, pp. 232-244.
- Kelager, M., 2006. *Lagrangian Fluid Dynamics Using Smoothed Particle Hydrodynamics*. s.l.:DIKU, Department of Computer Science, University of Copenhagen, Denmark.
- Keshavarzi, A. & Esfahani, F. S., 2011. Effect of different meander curvatures on spatial variation of coherent turbulent flow structure inside ingoing multi-bend river meanders. *Stochastic Environmental Research and Risk Assessment*, Volume 25, pp. 913-928.
- King, I., 1993. *RMA-10 A Finite Element Model for Three-Dimensional Density Stratified Flow*. s.l.:Department of Civil and Environmental Engineering, University of California Davis.
- King, I., 2012. *A Finite Element Model for Stratified Flow RMA-10 Users Guide*. Version 8.7e ed. Sydney: Resource Modelling Associates.
- King, I., 2013. *RMA-11: A Three Dimensional Finite Element Model for Water Quality in Estuaries and Streams*. Documentation Version 8.7H ed. Sydney: Resource Modelling Associates.
- Kristof, P., Beneš, B., Křivánek, J. & Št'ava, O., 2009. Hydraulic Erosion Using Smoothed Particle Hydrodynamics. *EUROGRAPHICS*, 28(2).

- Langbein, W. B. & Leopold, L. B., 1966. *River Meanders - Theory of Minimum Variance*. Geological Survey Professional Paper 422 H ed. Washington: US Government Printing Office.
- Leopold, L. B. & Wolman, M. G., 1957. *River Channel Patterns, Braided, Meandering and Straight*. Geological Survey Professional Paper 282 B ed. Washington: US Government Printing Office.
- Liu, G. R. & Liu, M. B., 2003. *Smoothed Particle Hydrodynamics: a meshfree particle method*. s.l.:World Scientific.
- Liu, M. B. & Liu, G. R., 2010. Smoothed Particle Hydrodynamics (SPH): an Overview and Recent Developments. *Arch Comput Methods Eng*, Volume 17, pp. 25-76.
- Lucy, L. B., 1977. A numerical approach to the testing of the fission hypothesis. *The Astronomical Journal*, 82(12), pp. 1013-1024.
- Manenti, S., Sibilla, S., Agate, G. & Guandalini, R., 2012. SPH Simulation of Sediment Flushing Induced by a Rapid Water Flow. *Journal of Hydraulic Engineering*, 138(3), pp. 272-284.
- Mao, Y., 2003. The Effects of Turbulent Bursting on The Sediment Movement in Suspension. *International Journal of Sediment Research*, 18(2), pp. 148-157.
- Monaghan, J. J., 2005. *Smoothed particle hydrodynamics*, s.l.: Report on Progress in Physics, Institute of Physics Publishing, IOP Publishing Ltd, UK.
- Monaghan, J. J., 2012. Smoothed Particle Hydrodynamics and Its Diverse Applications. *Annual Review of Fluid Mechanics*, Volume 44, pp. 323-346.
- Müller, M., Charypar, D. & Gross, M., 2003. *Particle-Based Fluid Simulation for Interactive Applications*. s.l., Eurographics/SIGGRAPH Symposium on Computer Animation.
- Müller, M., Solenthaler, B., Keiser, R. & Gross, M., 2005. Particle-Based Fluid-Fluid Interaction. *Eurographics/ACM SIGGRAPH Symposium on Computer Animation*, pp. 1-7.
- Odgaard, A. J., 1989. River-Meander Model. I: Development. *Journal Hydraulics Engineering*, Volume 115, pp. 1433-1450.
- Papanicolaou, A. N. T. et al., 2008. Sediment Transport Modeling Review—Current and Future Developments. *Journal of Hydraulic Engineering*, 134(1), pp. 1-14.
- Potter, M. C., Wiggert, D. C., Bassem, R. & Shih, T. I.-P., 2012. *Mechanics of Fluids*. Stamford: Cengage Learning.
- Price, D. J., 2004. *Magnetic fields in Astrophysics, Doctoral Thesis*. s.l.:University of Cambridge, UK..
- Prince George's County, 1999. *Low-Impact Development Design Strategies: An Integrated Design Approach*. Maryland: Department of Environmental Resource, Programs and Planning Division.
- Raudkivi, A. J., 1998. *Loose Boundary Hydraulics*. s.l.:A. A. Balkema.

- Riley, J. D. & Rhoads, B. L., 2012. Flow structure and channel morphology at a natural confluent meander bend. *Geomorphology*, 84(98), pp. 163-164.
- Sanjou, M. & Nezu, I., 2009. Turbulence structure and coherent motion in meandering compound open-channel flows. *Journal of Hydraulic Research*, 47(5), pp. 598-610.
- Shao, S. & Gotoh, H., 2005. Turbulence particle models for tracking free surfaces. *Journal of Hydraulic Research*, 43(3), pp. 276-289.
- Solenthaler, B. et al., 2011. SPH Based Shallow Water Simulation. *Workshop on Virtual Reality Interaction and Physical Simulation VRIPHYS*.
- Struiksma, N., Olesen, K. W., Flokstra, C. & de Vriend, H. J., 1985. Bed deformation in curved alluvial channels. *Journal of Hydraulic Research*, 23(1), pp. 57-79.
- Termini, D., 2009. Experimental Observations of Flow and Bed Processes in Large-Amplitude Meandering Flume. *Journal of Hydraulic Engineering*, 135(7), pp. 575-587.
- Termini, D. & Piraino, M., 2011. Experimental analysis of cross-sectional flow motion in a large amplitude meandering bend. *Earth Surface Process Landforms*, Volume 36, pp. 244-256.
- Tilston, M., Rennie, C., Arnott, R. W. C. & Post, G., 2009. *On the Nature of Coherent Turbulent Structures in Channel Bends: Burst-Sweep Orientations in Three-Dimensional Flow Fields*. s.l., 33rd IAHR Congress: Water Engineering for a Sustainable Environment.
- van Balen, W., Uijttewaal, W. S. J. & Blanckaert, K., 2010. Large-eddy simulation of a curved open-channel flow over topography. *Physics of Fluids*, Volume 22.
- van Rijn, L. C., 1993. *Principles of Sediment Transport in Rivers, Estuaries and Coastal*. Netherland: Aqua Publications.
- Vickers, D., Mahrt, L. & Belušić, D., 2008. Particle simulations of dispersion using observed meandering and turbulence. *Acta Geophysica*, 56(1), pp. 234-256.
- Vickers, D., Mahrt, L. & Belušić, D., 2008. Particle simulations of dispersion using observed meandering and turbulence. *Acta Geophysica*, 56(1), pp. 234-256.
- Violeau, D., 2012. *Fluid Mechanics and the SPH Method: Theory and Applications*. s.l.:Oxford University Press.
- Violeau, D. & Rogers, B. D., 2015. The SPHERIC Community. *HydroLink*, p. 73.
- Wang, X. & Liu, X., 2015. Experimental Investigation of Flow Structures and Bed Deformation with Small Width-to-Depth Ratio in a Bend. *Korean Society of Civil Engineers*, Volume 0, pp. 1-12.
- Wendt, J. F. ed., 2009. *Computational Fluid Dynamics: An Introduction*. Third ed. Berlin(Heidelberg): Springer-Verlag.
- Wieringa, J., 1980. Representativeness of Wind Observations at Airports. In: De Bilt, Netherlands: Royal Netherlands Meteorological Institute.
- Wilkes, J. O. et al., 2006. *Fluid Mechanics for Chemical Engineers with Microfluids and CFD*. Second ed. s.l.:Prentice Hall PTR.

Woo, H., 2010. Trends in ecological engineering in Korea. *Journal of Hydro-environment Research*, Volume 4, pp. 269-278.

Wormleaton, P. R. & Ewunetu, M., 2006. Three-dimensional k- ϵ numerical modelling of overbank flow in a mobile bed meandering channel with floodplains of different depth, roughness and planform. *Journal of Hydraulic Research*, 44(1), pp. 18-32.

Wu, W., 2008. *Computational River Dynamics*. London, UK: Taylor and Francis Group.

Xu, D. & Bai, Y., 2013. Experimental study on the bed topography evolution in alluvial meandering rivers with various sinuousnesses. *Journal of Hydro-environment Research*, Volume 7, pp. 92-102.

Yalin, M. S., 1992. *River Mechanics*. Ontario: Pergamon Press Lt..

Zhiyao, S., Tinting, W., Fumin, X. & Ruijie, L., 2008. A simple formula for predicting settling velocity of sediment particles. *Water Science and Engineering*, 1(1), pp. 37-43.